STUDY OF WAVES OBSERVED IN THE EQUATORIAL IONOSPHERIC VALLEY REGION USING JICAMARCA ISR AND VIPIR IONOSONDE

BY

PABLO MARTIN REYES

DISSERTATION

Submitted in partial fulfillment of the requirements
for the degree of Doctor of Philosophy in Electrical and Computer Engineering
in the Graduate College of the
University of Illinois at Urbana-Champaign, 2017

Urbana, Illinois

Doctoral Committee:

Professor Erhan Kudeki, Chair
Professor Jonathan J. Makela
Professor Steven J. Franke
Professor Jianming Jin

ABSTRACT

Incoherent scatter (IS) radar and ionosonde (VIPIR, vertical incidence pulsed ionospheric radar) data were taken concurrently at Jicamarca during campaigns of January, April, June, and July 2015, January 2016, and most recently April 2017 to bring more insight into the state and dynamics of the ionospheric E-F valley region and the 150-km radar echoes detected from this region. To better understand the rich and dynamic vertical structure of 150-km echoes observed at the Jicamarca Radio Observatory (JRO) and other equatorial stations and to contribute to the understanding of the physics of this region, we used JRO ISR and VIPIR ionosonde techniques to perform high spatial and temporal resolution measurements.

We found correlations between VHF backscatter radar measurements and fluctuations detected with the VIPIR ionosonde, which is an indication of gravity waves playing a role in modulating the space-time structure of the 150-km echoes. Fluctuations with periods from 5 to 15 minutes are observed in VIPIR ionograms as well as in the layers found in the 50 MHz radar range-time-intensity (RTI) plots. The quiet-time stratified electron density contours are being rippled by waves propagating through the ionosphere. Evidence for this is the fluctuation of virtual reflection heights and angle of arrival (AOA) of the ionosonde echoes. The AOA is provided by interferometry, which indicates that the echo is not always coming from overhead. Scatter plots of the AOA in the receiving antenna's orthogonal baselines give us the propagation direction. Plots of virtual height

and AOA obtained using VIPIR data show phase fronts propagating downwards, which is characteristic of internal gravity waves (IGW). Other characteristics of IGW are present in the oscillations of virtual height: their frequencies are just below the Brunt-Väisälä frequency, their amplitudes increase with altitude, and shorter vertical wavelengths seen in lower altitudes are heavily damped in higher altitudes. The observed IGW exhibit fluctuations similar to those seen in the thin "forbidden" or "quite" zone of the 150-km echo undulations, which indicates some IGW-driven modulations of the 150-km echo as has been suggested previously [e.g. *Kudeki and Fawcett*, 1993; *Chau and Kudeki*, 2013]. Phase profiles of cross-correlation pair of antennas in the IS Faraday rotation experiment exhibit a smooth progression with altitude. That means that there are no sharp density gradients that could be a source of plasma instabilities. Still, density variations across the magnetized plasma in the region can be key to explaining the enhanced echoes observed via the electrodynamics that they can drive.

We also found that there exist sub-minute quasi-periodic (SMQP) fluctuations when zooming into high time resolution RTI plots. This is a new observation that has not been reported in the literature to date. A method was designed in order to validate the existence of SMQP fluctuations. The method consisted of identifying episodes of sub-minute fluctuations in a non-exhaustive search of high resolution RTI plots using a web-based interactive tool designed for zooming in and marking the episodes where the sub-minute period fluctuations were found. We found a wide range of sub-minute periods, with a predominance between 15 and 20 seconds. This was a first step towards reporting SMQP; a more exhaustive method to search for these fluctuations is being produced.

This multi-instrument approach helps us to characterize the daytime electron density fluctuations in the equatorial valley region, and aims to contribute to the goal of understanding better the fundamental physics of the region.

A mi amada familia: mi esposa Erin,
mi hijo Reimare, y mi hija Soleia

ACKNOWLEDGMENTS

I sincerely thank all my PhD committee members, especially my adviser, Professor Erhan Kudeki, for his contributions, comments and reviews of this work, for his guidance and support, and all his teachings. I want to thank my wife, Dr. Erin McKenna, for supporting me through all my dissertation work. I want to thank my children, who provided great moments of joy all the time. Thanks to my parents Elmer and Ada for their wise guidance and teachings throughout different stages of my life.

I would like to thank the Jicamarca Radio Observatory (JRO) director, Dr. Marco Milla, for his friendship and advice during my time working as an electrical engineer at JRO and during my MS and PhD studies at the University of Illinois. I would also like to thank my colleagues in the Remote Sensing and Space Sciences (RSSS) group: Mark Butala, Gonzalo Cucho, Ben Eng, Dan Fisher, Levent Gezer, Matt Grawe, Stephen Hall, Brian Harding, Kiwook Lee, Yamuna Phal, Jianqi Qin, Fabio Vargas, Binghui Wang, Shiyi Yang, and others. The work environment and the collaboration experienced in this group make the UIUC RSSS a great research place.

I want to thank also all the scientific staff, engineers, and friends at the JRO in Lima, Perú, from whom I learned so much when I worked there and also for their support during my visits to the observatory. Discussions and collaboration with my colleagues Marco Milla, Jorge L. Chau and Gerald Lehmacher were very useful for their contribution to this work. Thanks to Tim Duly for creating and

maintaining pyglow, an open-source Python module that wraps several upper atmosphere climatological models like IRI, MSIS, and IGRF. I also thank César de la Jara for his help with providing information and data from the VIPIR ionosonde system. I am also very thankful to the community involved in constantly developing and maintaining the open source programming tools used in this dissertation; these include Python, as well as all the associated libraries: Numpy, Scipy, Matplotlib, and the Bokeh interactive visualization library to generate the web-based tools.

TABLE OF CONTENTS

CHAPTER 1

INTRODUCTION

The purpose of this study is to observe and bring more insight into the state and dynamics of the equatorial ionospheric valley region over the Jicamarca Radio Observatory (JRO) using radar and ionosonde techniques. The ionospheric valley region is the part of the ionosphere between the E- and F-regions that shows a reduction of electron density, as shown in the right part of Figure 2.1. Figure 1.1 shows a typical equatorial daytime range-time-intensity (RTI) plot of 50 MHz radar backscatter at Jicamarca from altitudes ranging from 60 km to 180 km. Signals shown there from bottom to top are due to mesospheric turbulence, electrojet irregularities, and 150-km echoes. The 150-km echoes are relatively strong VHF radar backscatter returns from the ionosphere close to Earth's magnetic equator. The measurements were taken using ~2 MW transmitted power pulses of 64-baud complementary code with a baud length of 1 μs (150 m height resolution). This coding schema is suitable for probing slowly fading radar returns from the mesosphere and the strong echoes from the 150-km regions, but fails to decode properly for the rapidly fading returns from electrojet heights. A zoom of Figure 1.1 that displays only the 150-km echo region is shown in Figure 1.2. Note that the 150-km echo RTI has the characteristic "necklace shape" which was first reported by *Kudeki and Fawcett* [1993] with multiple layers that descend at morning hours and ascend in the afternoon. Typical layer widths are

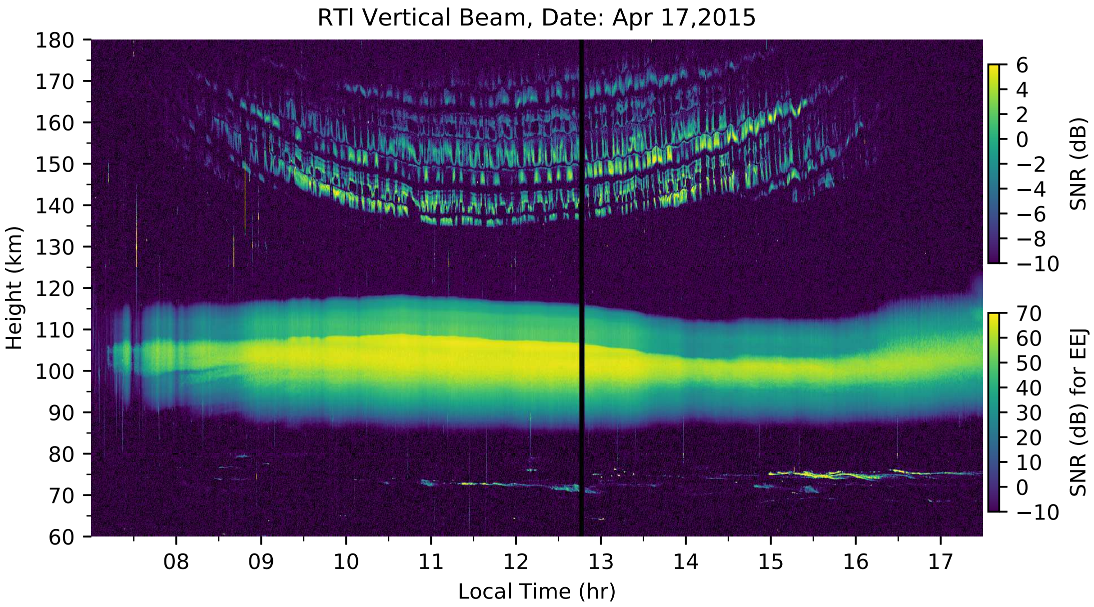

Figure 1.1 – Range-time-intensity (RTI) plot of signal-to-noise (SNR) of 50 MHz JRO with a 150 m height resolution and a time resolution about 8 s. The data used for this plot was taken during an MST-ISR-EEJ campaign (details about this operation mode are given in section 3.2). The RTI plot presents evidence for narrow scattering layers in the mesosphere (60-80 km), an over-saturated backscatter from the equatorial electrojet (90-120 km), and an intricately structured backscattered power pattern for the 150-km echoes (>130 km) which is the subject of this study. Note that different color bars are used for electrojet returns and returns from mesosphere and 150 km region.

5 to 10 km and echo intensity within each layer exhibits temporal fluctuations with about 5 to 15 minute period. Narrow "forbidden regions" separating adjacent echoing layers exhibit quasi-periodic height variations with also about 5 to 15 minute periodicity. These features of the necklaced shaped 150-km echo RTI are observed every day and show relatively minor variations from day to day.

The 150-km echoes were first described by *Balsley* [1964] using oscilloscope screenshots and filmstrips as narrow stratified echoes showing simultaneously up to four layers at different heights in the region around 150 km of altitude. *Kudeki and Fawcett* [1993] showed that using the 150-km echo vertical Doppler velocities was a way to measure the ionospheric zonal electric fields at equatorial latitudes. The vertical drift of these echoes is routinely used as a proxy for the $\mathbf{E} \times \mathbf{B}$ drift of

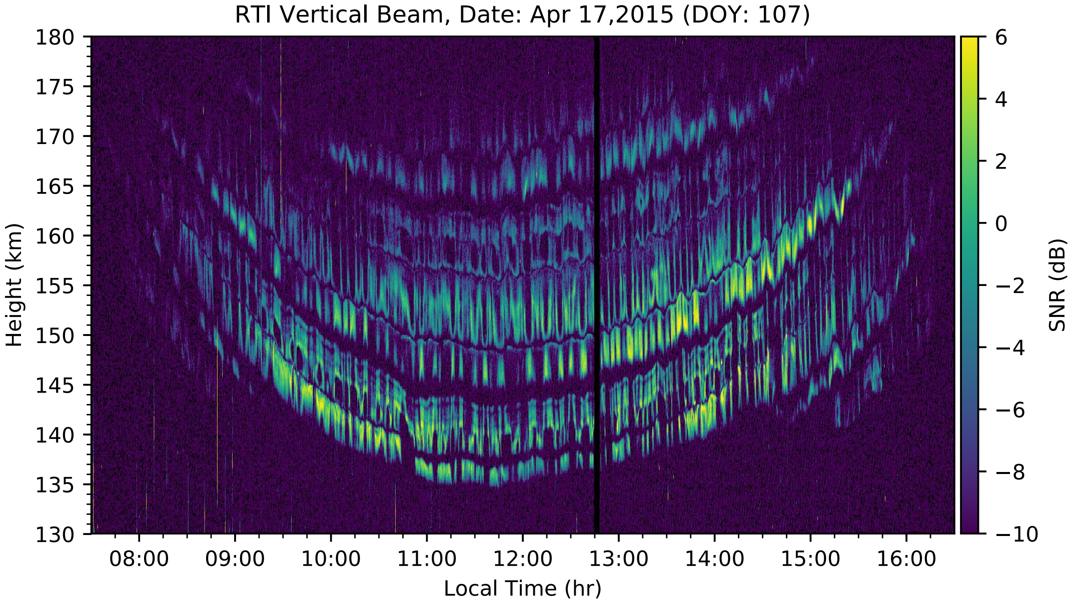

Figure 1.2 – A blow-up of the RTI in Figure 1.1 focusing only in 150-km echoes.

the F-region [e.g. *Chau and Woodman*, 2004] that drives the equatorial fountain effect. *Chau and Kudeki* [2013] discovered that the 150-km echoes consist of mainly two types of echoes: the naturally enhanced incoherent scatter (NEIS) and the field-aligned irregularity (FAI) echoes, which they named type A echoes and type B echoes respectively, the former being the more abundant at Jicamarca. They also pointed out that the mechanism of generation of 150-km radar echoes as well as the associated necklace shaped 150-km echo RTI is still unknown more than 50 years after the first report by *Balsley* [1964]. Recently, *Oppenheim and Dimant* [2016] have shown, using large-scale kinetic simulations, that energetic photoelectrons can cause the enhancement of radar measurements of plasma lines and ion lines around 150 km of altitude. *Reyes* [2012] studied the effects of solar flare events on the equatorial ionosphere, and showed that the 150-km echoes were enhanced obeying the increase in energetic solar flux (now contributing to the theory of the role of energetic photoelectrons in the enhance mechanism). The same study also observed that during solar flare events the different layers of the 150-km echoes were compressed and pushed down during the onset of the flares. *Oppenheim and Dimant* [2016] suggest that more studies should be done comparing energetic solar emission strength and the valley region amplitudes. While all these findings bring us closer to an understanding of the enhancement mechanism of the backscatter echoes present in this region, there is still much work to be done to explain the rich spatial structure and dynamics of the 150-km echoes observed at JRO and other equatorial stations. In an effort to contribute to the understanding of the physics of this region, we used JRO ISR and VIPIR ionosonde techniques to perform high temporal resolution measurements of the echoes. We found correlations between VHF backscatter radar measurements and fluctuations detected with the VIPIR ionosonde which make a strong case for gravity waves propagating through the equatorial valley region ionosphere having some major role in the structuring of the 150-km VHF radar echoes. We also found that there exist some sub-minute quasi-periodic (SMQP) time-scale fluctuations when zooming into high time resolution RTI plots.

JRO (11.95° S, 76.87° W) is an equatorial station located near Lima, Peru, that consists of a set of radio and optical remote sensing instruments along with its main facility, a 50 MHz incoherent scatter radar (ISR) with MW power transmitters and a 300 m by 300 m modular antenna array system consisting of half-wavelength dipoles [*Ochs*, 1965]. Among the radio instruments, JRO maintains and runs a VIPIR ionosonde, which consists of a wide-band antenna that sends vertically propagating radio wave pulses by means of a 4 kW transmitter sweeping from 0.3 to 25 MHz. The detection of the reflected pulses is done by 8 short dipoles connected to 8 coherent receivers. The receiving antennas form a set of orthogonal interferometric baselines that can be used to detect the angle of arrival (AOA) of the reflected radio waves. The oscillation of the AOA in the ionosonde data is an indication of the electron density contours being rippled by waves crossing the ionosphere. These waves, possibly gravity waves (GW), are ubiquitous. In section 3.3 we will see examples of how the waves are present at all daytime hours and extend throughout the ionosphere or at least up to the peak of the ionosphere that is what an ionosonde can detect.

Concurrent IS radar and VIPIR data were taken at Jicamarca in January, April, June, and July 2015, and during January 2016. In this work, we present ISR and VIPIR measurements. The ISR experiments used were the Valley experiment, and the MST-ISR-EEJ [e.g., *Akgiray*, 2007; *Lehmacher et al.*, 2009]. The Valley experiment uses the main JRO antenna transmitting linearly polarized electro-magnetic (EM) pulses, and receiving with both circular polarizations to get electron density profiles by means of the Faraday rotation technique. This method is explained in Chapter 3. It has two modes: the wide-band and the narrow-band modes. The wide-band mode measures up to ±2142.8 m/s of Doppler frequency spectra, but range aliased due to an inter-pulse-period (IPP) of 105 km and sampling every 0.75 km. The narrow-band mode measures electron density profiles up to 420 km, sampling every 0.75 km and has spectral widths of ±535.7 m/s. The MST-ISR-EEJ experiment is relevant to this study because of its high range resolution of 0.15 km, and high temporal resolution 2.5 s of integrated data, which captures the small-scale dynamics of the 50 MHz backscatter fluctuations of the 150-km region.

This study is organized as follows: In Chapter 2 we provide a brief overview of pertinent aspects of ionospheric physics including some specific characteristics of the valley region. We also include some aspects of magneto-ionic (MI) propagation effects, which are used to explain the results of the VIPIR ionosonde, as well as the Faraday rotation technique used with the IS data to get electron density profiles. At the end of the chapter we include basic concepts of waves in the the neutral atmosphere with emphasis on internal gravity waves (IGW).

Chapter 3 is devoted to descriptions of the instruments and the data sources and the presentation of the pertinent data sets acquired using the 50 MHz IS radar and the VIPIR ionosonde. Chapter 4 describes the correlation between VIPIR virtual height oscillations and the fluctuations of 150-km echo layers. Chapter 5 reports on the sub-minute quasi-periodic (SMQP) power fluctuations in the 150-km echo region detected at Jicamarca. Finally Chapter 6 offers the results and conclusions, and ideas for future direction in the studies of the valley region.

CHAPTER 2

EARTH ATMOSPHERE

2.1 Earth's Atmosphere and Ionosphere

The Earth's atmosphere is the outermost layer of our planet and consists of molecules and atoms in gaseous form. Figure 2.1 shows the principal layers of the atmosphere using two different metrics to divide it. One of the criteria to divide the atmosphere is the temperature of the neutral gas, which yields to the following four main regions: the troposphere, the stratosphere, the mesosphere, and the thermosphere. The other division criterion is the concentration of free electrons that yields three distinguishable regions: the D-region, the E-region, and the F-region.

The graph on the left of Figure 2.1 shows the division of the atmosphere based on the temperature profile. This plot has been made with data from the mass spectrometer and incoherent scatter data (MSIS-E 90)[1] model [*Hedin*, 1991].

The troposphere is the first layer above the surface of Earth. In this region the temperature decreases with altitude up to the tropopause (around 20 km). The following layer is called the stratosphere and here the temperature increases with altitude up to the stratopause (about 50 km). The mesosphere is the layer above

---

[1] The MSIS-E model describes the neutral temperature and densities in Earth's atmosphere from ground to thermospheric heights and is based on data compilation from several instruments including incoherent scatter radars. The data can be downloaded, online for a particular location, date and time from the following URL: `http://ccmc.gsfc.nasa.gov/modelweb/models/msis_vitmo.php` .

the stratosphere where the temperature decreases up to the mesopause (about 90 km) which is the coldest place in the Earth system (average of 190 K). Finally the layer above the mesosphere is called the thermosphere where the temperature increases with altitude up to a maximum of around 1000 K and remains constant in height.

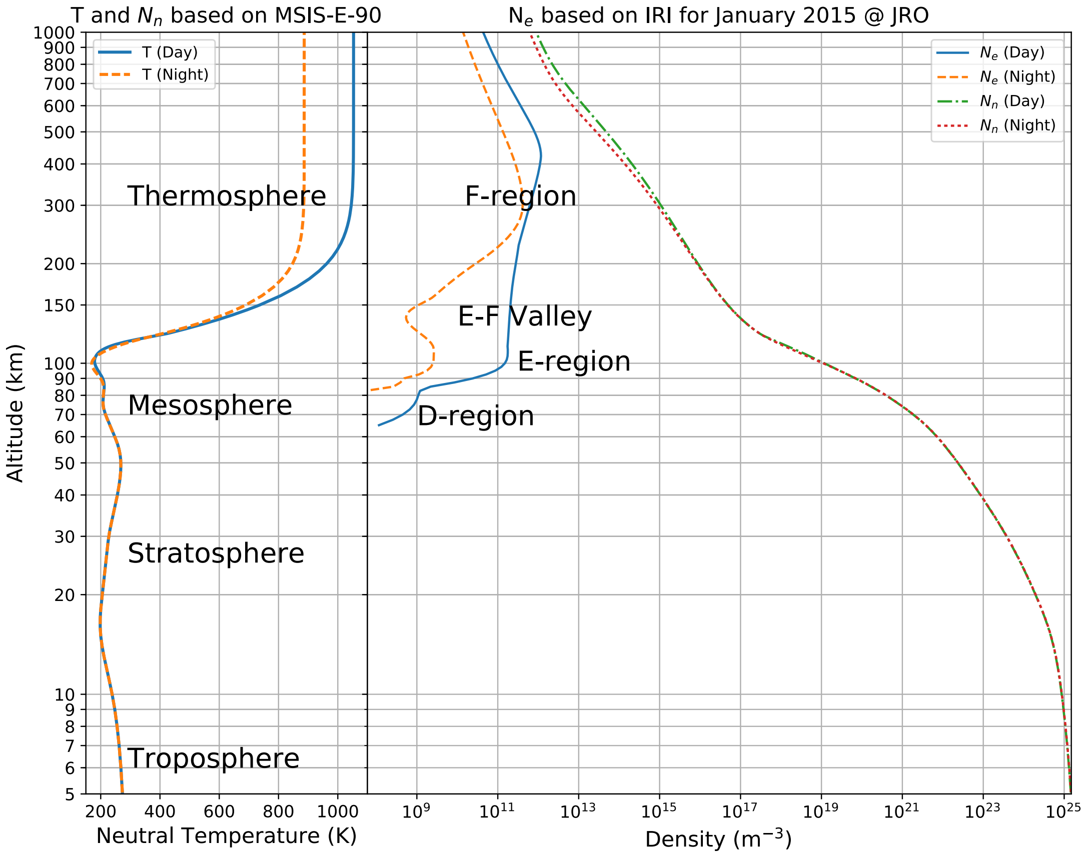

Figure 2.1 – Typical neutral temperature and electron and neutral density profile showing the different layers of the atmosphere. These plots were generated with data from the “mass spectrometer & incoherent scatter” data (MSIS-E 90) model for the temperature and neutral density profiles, and from the “international reference ionosphere” (IRI) model for the electron density profile. The location chosen was the JRO coordinates, the date January 15, 2015, and the times 12 and 0 local time (LT) for day and night respectively. After *Kelley* [2009].

The part of the upper atmosphere where free electrons and ions coexist with neutral molecules and atoms is called the ionosphere and extends from about

50 km to more than 1000 km of altitude. The graph on the right of Figure 2.1 shows the concentration of free electrons as a function of altitude and indicates the different layers (D, E and F regions) in which the ionosphere is divided. This plot has been made with data from the international reference ionosphere (IRI)[2] model [*Bilitza*, 2001].

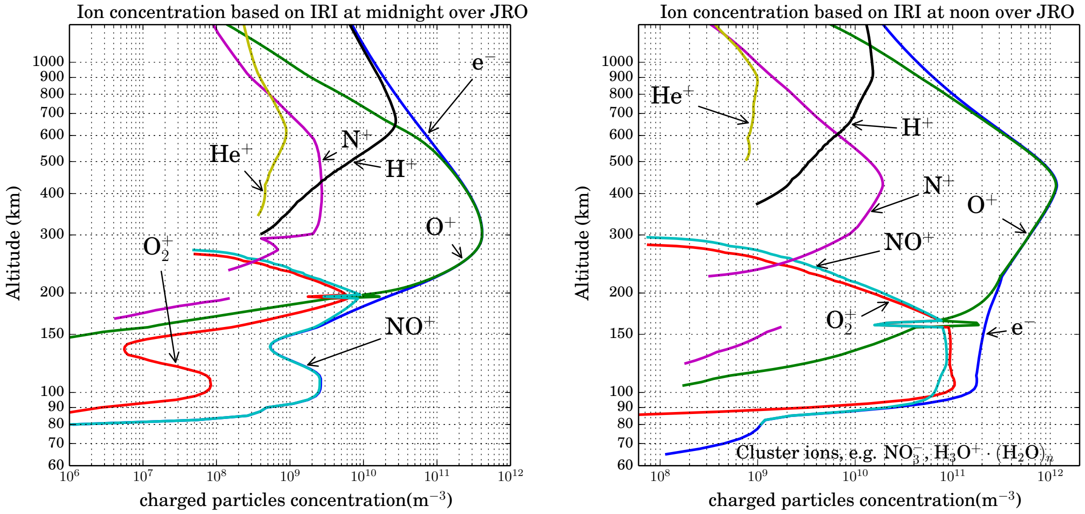

Figure 2.2 – Ion composition plots with data obtained from the international reference ionosphere (IRI) model for the electron density profile. The location chosen was the JRO coordinates, the date was January 15, 2015. The graph on the left represents a sample at midnight and the one on the right at noon.

The ionization of the neutral species in the atmosphere is caused by solar radiation, especially X-ray and ultraviolet radiation, that provides the proper amount of energy to an electron bounded to an atom (or molecule) to make it escape from its potential well to yield a free electron and a positively charged ion. Negatively charged ions are also present, but only in the D-region where the probability of an electron hitting a neutral molecule and remaining attached to

---

[2] The IRI is an empirical standard model of the ionosphere, based on all available data sources (e.g. ionosondes and IS radars) that provides averages of electron density, electron temperature, ion temperature and ion composition for the altitude range from 50 km to 2000 km. The data can be downloaded online, for a particular location, date and time from the following URL: `http://omniweb.gsfc.nasa.gov/vitmo/iri_vitmo.html` .

it is greater due to the denser atmosphere.

Table 2.1 – Classification of the ionosphere according to composition (from *Prölss* [2004]).

Name	Range	Main Constituents
D-region	$h \lesssim 90\,\mathrm{km}$	e.g. $H_3O^+ \cdot (H_2O)_n$, NO_3^-
E-region	$90 \lesssim h \lesssim 170\,\mathrm{km}$	O_2^+, NO^+
F-region	$170 \lesssim h \lesssim 1000\,\mathrm{km}$	O^+

A classification of the ionosphere will be done using the ion composition. Figure 2.2 shows two plots of ion composition of the ionosphere versus height for midnight and noon conditions. The data for these plots has been created feeding the IRI model with location and time corresponding to JRO and January 15, 2015. Table 2.1, found in *Prölss* [2004], shows the main constituents found in the D, E and F regions at typical range of altitudes. The F-region is the atomic oxygen ion region; the E-region is dominated by O_2^+ and NO^+; the lowermost region of the ionosphere is the D-region and is where cluster ions and negative ions play an important role.

2.1.1 The equatorial valley region

The right part of Figure 2.1 identifies the E-F valley region between 120 and 180 km. At nighttime, the region clearly shows a reduction in electron density which emphasizes the valley shape between the denser E and F regions. Some important characteristics of this region are summarized in *Chau et al.* [2009] as follows:

1. In this region occurs the transition between the dominant molecular ions of lower altitudes [O_2^+, NO^+, N_2^+] and F-region dominant atomic oxygen ion [O^+].

2. Collisions with neutrals start to be less important as the altitude increases.

3. Electron coulomb collisions need to be considered for angles close to perpendicular, i.e., for $< 3^\circ$ (e.g. *Kudeki and Milla* [2011]).

4. At the magnetic equator, magnetic field lines around 140–170 km are mapped to both the north and south E-regions that are located outside the equatorial electrojet (EEJ) belt.

5. So called "intermediate layers" are known to occur at these altitudes at mid-latitudes, but so far they have not been observed at equatorial regions during the day.

6. Large electron to ion (and therefore neutral) temperature ratios are expected and observed during the day.

7. Maximum photoelectron production rate occurs around 150 km (e.g. *Su et al.* [1998]). Recently, *Oppenheim and Dimant* [2016] demonstrated through simulations that energetic photoelectrons can cause the enhancement of radar measurements of plasma lines and ion lines around 150 km of altitude.

8. Altitudes below 200 km are difficult to explore with ISR techniques at magnetic equator regions due to the presence of coherent 150-km echoes, and other ionospheric irregularities causing strong coherent echoes, like EEJ, meteor head and trails (e.g. *Chau and Woodman* [2005]; *Chau and Kudeki* [2006]).

9. Only a handful of in-situ measurements have been performed with rockets, but the probes did not observe any strong evidence for large scale plasma irregularities or sharp density gradients (e.g. *Prakash et al.* [1969]).

10. *Reyes* [2012] studied the ionospheric effects of solar flares over Jicamarca and found that the 150-km echoes experienced changes in shape and location for flares with magnitudes as low as M3.5.[3] Layers seem to be pushed downwards by the enhanced ionizing solar radiation. And depending on the solar flare strength, the $\mathbf{E} \times \mathbf{B}$ drift calculated from the 150-km echoes could experience a drop about 18 m/s for the case of a strong solar flare (e.g., X17.1).

11. Backscatter from VHF radars exhibits mainly two distinct types of the 150 km echoes [*Chau and Kudeki*, 2013]. One is related to naturally enhanced incoherent scatter (NEIS) and the other one is related to field-aligned irregularities (FAI). At Jicamarca, NEIS 150-km echoes constitute the majority, while FAI 150-km echoes are the minority. In that paper, the scattering due to NEIS was given the name of type A echoes, while scattering due to FAI was given the name of type B echoes. In the type A echoes, the Doppler spectral width increases with signal strength, while type B echoes of higher signal-to-noise (SNR) exhibit much narrower SNR-independent Doppler spectral widths.

2.1.2 Propagation of radio waves in magnetized plasmas, derivation of Appleton-Hartree equation

In this section the propagation modes for high frequency (HF) waves traveling with a wave propagation vector $\mathbf{k}$ at a magnetic aspect angle α are derived. This topic is relevant for HF and VHF probing of the magnetized valley region

---

[3] X-ray flare classification is done according to energy flux in the X-ray emission band $1-8$ Å measured near Earth in W/m^2. In the notation, the prefix X means 10^{-4} W/m^2, while M means 10^{-5} W/m^2[from *Hargreaves*, 1992]. Therefore an M3.5 flare means that a peak energy flux of 3.5×10^{-5} W/m^2 was detected near Earth, while a solar flare classified as X17.1 corresponds to a detected peak energy flux of 17×10^{-4} W/m^2.

ionosphere with ionosonde and incoherent scatter radar systems.

Figure 2.3 shows the geometric framework used in our derivations. We start from Maxwell's curl equations in differential form

$$\begin{aligned} \nabla \times \mathbf{E} &= -\frac{\partial \mathbf{B}}{\partial t}, && (2.1) \\ \nabla \times \mathbf{H} &= \mathbf{J} + \frac{\partial \mathbf{D}}{\partial t}. && (2.2) \end{aligned}$$

Assuming time-harmonic wave solutions exhibiting the planar phasor form

$$\mathbf{E} = \mathbf{E}_o e^{j\omega t - j\mathbf{k}\cdot\mathbf{r}}, \tag{2.3}$$

where ω is the wave frequency, $\mathbf{k}$ is the wave propagation vector, and $\mathbf{r}$ is the position vector, we obtain the plane-wave form of Maxwell's curl equations

$$\begin{aligned} -j\mathbf{k} \times \mathbf{E} &= -j\omega\mu_o\mathbf{H}, && (2.4) \\ -j\mathbf{k} \times \mathbf{H} &= \overline{\overline{\sigma}} \cdot \mathbf{E} + j\omega\epsilon_o\mathbf{E}, && (2.5) \end{aligned}$$

where the differential operators ∇ and $\partial/\partial t$ have been replaced by $-j\mathbf{k}$ and $j\omega$, respectively. In these equations we have assumed propagation in a magnetized plasma with $\epsilon = \epsilon_o$, $\mu = \mu_\circ$, and $\mathbf{J} = \overline{\overline{\sigma}} \cdot \mathbf{E}$, where $\overline{\overline{\sigma}}$ is a conductivity tensor which accounts for free charge carriers. Also we have used $\mathbf{B} = \mu_o\mathbf{H}$ and $\mathbf{D} = \epsilon_o\mathbf{E}$. We combine equations (2.4) and (2.5) by taking $(\mathbf{k}\times)$ to equation (2.4) and find

$$\mathbf{k} \times \mathbf{k} \times \mathbf{E} = \frac{\omega\mu_o}{-j}\left(\overline{\overline{\sigma}} \cdot \mathbf{E} + j\omega\epsilon_o\mathbf{E}\right), \tag{2.6}$$

from which we obtain

$$-k^2\mathbf{E}_\perp = j\omega\mu_o\overline{\overline{\sigma}} \cdot \mathbf{E} - k_o^2\mathbf{E}, \tag{2.7}$$

where $k_o \equiv \omega\sqrt{\mu_o \epsilon_o}$ is the free-space wavenumber, and $\mathbf{E}_\perp$ is the component of $\mathbf{E}$ perpendicular to $\hat{k}$. But since $\mathbf{k} = k_o n \hat{k}$, where n is the refractive index, we obtain

$$\frac{\overline{\overline{\sigma}} \cdot \mathbf{E}}{j\omega\epsilon_o} = n^2 \mathbf{E}_\perp - \mathbf{E}. \tag{2.8}$$

To derive the conductivity tensor $\overline{\overline{\sigma}}$ we consider a cold, collisionless, magnetized plasma. Applying Newton's second law to an electron immersed in the plasma under the action of the Coulomb and Lorentz forces we have

$$m_e \frac{d\mathbf{v}}{dt} = -e\left(\mathbf{E} + \mathbf{v} \times \mathbf{B}\right), \tag{2.9}$$

where m_e is the electron mass, and $-e$ is the electron charge. Also $\mathbf{B} = \mathbf{B}_o + \mathbf{B}_{\text{wave}}$ is the magnetic field experienced by the electron, where $\mathbf{B}_{\text{wave}}$, the wave magnetic field, is much weaker than the background Earth's magnetic field $\mathbf{B}_o$. In phasor form, and since $\mathbf{B}_o \gg \mathbf{B}_{\text{wave}}$, we can rewrite equation (2.9) as

$$j\omega m_e \mathbf{v} = -e\mathbf{E} + e\mathbf{B}_o \times \mathbf{v}. \tag{2.10}$$

Multiplying this equation by the number electron density N_o and the elementary charge e and dividing by $j\omega m_e$, we obtain

$$eN_o\mathbf{v} = -\frac{N_o e^2}{j\omega m_e}\mathbf{E} + \frac{e}{j\omega m_e}\mathbf{B}_o \times eN_o\mathbf{v}. \tag{2.11}$$

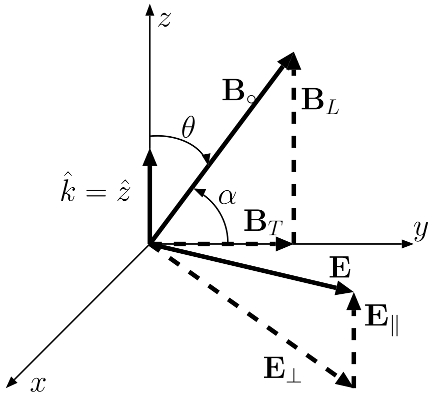

Figure 2.3 – Coordinate system used as a framework for the propagation of radio waves in magnetized plasmas. The propagation vector $\hat{k}$ is parallel to the z axis. The background magnetic field $\mathbf{B}_\circ$ is assumed to be on the yz-plane at an angle θ from the wave propagation direction $\hat{k}$. The magnetic aspect angle α is the complementary angle of θ. $\mathbf{B}_\circ$ has a longitudinal component $\mathbf{B}_L$, parallel to $\hat{k}$, and a transversal component $\mathbf{B}_T$, perpendicular to $\hat{k}$ in the yz-plane. The wave field $\mathbf{E}$ is characterized with a parallel to $\hat{k}$ component, $\mathbf{E}_\parallel$, and a perpendicular to $\hat{k}$ component, $\mathbf{E}_\perp$.

We now define $\mathbf{J} = -eN_o\mathbf{v}$ as the current density phasor, neglecting the current generated by the heavy ions,

$$\Omega_e \equiv \frac{eB_o}{m_e} \tag{2.12}$$

as the electron gyro-frequency, and

$$\omega_p = \sqrt{\frac{N_o e^2}{m_e \epsilon_o}} \tag{2.13}$$

as the plasma frequency. We also adopt the classic magneto-ionic notation:

$$X \equiv \frac{\omega_p^2}{\omega^2} = \frac{N_o e^2}{m_e \epsilon_o \omega^2},\ Y \equiv \frac{\Omega_e}{\omega} = \frac{eB_o}{\omega m_e},\ Y_L = Y\cos\theta,\ Y_T \equiv Y\sin\theta, \tag{2.14}$$

given that

$$\mathbf{B}_o = \mathbf{B}_T + \mathbf{B}_L = B_o\left(\hat{y}\sin\theta + \hat{z}\cos\theta\right), \tag{2.15}$$

as shown in Figure 2.3. With the new definitions, equation (2.11) can be rewritten as

$$\mathbf{J} = -j\omega\epsilon_o X\mathbf{E} - jY_T\hat{y} \times \mathbf{J} - jY_L\hat{z} \times \mathbf{J}, \tag{2.16}$$

and breaking it into their scalar components we have

$$\begin{aligned} -j\omega\epsilon_o XE_x &= J_x + jY_T J_z - jY_L J_y, && (2.17) \\ -j\omega\epsilon_o XE_y &= J_y + jY_L J_x, && (2.18) \\ -j\omega\epsilon_o XE_z &= J_z - jY_T J_x. && (2.19) \end{aligned}$$

We also break vector equation (2.8) into their scalar components, and obtain

$$\begin{aligned} \left(n^2 - 1\right) E_x &= \frac{J_x}{j\omega\epsilon_o}, && (2.20) \\ \left(n^2 - 1\right) E_y &= \frac{J_y}{j\omega\epsilon_o}, && (2.21) \\ -E_z &= \frac{J_z}{j\omega\epsilon_o}. && (2.22) \end{aligned}$$

We will re-write these equations, for $n^2 - 1 \neq 0$, in terms of the ratios

$$\begin{aligned} \frac{E_x}{E_y} &= \frac{J_x}{J_y} \equiv R, && (2.23) \\ \frac{E_z}{E_x} &= \frac{J_z}{J_x}\left(1 - n^2\right) \equiv S. && (2.24) \end{aligned}$$

Using equation (2.22) with equation (2.19) we get

$$J_z = \frac{1}{X}\left(J_z - jY_T J_x\right) \;\Rightarrow\; \frac{J_z}{J_x} = j\frac{Y_T}{1 - X}. \tag{2.25}$$

Dividing equation (2.17) by J_x, and using equation (2.25) yields

$$-j\omega\epsilon_o X\frac{E_x}{J_x} = 1 - \frac{Y_T^2}{1 - X} - j\frac{Y_L}{R}. \tag{2.26}$$

Now we divide equation (2.18) by J_y to obtain

$$-j\omega\epsilon_o X\frac{E_y}{J_y} = 1 + jY_L R. \tag{2.27}$$

Since from equation (2.23), $E_x/J_x = E_y/J_y$, we notice that the left parts of equations (2.26) and (2.27) are the same. Therefore,

$$-\frac{Y_T^2}{1-X} - j\frac{Y_L}{R} = jY_L R, \tag{2.28}$$

which yields

$$jY_L R^2 + \frac{Y_T^2}{1-X}R + jY_L = 0. \tag{2.29}$$

Solving the second order equation (2.29) we obtain

$$R = \frac{-\frac{Y_T^2}{1-X} \pm \sqrt{\frac{Y_T^4}{(1-X)^2} + 4Y_L^2}}{j2Y_L} = \frac{1}{-jY_L}\left\{\frac{Y_T^2}{2\left(1-X\right)} \mp \sqrt{\frac{Y_T^4}{4\left(1-X\right)^2} + Y_L^2}\right\}. \tag{2.30}$$

For convenience we define

$$F \equiv -jY_L R = \frac{Y_T^2}{2\left(1-X\right)} \mp \sqrt{\frac{Y_T^4}{4\left(1-X\right)^2} + Y_L^2}. \tag{2.31}$$

Next, we combine equations (2.18) and (2.21) as

$$n^2 - 1 = \frac{-XJ_y}{J_y + jY_L J_x} = \frac{-X}{1 + jY_L R} = \frac{-X}{1-F}, \tag{2.32}$$

which yields the refractive index formula

$$n^2 = 1 - \frac{X}{1-F}, \tag{2.33}$$

which is known as the Appleton-Hartree equation [e.g. *Davies*, 1969]. Finally, from equations (2.22) and (2.19) we get S in terms of Y_T, n, and X

$$1 - X = jY_T \frac{J_x}{J_z} = jY_T \frac{(1-n^2)}{S} \Rightarrow S = \frac{E_z}{E_x} = \frac{jY_T\,(1-n^2)}{1-X}. \tag{2.34}$$

2.1.3 Propagation perpendicular to $\mathbf{B}_o$: ordinary and extraordinary waves

While the Appleton-Hartree equation is valid for any propagating radio frequency ω and any propagation direction $\mathbf{k}$ with an arbitrary magnetic aspect angle α, in this section we are going to analyze the case of propagation perpendicular to the background magnetic field $\mathbf{B}_o$. In the case of propagation with exactly zero magnetic aspect angle we have $\mathbf{B}_o = B_o\,\hat{y}$, $\theta = \frac{\pi}{2}$, $Y_T = Y$, and $Y_L = 0$. Therefore, from equation (2.31) we obtain the two possible values of F:

$$F_- = 0, \text{ and } F_+ = \frac{Y^2}{1-X}. \tag{2.35}$$

Ordinary wave The first mode, i.e. when $F = 0$, is called ordinary mode (O-mode). From equation (2.33) we obtain the refractive index formula for the ordinary wave

$$n_-^2 = 1 - X. \tag{2.36}$$

Using l'Hospital's rule in equation (2.30) we obtain the ratio

$$R = \frac{E_x}{E_y} = \lim_{\theta \to \frac{\pi}{2}} -\frac{F_-}{jY_L} = 0. \tag{2.37}$$

This result implies that $E_x = 0$. Finally, equation (2.34) simplifies to

$$S = \frac{E_z}{E_x} = j\frac{Y}{\frac{1}{X} - 1} \neq 0, \tag{2.38}$$

which yields $E_z = 0$. Therefore, the ordinary wave is a linearly polarized wave along the direction of $\mathbf{B}_o = B_o\hat{y}$.

Extraordinary wave The second possible mode of propagation, i.e. when $F = \frac{Y^2}{1-X}$, is called extraordinary mode (X-mode). From equation (2.33) we obtain the refractive index formula for the ordinary wave

$$n_+^2 = 1 - \frac{X(1-X)}{1-X-Y^2}. \tag{2.39}$$

Using l'Hospital's rule in equation (2.30) we obtain the ratio

$$R = \frac{E_x}{E_y} = \lim_{\theta \to \frac{\pi}{2}} -\frac{F_+}{jY_L} = \infty. \tag{2.40}$$

This result implies that $E_y = 0$. Finally, from equation (2.34) we get

$$S = \frac{E_z}{E_x} = j\frac{YX}{1-X-Y^2}, \tag{2.41}$$

which is purely imaginary. Therefore, the extraordinary wave is elliptically polarized, and since $E_z = SE_x \neq 0$, this is not a transverse-electromagnetic (TEM) wave.

2.1.4 Vertical incidence ionospheric sounding, ionograms, group velocities and virtual height model

A narrowband pulsed radio wave transmission propagating vertically through the ionosphere goes through a total reflection at height $z_r(\omega_o)$ as one can see in the representation of the path followed by the transmitted pulse with thin continuous black arrows in Figure 2.4. For ordinary waves that height is where $n_-^2 = 0$. Using equation (2.36) the reflection height for O-mode is where $X = 1$, i.e. where the local value of plasma frequency equals ω_o. For the extraordinary mode of propagation the wave is reflected at the height where $n_+^2 = 0$. Letting equation (2.39) be zero, we obtain

$$(1 - X)^2 = Y^2, \tag{2.42}$$

which yields $X = 1 - Y$ if $Y < 1$ and $X = 1 + Y$ if $Y > 1$. The pulse returns back to $z = 0$ after having travelled a total distance of $2z_r(\omega_o)$ at the ionospheric group speed

$$v_g = \frac{c}{n_g} = \frac{dz}{d\tau}, \tag{2.43}$$

where c is the speed of light, n_g is the group refractive index, z is the traveled height, and τ is the group delay. The group refractive index is defined in terms of the refractive index n as

$$n_g \equiv \frac{\partial}{\partial \omega}(n\omega) = \frac{\partial}{\partial f}(nf). \tag{2.44}$$

Virtual height is the distance that the wave would have traveled at the speed of light c. The virtual height path is depicted with dashed lines in Figure 2.4. Hence, the variation in virtual height due to a variation in group delay $d\tau$ is defined as

$$dh' = c d\tau, \tag{2.45}$$

which combined with equation (2.43) becomes

$$dh' = n_g dz. \tag{2.46}$$

Therefore, to obtain the virtual height for a given transmitted frequency, we integrate equation (2.46) from the ground until the reflection height

$$h' = \int_0^{z_r} n_g(z)dz. \tag{2.47}$$

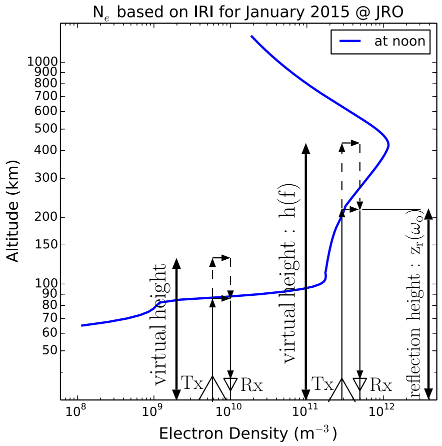

Figure 2.4 – Vertical incidence ionospheric sounding. The electron density profile is similar to that shown in right of Figure 2.1.

Next, we are going to derive the group refractive index. We start evaluating equation (2.44):

$$n_g = \frac{\partial}{\partial f}(nf) = n + f\frac{\partial n}{\partial f} = n + f\left(\frac{\partial n}{\partial X}\frac{\partial X}{\partial f} + \frac{\partial n}{\partial Y}\frac{\partial Y}{\partial f}\right). \tag{2.48}$$

From the definitions in (2.14) we have

$$X = \frac{f_p^2}{f^2} \qquad \Rightarrow \qquad \frac{\partial X}{\partial f} = -2\frac{f_p^2}{f^3} = -\frac{2X}{f}, \tag{2.49}$$

and

$$Y = \frac{\Omega}{2\pi f} \qquad \Rightarrow \qquad \frac{\partial Y}{\partial f} = -\frac{\Omega}{2\pi f^2} = -\frac{Y}{f}. \tag{2.50}$$

Substituting $\partial X/\partial f$ and $\partial Y/\partial f$ in equation (2.48) we obtain

$$n_g = n - 2X\frac{\partial n}{\partial X} - Y\frac{\partial n}{\partial Y}. \tag{2.51}$$

For convenience, we multiply (2.51) by n, which simplifies to

$$nn_g = n^2 - X\frac{\partial n^2}{\partial X} - \frac{1}{2}Y\frac{\partial n^2}{\partial Y}. \tag{2.52}$$

For the terms with n^2, we can use the magneto-ionic (MI) refractive index formula (2.33). Now we are going to analyze the two cases described in subsection 2.1.3, the O- and X-modes. For the O-mode we have

$$n^2 = 1 - X \qquad \Rightarrow \qquad \frac{\partial n^2}{\partial X} = -1,\ \frac{\partial n^2}{\partial Y} = 0 \qquad \therefore \qquad nn_g = 1 - X + X = 1, \tag{2.53}$$

which yields the group refractive index for O-mode

$$n_g = \frac{1}{n} = \frac{1}{\sqrt{1-X}} = \frac{1}{\sqrt{1-\frac{f_p^2}{f^2}}}. \tag{2.54}$$

For the X-mode we take the derivative of equation (2.39) with respect to X, and obtain

$$\begin{aligned}
\frac{\partial n^2}{\partial X} &= -\frac{(1-2X)\left(1-X-Y^2\right)+X\left(1-X\right)}{\left(1-X-Y^2\right)^2} \\
&= \frac{-\left(1-2X\right)}{\left(1-X-Y^2\right)}\frac{X\left(1-X\right)}{X\left(1-X\right)} + \frac{-X\left(1-X\right)}{\left(1-X-Y^2\right)^2} && (2.55)\\
&= \left(n^2-1\right)\frac{\left(1-2X\right)}{X\left(1-X\right)} + \frac{\left(n^2-1\right)}{\left(1-X-Y^2\right)} && (2.56)\\
&= \left(n^2-1\right)\left[\frac{1}{1-X-Y^2} + \frac{1-2X}{X\left(1-X\right)}\right]. && (2.57)
\end{aligned}$$

Next, we take the derivative of equation (2.39) with respect to Y, and obtain

$$\frac{\partial n^2}{\partial Y} = -\frac{2YX\left(1-X\right)}{\left(1-X-Y^2\right)^2} = \frac{2Y\left(n^2-1\right)}{1-X-Y^2}. \tag{2.58}$$

Inserting equations (2.56) and (2.58) in equation (2.52) yields

$$\begin{aligned} nn_g &= n^2 + \left(1-n^2\right)\left[\frac{X}{1-X-Y^2} + \frac{1-2X}{1-X} + \frac{Y^2}{1-X-Y^2}\right] \\ &= n^2 + \left(1-n^2\right)^2 \frac{1-X-Y^2}{X\left(1-X\right)}\left[\frac{X+Y^2}{1-X-Y^2} + 1 - \frac{X}{1-X}\right] \\ &= n^2 + \left(1-n^2\right)^2 \left[\frac{X+Y^2}{X\left(1-X\right)} + \frac{1-X-Y^2}{X\left(1-X\right)} - \frac{1-X-Y^2}{\left(1-X\right)^2}\right] \\ &= n^2 + \left(1-n^2\right)^2 \left[\frac{1}{X\left(1-X\right)} - \frac{1}{1-X} + \frac{Y^2}{\left(1-X\right)^2}\right] \\ &= n^2 + \left(1-n^2\right)^2 \left[\frac{1}{X} + \frac{Y^2}{\left(1-X\right)^2}\right]. \end{aligned} \tag{2.59}$$

We are going to use these results next in order to obtain a forward model relating electron density distributions and ionograms.

2.1.5 Modeling the vertical ionospheric sounding in an inhomogeneous ionosphere

We are going to consider a plane wave propagating in an inhomogeneous magnetized ionosphere at the geomagnetic equator in a direction $\hat{k}$ perpendicular to the Earth's magnetic field $\mathbf{B}_o$. To model the virtual height of the propagating wave, we will divide the ionosphere in slabs of equal width perpendicular to the propagation direction such that within each slab the physical plasma parameters can be considered constants. As the radio wave travels through the ionosphere, the refractive index, n, experiences different values, until it gets to very close to zero when approaching the reflection height. We need to pay special attention to the last slab, because as $n \to 0$, the wave group velocity, c/n_g, decreases significantly, contributing to a larger virtual height. For this reason, we will use the following method to calculate the virtual height, where the contribution of the last slab is evaluated analytically:

$$h'(f) = \sum_{\text{all but last slab}} \Delta z \bar{n}_{gi} + \int_{z_b}^{z_r} n_g(z) dz, \tag{2.60}$$

where Δz is the slab width, z_b is the height of the bottom of the last slab, z_r is the reflection height, and $\bar{n}_g$ is an average refractive index of the slab, calculated as

$$\bar{n}_{gi} = \frac{n_{gib} + n_{git}}{2}, \tag{2.61}$$

where n_{gib} and n_{git} are the group refractive indexes at the bottom and the top of the i-th slab respectively. To approximate n_g in the last slab, we are going to consider a linear variation of n^2 with respect to z (see Figure 2.5). Using Figure 2.5 we can express n^2 for the last slab as

$$n^2(z) = n_b^2 - \frac{(n_b^2 - n_t^2)}{\Delta z} (z - z_b), \tag{2.62}$$

where n_b and n_t are the refractive indexes at the bottom and the top of the last slab. Next, we calculate the reflection height, i.e. when $n^2(z) = 0$

$$0 = n^2(z_r) = n_b^2 - \frac{(n_b^2 - n_t^2)}{\Delta z} (z_r - z_b) \qquad \Rightarrow \qquad z_r = z_b + \frac{n_b^2 \Delta z}{n_b^2 - n_t^2}. \tag{2.63}$$

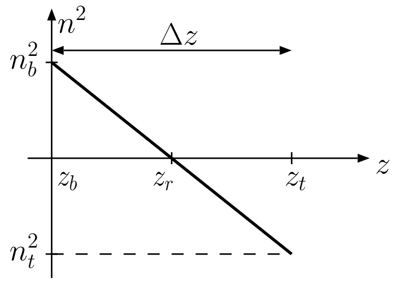

Figure 2.5 – Modeling n^2 with a linear approximation for the last slab of width Δz.

For the O-mode, we know from equation (2.54) that $n_g = 1/n$. Therefore, we can calculate the integral in equation (2.60) analytically

$$\int_{z_b}^{z_r} n_g(z)dz = \int_{z_b}^{z_r} \frac{dz}{\sqrt{n_b^2 - \frac{1}{\Delta z}\left(n_b^2 - n_t^2\right)\left(z - z_b\right)}}$$

$$= \int_0^{\frac{n_b^2 \Delta z}{n_b^2 - n_t^2}} \frac{dz'}{\sqrt{n_b^2 - \frac{1}{\Delta z}\left(n_b^2 - n_t^2\right) z'}} = \frac{2 n_b \Delta z}{n_b^2 - n_t^2}. \tag{2.64}$$

For the X-mode, we are going to use a simplified version nn_g in equation (2.59). Let us define

$$\epsilon \equiv 1 - Y - X. \tag{2.65}$$

According to *Davies* [1969], for small ϵ, an approximation for the extraordinary mode refractive index can be written as

$$n^2 \cong \frac{2\epsilon}{1 - Y}, \tag{2.66}$$

while the group refractive index can be approximated as

$$n_g \cong \frac{2 - Y}{\sqrt{2\epsilon\left(1 - Y\right)}}. \tag{2.67}$$

Finally, it can be shown that for the X-mode, the virtual height over the last slab is

$$\Delta h' = \int_{z_b}^{z_r} n_g(z)dz = \frac{2n_b\Delta z}{n_b^2 - n_t^2}\left(\frac{2-Y}{1-Y}\right). \tag{2.68}$$

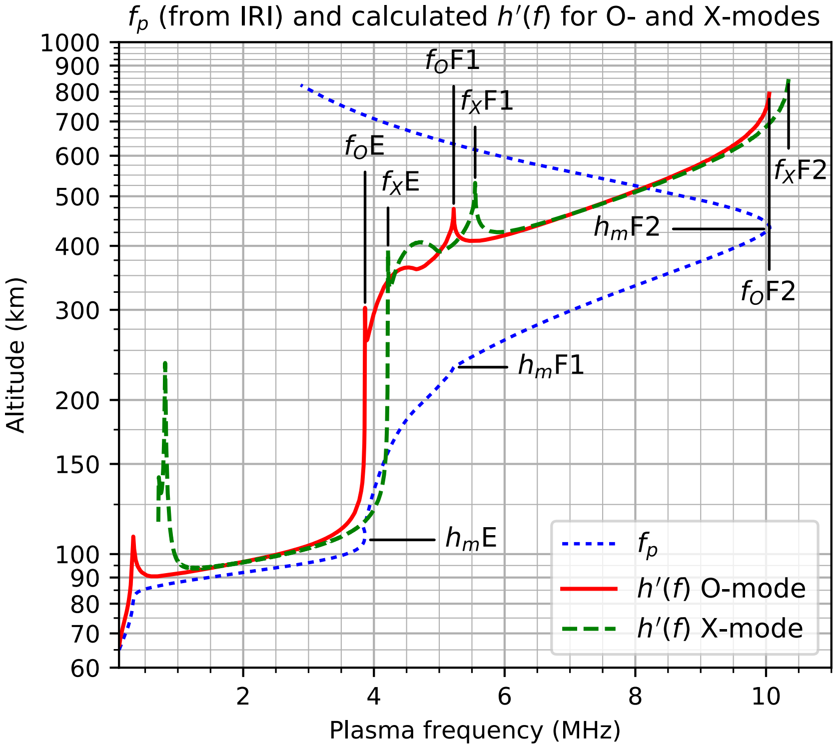

Figure 2.6 – Ordinary and extraordinary ionogram traces calculated for the ionosphere shown in Figure 2.1. This figure also shows the conventional nomenclature for the critical frequencies in ionogram traces [e.g. *Rishbeth and Garriott*, 1969].

As a practical note for implementing this forward model one should consider the last two slabs for the analytical integral. The reason for that consideration is that within the last slab, the reflecting height z_r could be very close to the bottom of the slab. In those cases the integral will be more accurate if the combination of the last two slabs is considered as a larger last slab for the analytical calculation. Instead of paying attention to how close the reflecting height is from the bottom of the last slab, considering always the last two slabs for the analytical integral avoids extra complications to the forward model algorithm.

Figure 2.6 shows the O- and X-mode calculated virtual heights $h'(f)$ for the dayside ionosphere obtained with the IRI model for January 15, 2015 (same as in the right side of Figure 2.1). The O- and X-traces were calculated using formulas (2.60), (2.64), and (2.68). To obtain the magnitude of the magnetic field at a given height, the International Geomagnetic Reference Field (IGRF) model [e.g., *Thébault et al.*, 2015] was used. In the same graph there are annotations of typical critical frequencies (or penetration frequencies) of the layers found in ionogram traces [e.g. Figure 10 in *Rishbeth and Garriott*, 1969].

2.1.6 Quasi-longitudinal propagation

For sufficiently large frequencies ω compared to the plasma frequency ω_p and the electron gyro-frequency Ω_e of the ionosphere, the condition $Y_T^2 \ll 2Y_L(1-X)$ is valid over nearly all propagation angles θ between $\hat{k}$ and $\mathbf{B}_o$ (see Figure 2.3). As a consequence, F in equation (2.31) becomes

$$F = \frac{Y_T^2 \mp \sqrt{Y_T^4 + 4Y_L^2(1-X)^2}}{2(1-X)} \approx \mp Y_L = \mp Y\cos\theta, \tag{2.69}$$

which yields the refractive indices

$$n^2 = 1 - \frac{X}{1-F} \approx 1 - \frac{X}{1 \pm Y_L}, \tag{2.70}$$

and the ratio of the wave electric field components orthogonal to the propagation direction

$$R = \frac{E_x}{E_y} = \frac{jF}{Y_L} \approx \mp j. \tag{2.71}$$

This corresponds to right- and left-circular quasi-longitudinal modes, which can be shown to be also quasi-TEM in the sense that $|E_z|^2 \ll |\mathbf{E}_\perp|^2$. The quasi-longitudinal condition

$$Y_T^2 \ll 2Y_L\,(1-X) \tag{2.72}$$

implies that

$$\tan\theta\sin\theta \ll 2\frac{1-X}{Y}. \tag{2.73}$$

This condition holds for relatively small ω, over a very narrow band of θ centered about $\theta = 0^\circ$. For larger frequencies $\omega \gg \omega_p$ and $\omega \gg \Omega_e$ the same condition can be approximated by

$$\tan\theta\sin\theta \ll 2\frac{1-X}{Y} = 2\frac{\omega^2-\omega_p^2}{\omega\Omega_e} \approx \frac{2\omega}{\Omega_e}, \tag{2.74}$$

and has a very broad range of validity in θ. Since $\sin\theta \leq 1$, we can turn the condition into

$$\theta \ll \tan^{-1}\frac{2\omega}{\Omega_e}. \tag{2.75}$$

For the Jicamarca VHF 50 MHz incoherent scatter radar, $\omega \approx 2\pi \times 50 \times 10^6\,\mathrm{rad/s} \approx 3.14 \times 10^8\,\mathrm{rad/s}$. At an altitude of 200 km the magnitude of the Earth's magnetic field is about 23000 nT, which yields $\Omega_e = eB_o/m_e \approx 4.05 \times 10^6\,\mathrm{rad/s}$. Consequently the condition becomes $\theta \ll 89.63^\circ$.

2.1.7 Faraday rotation

A linearly polarized quasi-longitudinal wave will excite the two quasi-circular polarized modes. Each mode with its respective refractive index as described by equation (2.70) is

$$n_m^2 = 1 - \frac{X}{1-mY\cos\theta}, \tag{2.76}$$

where $m = \pm 1$ accounts for the two possible modes. The linearly polarized wave can be expressed as a pair of circular polarized waves

$$\mathbf{E} = (\hat{x} - j\hat{y})\, e^{\pm jk_o n_{+1} z} + (\hat{x} + j\hat{y})\, e^{\pm jk_o n_{-1} z}, \tag{2.77}$$

where $\pm$ accounts for the wave propagating in the $\mp\hat{z}$ directions. Using the definitions

$$\bar{n} = \frac{n_{+1} + n_{-1}}{2}, \qquad \text{and} \qquad \delta n = n_{-1} - n_{+1}, \tag{2.78}$$

equation (2.77) becomes

$$\mathbf{E} = 2e^{\pm jk_o \bar{n} z} \left[\hat{x} \cos\left(k_o \frac{\delta n}{2} z \right) \pm \hat{y} \sin\left(k_o \frac{\delta n}{2} z \right) \right]. \tag{2.79}$$

We notice that $\mathbf{E}$ is linearly polarized at an angle

$$\rho = \frac{k_o \delta n}{2} z \,\text{rad} \tag{2.80}$$

with respect to $\hat{x}$. It can be shown that for small X and Y, the Faraday rotation angle can be approximated by

$$\rho \approx \frac{40.3 \Omega N_e \cos\theta}{c f^2} r, \tag{2.81}$$

where N_e is the plasma density in m^{-3}, and $r = |z|$ is the total path that the wave has traveled. The previous result assumes a homogeneous magneto-plasma. To apply the Faraday technique to the inhomogeneous ionosphere, where $N_e = N_e(r)$, $\Omega_e = \Omega_e(r)$, and $\theta = \theta(r)$ are functions of altitude, we need to divide the ionosphere into slabs. In the infinitesimal slab, the change in Faraday rotation over an infinitesimal section dr is

$$d\rho \approx \frac{40.3\Omega_e(r)N_e(r)\cos\theta(r)}{cf^2}dr. \tag{2.82}$$

This result has an important application for remote sensing, since the electron density at a particular distance $N_e(r)$ can be estimated using the derivative of the Faraday rotation with respect to the distance, i.e. $d\rho/dr$. For radar application, the accumulation of rotation will double, since it adds on the way up, and on the way down. We use $r = \frac{ct}{2}$ in equation (2.82), and divide the calculated value by two to get the backscatter radar equation for electron density estimation based on Faraday rotation

$$N\left(\frac{ct}{2}\right) = \frac{f^2}{40.3\Omega_e\left(\frac{ct}{2}\right)\cos\left[\theta\left(\frac{ct}{2}\right)\right]}\frac{d\rho}{dt}. \tag{2.83}$$

2.2 Basic Concepts of Waves in the Neutral Atmosphere

Figure 2.1 shows how the density of neutral particles at the valley region is more that five orders of magnitude larger than the electron density; but as we mentioned in section 2.1.1, above the E-region, the ion-neutral collision frequency start to be less important than the ion gyro frequency, Ω_i. While collision of electrons with neutrals was already low at the E-region considering electrons to be magnetized, [4] it is in the valley region where the ions also start to be considered magnetized. Nevertheless, the impact of the neutral atmosphere dynamics on the ionosphere is manifested in several ways, e.g. the effect of internal gravity waves (IGW) on the electron density contours detected with ionosondes [e.g. *Negrea*

---

[4] A charged atmospheric species is considered to have a magnetized behavior if the gyro frequency is larger than the collision frequency with neutrals, which are the dominant collisions in the ionosphere.

et al., 2016, and this dissertation] and also the effect of gravity waves in the $\mathbf{E}\times\mathbf{B}$ measurements at JRO [e.g. *Kudeki et al.*, 1999; *Varney et al.*, 2009]. Also parallel to the geomagnetic field $\mathbf{B}$ ionospheric plasma readily follows the neutral motion via collisional momentum exchange. Since IGW propagate through our subject of study, the valley region, and have a detectable impact in our measurements both in the 50 MHz radar backscattering data and in VIPIR ionosonde returns, we will discuss next some of their basic characteristics.

2.2.1 Basic equations of internal gravity waves (IGW) through the atmosphere

In this part we do not intend to show any detailed mathematical development of the derivation of the equations governing the atmospheric oscillations. We are particularly interested in showing the reader how the Brunt-Väisälä frequency relates to the gravity wave equations and how it can be calculated. Rigorous calculations and derivations can be found in the literature [e.g. *Hines*, 2013; *Kelley*, 2009; *Hocking et al.*, 2016; *Kudeki*, 1988].

The analysis found in the aforementioned references is based on the assumption that small perturbations of pressure p and mass density ρ, and horizontal and vertical components of the wind $\mathbf{U} = (U_x, 0, U_z)$, all exhibit propagating components with

$$\frac{\delta p}{p} \propto \frac{\delta \rho}{\rho} \propto U_x \propto U_z \propto e^{j(\omega t-(k_x x+k_z z))} \tag{2.84}$$

dependence, where ω is the angular frequency, x and z are the horizontal and vertical position coordinates, k_x is the horizontal wavenumber vector, and k_z is the vertical wavenumber vector. It can be demonstrated [e.g. *Kudeki*, 1988] that in the wind frame, the wave equation of adiabatic pressure perturbations propagating through the atmosphere, assuming isothermal non-rotating conditions with constant horizontal wind and ignoring non-linear effects is

$$\frac{\delta p}{p_0} = A e^{z/2H} e^{j(\omega t - (k_x x + k_z z))}, \tag{2.85}$$

where

$$H = \frac{k_B T}{\langle m \rangle g} \tag{2.86}$$

is the scale height, with T being the absolute temperature, k_B the Boltzmann constant, $\langle m \rangle$ the mean mass of a molecule, and g the gravitational acceleration. The dispersion relation of waves described by equation (2.85) is [e.g. *Kudeki*, 1988]:

$$k_z^2 = \frac{\omega^2}{C_s^2}\left(1 - \frac{\omega_a^2}{\omega^2}\right) - k_x^2\left(1 - \frac{\omega_B^2}{\omega^2}\right), \tag{2.87}$$

or

$$C_s^2\left(k_x^2 + k_z^2 + \frac{\omega_a^2}{C_s^2}\right) = \omega^2 + C_s^2 k_x^2 \frac{\omega_B^2}{\omega^2}, \tag{2.88}$$

where

$$\omega_a^2 = C_s^2 / 4H^2 \tag{2.89}$$

is the square of the acoustic frequency, and

$$\omega_B^2 = (\gamma - 1)\, g^2 / C_s^2 \tag{2.90}$$

is the square of the Brunt-Väisälä frequency. Waves of the type described in equation (2.85) are called acoustic gravity waves (AGW) and support two main types of branches: the acoustic branch, when $\omega > \omega_a$, and the internal gravity wave (IGW) branch, when $\omega < \omega_B$.

In equations (2.87) through (2.90)

$$C_s^2 = \gamma g H, \tag{2.91}$$

is the square of the speed of sound, where γ is the ratio of specific heats at constant pressure and constant volume. For a non-isothermal atmosphere, ω_B can be calculated [e.g. *Kudeki*, 1988] as

$$\omega_B^2 = (\gamma - 1)\,\frac{g^2}{C_s^2} + \frac{g^2}{C_s^2}\,\frac{\partial C_s^2}{\partial z}. \tag{2.92}$$

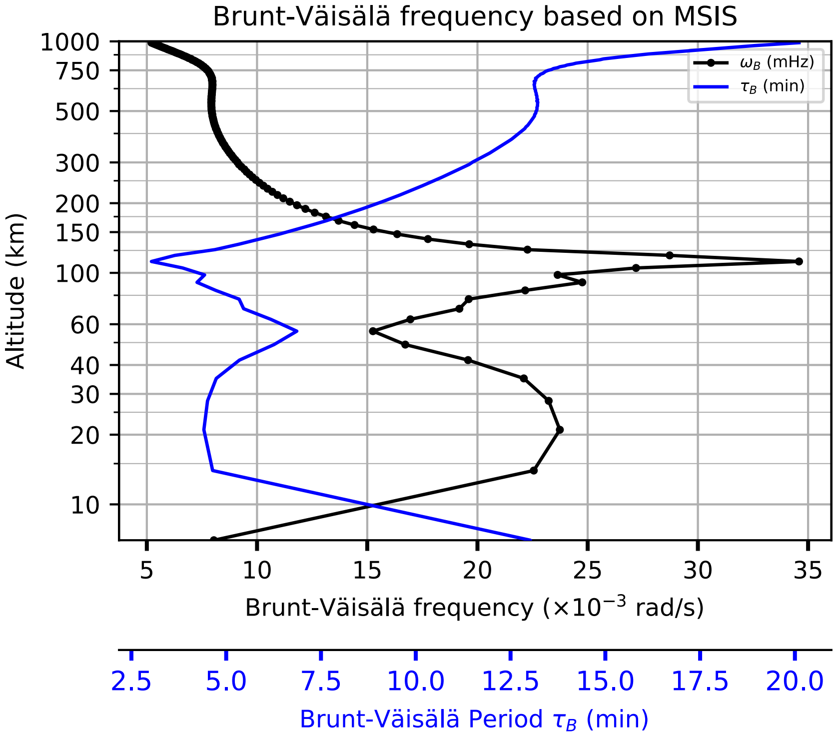

Figure 2.7 – Brunt Väisälä frequency, ω_B and corresponding period, τ_B as a function of height for an atmosphere with parameters obtained from the MSIS model.

Using equation (2.92) with neutral atmosphere parameters obtained from the MSIS model, we calculate the Brunt-Väisälä frequency as a function of height.

Figure 2.7 shows the Brunt-Väisälä frequency ω_B and its corresponding period τ_B in minutes as a function of height.

The physical interpretation of the Brunt-Väisälä frequency alludes to the frequency at which a parcel of air will oscillate if it is moved from its initial position and allowed to oscillate freely. This frequency is also a limit for gravity waves, in the sense that gravity waves with oscillation frequencies larger than ω_B (or with oscillation periods smaller than τ_B) are not allowed. Notice that at the E-F valley region τ_B ranges from about 2.5 minutes around 110 km up to 8 minutes around 200 km. Furthermore, only waves with periods larger than about 6 minutes can enter the region from the lower atmosphere because of the peak in τ_B at about 50 km of altitude. These features of τ_B variation allows the observed 5-15 minute oscillations that we are going to show in the following chapters.

Phase and group velocities

To obtain the horizontal and vertical components of the group velocity we differentiate the dispersion relation in equation (2.88), which yields

$$v_{gx} = \frac{\partial \omega}{\partial k_x} = \frac{\omega C_s^2 k_x \left(\omega^2 - \omega_B^2\right)}{\omega^4 - \omega_B^2 k_x^2 C_s^2} \tag{2.93}$$

and

$$v_{gz} = \frac{\partial \omega}{\partial k_z} = \frac{\omega^3 C_s^2 k_z}{\omega^4 - \omega_B^2 k_x^2 C_s^2}. \tag{2.94}$$

Here we notice an important characteristic of IGW: while for $\omega < \omega_B$ the signs of k_x and v_{gx} are the same, the signs of k_z and v_{gz} are opposite. This implies that if the k_z vector points downwards, the energy is actually propagating upwards.

The Boussinesq approximation for IGW

For the condition

$$\omega^2 \ll C_s^2 \left(k_x^2 + k_z^2 + \frac{\omega_a^2}{C_s^2} \right), \tag{2.95}$$

equation (2.88) reduces to

$$\omega \cong \frac{\omega_B}{\sqrt{k_x^2 + k_z^2 + \left(\frac{1}{2H}\right)^2}} k_x. \tag{2.96}$$

Furthermore, for vertical wave vectors that satisfy the condition

$$k_z H \gg \frac{1}{2}, \tag{2.97}$$

equation (2.96) reduces to

$$\omega \cong \frac{\omega_B}{\sqrt{k_x^2 + k_z^2}} k_x = \frac{\omega_B k_x}{k} \tag{2.98}$$

or

$$\frac{k_x}{k} = \frac{k_x}{\sqrt{k_x^2 + k_z^2}} = \frac{\omega}{\omega_B}. \tag{2.99}$$

The condition in equation (2.97) is called the Boussinesq limit and is valid for a wide class of IGWs observed in the upper atmosphere.

IGW observations on an earth fixed frame

So far our analysis of IGW has been in the wind frame (WF). In order to change our coordinate system from the WF to earth frame (EF) we do the following transformation:

$$\mathbf{r}' = \mathbf{r} + \mathbf{u}_0 t, \tag{2.100}$$

where $\mathbf{r}$ refers to the WF, $\mathbf{r}'$ to the EF, and $\mathbf{u}_0$ is the constant horizontal wind as measured in the EF. Figure 2.8 depicts this scenario. We also assume a zero-mean vertical wind. The wave equation (2.85) can be rearranged as

$$\frac{\delta p}{p_0} = Ae^{z/2H}e^{j(\omega' t-(\mathbf{k}_x\cdot\mathbf{r}'+k_z z'))}, \tag{2.101}$$

where

$$z' = z, \tag{2.102}$$

and

$$\omega' = \omega + \mathbf{k}_x \cdot \mathbf{u}_0 \tag{2.103}$$

is the modified (Doppler shifted) version of the WF frequency, also called the intrinsic frequency. We are going to explore one interesting effect of the Doppler shift. If we use the Boussinesq approximation in equation (2.99) with the EF frequency in equation (2.103), we obtain

$$\frac{k_x}{k} = \frac{\omega' - \mathbf{k}_x \cdot \mathbf{u}_0}{\omega_B}, \tag{2.104}$$

which indicates that if we want to know the horizontal wavenumber, k_x, we need to know the horizontal wind velocity $\mathbf{u}_0$ and the IGW propagation direction $\mathbf{k}_x/k_x$.

A monochromatic IGW in the WF and the corresponding observation by an antenna fixed in the EF are depicted in Figure 2.8. Let us assume that the signal detected by a sounding system using this antenna is proportional to the perturbation created by the IGW. Notice that the maxima of the wave fronts that the sounding system would detect will show downward phase progressions as the monochromatic IGW propagates in the downward $\mathbf{k}$ direction. In the same figure, the horizontal and vertical wavelengths are indicated with λ_x and λ_z

respectively, and the group velocity with v_g.

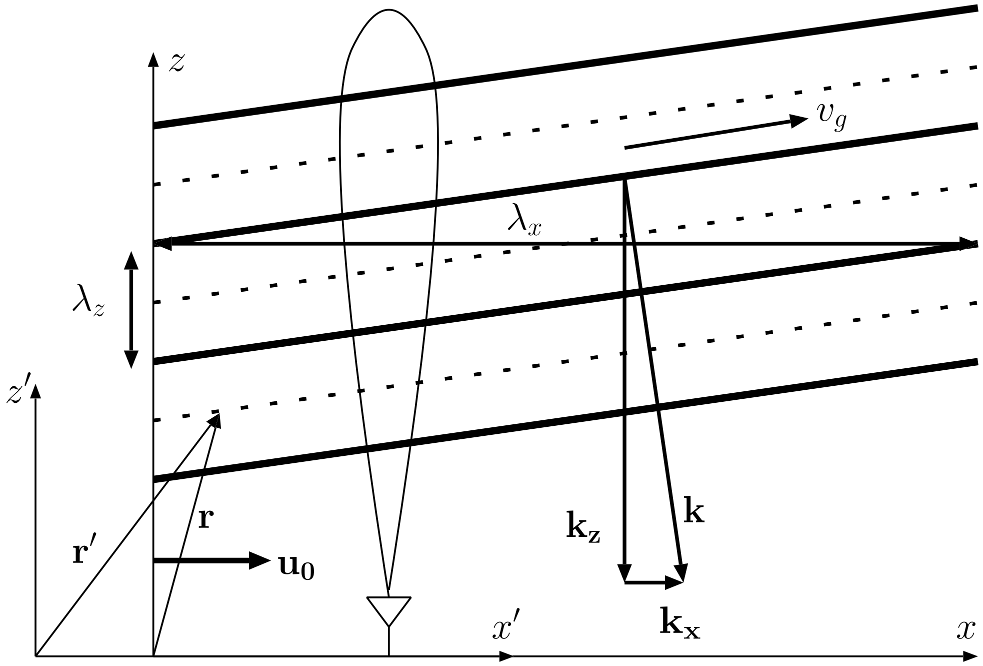

Figure 2.8 – Cartoon of a gravity wave in the WF and an antenna located in the EF. The maxima of the wave fronts are indicated with thick lines perpendicular to the wavenumber $\mathbf{k}$, while the minima of the wave fronts are indicated with dashed lines. WF and EF references shared the z axis, but not necessarily the horizontal axis.

2.2.2 Summary of internal gravity waves (IGW) characteristics

The key characteristic of IGWs discussed are as follows: (1) The oscillation frequency of the IGW must be lower than the Brunt-Väisälä frequency. (2) The oscillation amplitudes grow larger with altitude. (3) Downward phase progression of the waves means upward propagating energy. (4) Short vertical wavelengths are more heavily damped than larger ones due to viscosity [e.g. *Kelley*, 2009]. (5) The horizontal wind velocity $\mathbf{u}_{0h}$, and the direction of propagation of the IGW, $\mathbf{k}_h/k_h$, are needed in order to obtain $\mathbf{k}_h$.

CHAPTER 3

EXPERIMENTAL DESCRIPTION AND OBSERVATIONS

This chapter provides descriptions and data examples of the two instruments used, the Jicamarca incoherent scatter radar (ISR) and its different modes of operation, and the Jicamarca (VIPIR, vertical incidence pulsed ionospheric radar) ionosonde. We start by describing the ISR Valley experiment, and showing some range-time-intensity (RTI) plots together with some spectra and cross-spectra. An example of electron density calculation based on Faraday rotation is presented. After that we describe briefly the MST-ISR-EEJ experiment, and present an RTI of the MST mode showing the 150-km echo layers with high spatial and temporal resolution. We also show some RTIs of the ISR mode. Finally we describe the VIPIR system, and present some data, including ionograms showing their O- and X- curves and some maps of the virtual height and the angle of arrival of the reflected ionosonde pulses.

3.1 The Valley ISR Experiment

The upper part of Figure 3.1 shows a range-time-intensity (RTI) plot of signal-to-noise ratio (SNR) of the backscatter power signal received at JRO during the Valley ISR experiment. The lower part of Figure 3.1 shows an RTI of the phase of the cross-correlation between the cross-polarized antennas 1 and 2. The SNR map contains the characteristic necklace-shaped 150-km echoes in the region from 130 km to 180 km that we have already seen in Figure 1.2. The SNR map also shows the equatorial-electro-jet (EEJ) centered around 100 km. The EEJ signal is more than 40 dB stronger than the noise level and the power seems smeared by a few kilometers above and below as a result of code contamination (binary28). The cross-correlation phase is used to get the Faraday rotation for determining the absolute electron density profile [*Farley*, 1969]. The phase map in Figure 3.1 implies a smooth increase of electron density with height. Figure 3.2 shows the power spectra of cross-polarized antennas 1 and 2, and their cross-correlation normalized magnitude and phase. The two columns on the left represent the wide-band mode. Notice that the spectra are a combination of wide-spectrum and narrow, stronger spectra. According to *Chau and Kudeki* [2013], these correspond to naturally enhanced incoherent scattering (NEIS) and field-aligned irregularities (FAIs).

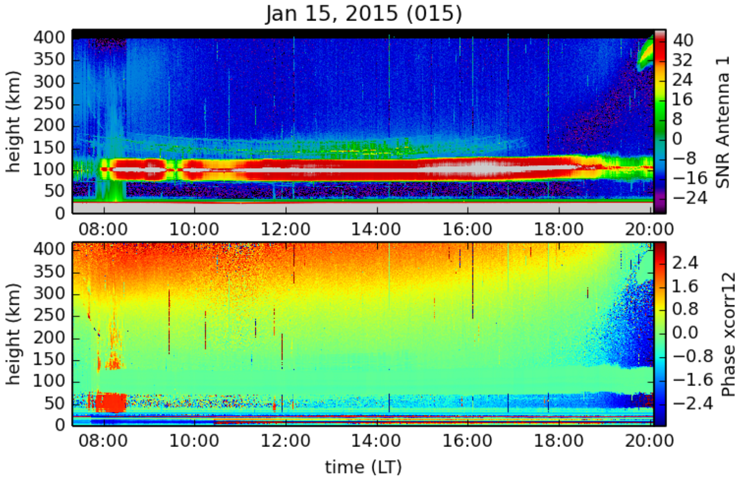

Figure 3.1 – Signal-to-noise (SNR) map and phase map of the cross-correlation between cross-polarized antennas 1 and 2.

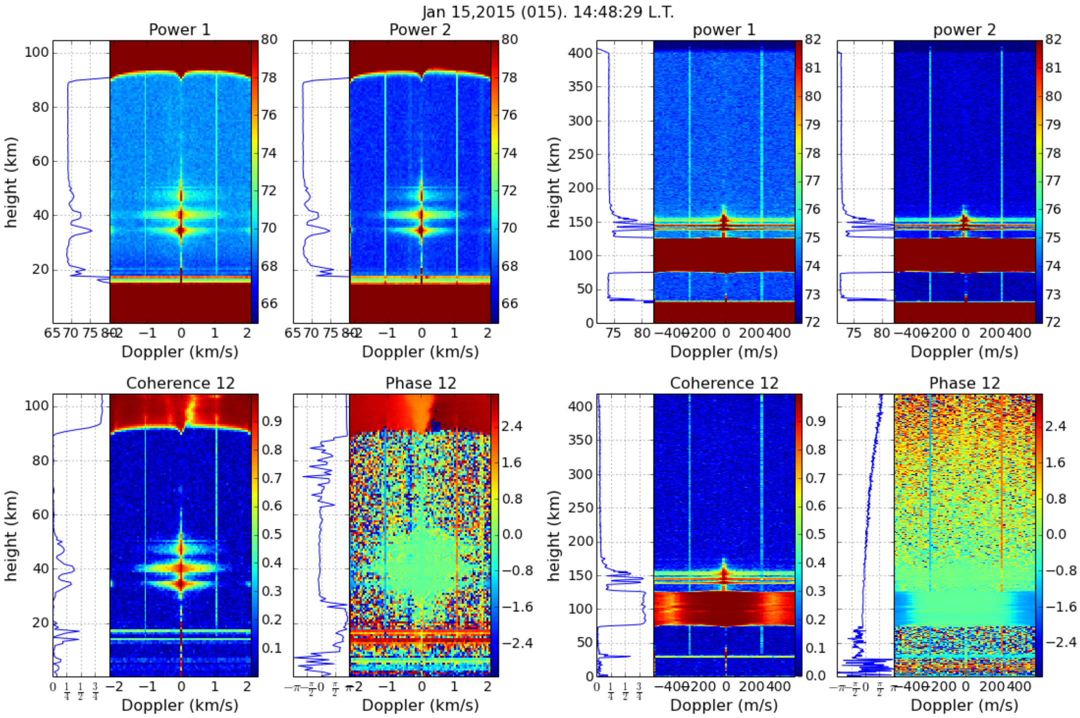

Figure 3.2 – Power spectra and cross-correlation coherence, and phase for cross-polarized antennas 1 and 2. The two columns on the left represent the wide-band mode and the two columns on the right, the Faraday mode. The upper row shows the corresponding power spectra, while the lower row shows the cross-correlation normalized magnitude and the phase.

3.1.1 Radar parameters and system configuration

The Valley ISR configuration uses both orthogonal linear polarizations of the whole 300 m × 300 m Jicamarca antenna to transmit a set of circular and orthogonal polarized waves. The reception is made with both polarizations of the four 150 m × 150 m quarters of the whole antenna. The two polarizations of each quarter are recorded using eight receiver channels. The two-way antenna beam pattern for each quarter is shown in Figure 3.3. There are two modes that are simultaneously used with a sequence of radar pulses that alternate between the two modes: (1) Faraday mode and (2) Wideband ISR mode. The radar parameters for both modes are summarized in Table 3.1. Both modes use the Faraday rotation method described in subsection 2.1.7 for determining the absolute electron density profile [*Farley*, 1969], but to avoid frequency aliasing, the wide-band mode uses a short inter-pulse period (IPP) of 105 km ($\sim 0.7\,\mathrm{ms}$) which allows for a Doppler velocity range of $\pm 2142\,\mathrm{m/s}$. This configuration causes range aliasing, i.e. the region $0-105\,\mathrm{km}$ will be mixed with backscattering from higher altitudes generated by previous pulses. As an example, the backscattering from the region $105-210\,\mathrm{km}$ will be received together with the backscattering region $0-105\,\mathrm{km}$ from the following pulse. Similarly, backscattering from the region $210-315\,\mathrm{km}$ will be received together with the $0-105\,\mathrm{km}$ backscattering region from two pulses ahead.

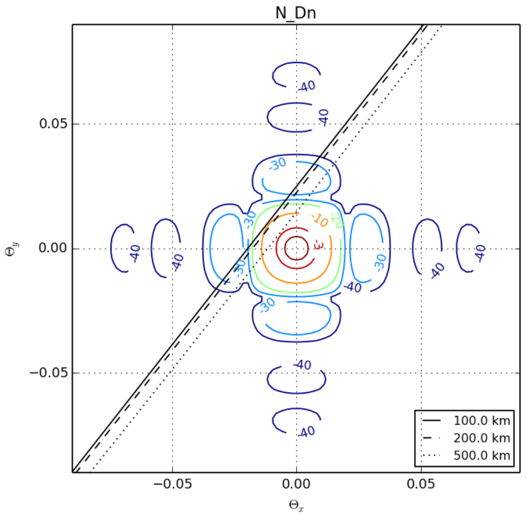

Figure 3.3 – On-axis normalized two-way antenna beam pattern for each quarter expressed in dB. The x- and y-axis correspond to the direction cosines. The black straight lines represent, at various heights, the directions where the magnetic aspect angle is zero (direction perpendicular to the earth's magnetic field **B**).

To avoid contamination of the backscattering from one pulse with the backscattering from neighboring pulses coming from higher ranged-aliased altitudes, right circular (RC) and left circular (LC) polarized pulses with flipped algebraic signs are used for successive transmissions as depicted in Figure 3.4. This figure is showing the sequence of four consecutive pulses with their corresponding RC and LC transmitted signs. Hypothetical highly reflecting mirrors have been placed at different altitudes to emphasize the range-aliasing problem. The desired range of wanted altitude returns is from 105 km to 210 km, which means that to de-flip the received signals, say right after the second pulse (TX2 in Figure 3.4), we need to use the codification used for TX1. When the signals in reception are de-flipped accordingly, DC and unwanted "cross-polarized" circular returns are thrown onto the Nyquist/2 frequency and Nyquist frequency respectively as can be observed in the power spectra plots in Figure 3.2.

Table 3.1 – Parameters for Faraday and Wideband ISR experiments at Jicamarca.

Parameter	Faraday	Wideband ISR
Effective IPP (km)	420 km	105 km
Nyquist (m/s)	535	2142
FFT points	64	80
Resolution (km)	0.75 km	0.75 km
Transmitter power (MW)	~ 2 MW	~ 2 MW
Rx Antenna	150 m × 150 m	150 m × 150 m
Code	28-baud	Barker-7

Figure 3.5 is similar to 3.1 but for the Wideband ISR mode. In this mode the 150-km echoes are range-aliased appearing around 45 km instead of 150 km.

Figure 3.6 shows the Faraday rotation angle from the same data presented in Figure 3.2. The Faraday rotation angle as a function of altitude has been applied a spline, shown in a thick black curve. With this smooth, monotonically increasing angle, we used equation (2.83) to estimate the electron density profile. To calculate Ω_e and θ, the International Geomagnetic Reference Field (IGRF) model [e.g., *Thébault et al.*, 2015] was used. In general we observe smooth Faraday rotation angle progression with altitude.

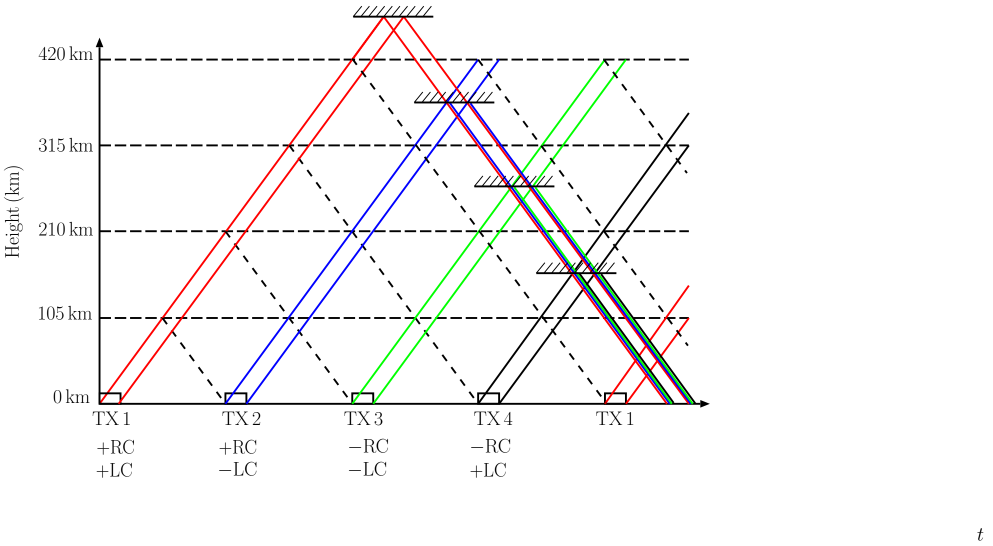

Figure 3.4 – Transmitted sequence of right and left circularly polarized pulses with flipped algebraic signs for the wide-band mode in the Valley experiment.

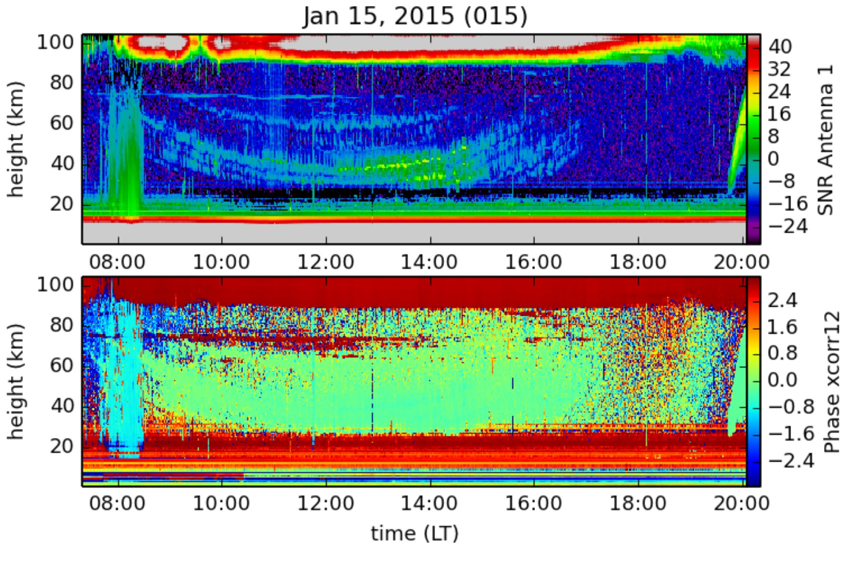

Figure 3.5 – SNR map and phase map of the cross-correlation between cross-polarized antennas 1 and 2. Similar to Figure 3.1 but for the Wideband ISR mode.

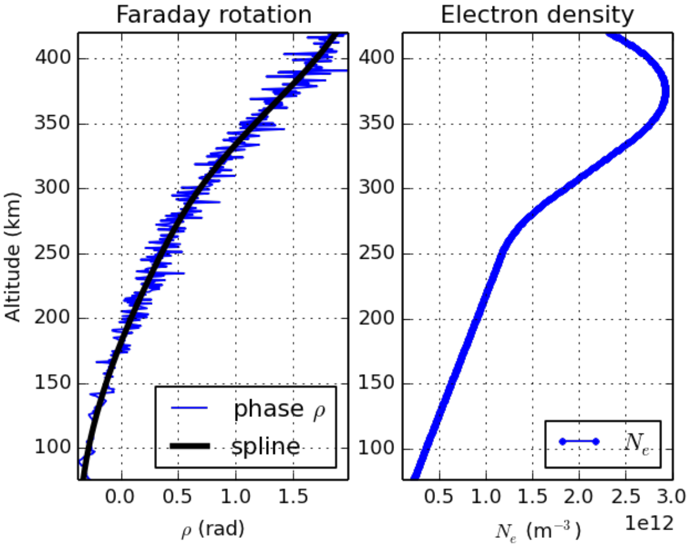

Figure 3.6 – Faraday rotation angle on the left, and electron density estimation based on the Faraday technique. This data corresponds to the spectra shown in Figure 3.2

3.1.2 Valley experiment and VIPIR ionosonde

Figure 3.7 shows the wide spectra mode of the Valley experiment, and a VIPIR ionogram on the right. When observing a sequence of these type of plots, there seems to be a correlation between the widening and the narrowing, the coming and going, and the changing in height of the 150-km echoes and the ionogram fluctuations. This requires further analysis and confirmation and should be part of the future directions of this study. From the Faraday rotation, given by the change of the cross-correlation phase shown in this figure and in Figure 3.2, we can estimate electron density profiles that change smoothly with height, i.e. without sharp density gradients. Figure 3.6 shows an attempt at inversion of the Faraday rotation angle as a function of height into an electron density profile. The electron density profile seems to change smoothly with altitude, i.e. there is no evidence of sharp density gradients in the valley ISR data.

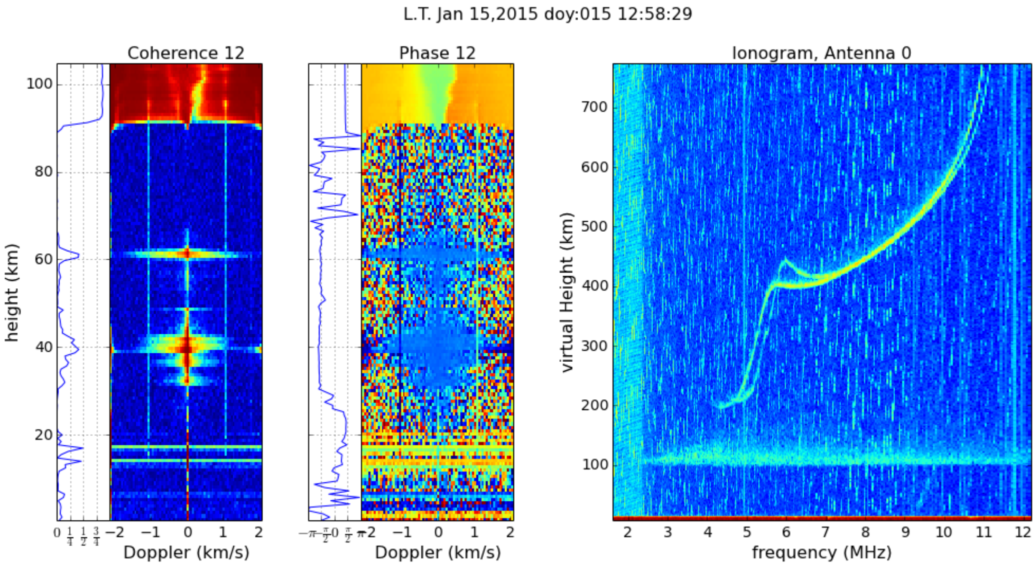

Figure 3.7 – Wide-band mode of the Valley experiment showing coherence and phase between the cross-polarized antennas 1 and 2. The ionogram on the right is the estimated power of antenna 1, showing combined O- and X-curves.

3.2 The MST-ISR-EEJ Experiment at JRO

Figure 3.8 displays a range-time-intensity (RTI) plot showing 3-m Bragg scatter radar power returns during a MST-ISR-EEJ campaign on April, 2015. The MST-ISR-EEJ is one of the available modes of operation at JRO that simultaneously monitor the equatorial D, E and F regions of the ionosphere [*Lehmacher et al.*, 2009]. The RTI in Figure 3.8 shows radar returns in the D-region at an altitude of 75 km, equatorial electro-jet around 100 km and the 150-km echoes in the region from 130 km to 180 km. The RTI also shows the "pass of the Galaxy"[1] as an enhanced background noise in all heights with a peak around 5 a.m. local time and the "back of the Galaxy"[2] around 5 p.m.

---

[1] The pass of the Galaxy is the period of time when the radar beam is pointing towards the center of the Milky Way, our Galaxy.

[2] The back of the Galaxy is the period of time when the radar beam is pointing towards the anti-center of the Milky Way, another direction of enhanced radio noise.

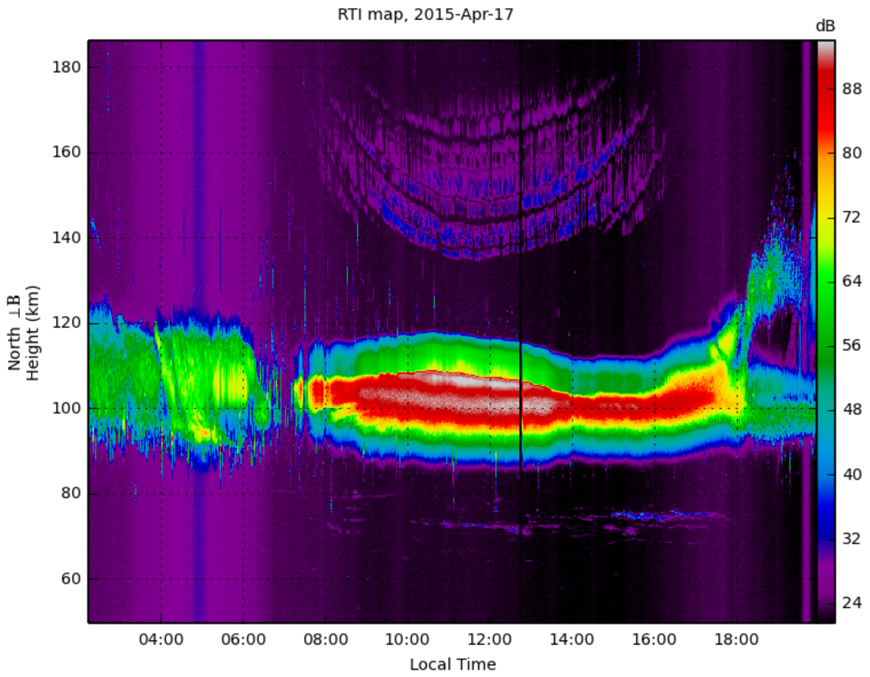

Figure 3.8 – Range-time-intensity (RTI) showing radar backscatter from the mesosphere, the electro-jet (EEJ) and the 150 – km echoes. This figure has been obtained using the MST-ISR-EEJ interactive website database developed by the Ionospheric Radar Group at the University of Illinois at Urbana-Champaign: `http://remote2.ece.illinois.edu/MST_ISR_EEJ_V3_scripts/show_parts_summary.py` .

The analysis that we are presenting in this study uses solely data from the MST mode which has a range resolution of 0.15 km and a typical inter-pulse-period (IPP) of 200 km (1.334 ms) with each pulse coded with a 64 bauds complementary code using 5% duty cycle of ~2 MW of transmitting power. Several campaigns have taken place with this mode starting in the year 2005 throughout 2017, and a campaign is scheduled for November 2017. A summary of the different radar parameters used on those campaigns can be found in Table 3.2.

Figure 3.9 shows the different antenna beam 2-way radiation pattern configurations used in all the MST-ISR-EEJ experiments since 2005 until 2016. The radiation pattern is obtained considering the phasing of all the 128 antenna modules of the main JRO antenna and the configuration of the antenna feeding mechanism in the switch yard [e.g. *Ochs*, 1965]. Configuration documents for every experiment are provided by the JRO staff and are included in Appendix B. In the antenna patterns, the horizontal solid and dashed black lines represent the loci of perpendicularity to the geomagnetic field **B** for 100, 300, and 600 km of altitude. The 2015 IGRF model [e.g., *Thébault et al.*, 2015] has been used to obtain the geomagnetic field vector **B** within the antenna beams. The contour line thickness in each of the 2-way radiation patterns is proportional to the antenna gain at the following levels: -1, -3, -6, -9, -12, -15, -18, and -21 dB from the maximum gain of the particular beam. $\Theta_{x'}$ and $\Theta_{y'}$ are the direction cosines[3] with respect to the plane of the antenna that has been rotated in such a way that the loci of perpendicularity to **B** are close to horizontal lines.

3.2.1 The ISR mode

The ISR mode of the MST-ISR-EEJ experiment uses a typical pulse length of 45 km coded using a barker3 code. Figure 3.10 shows an RTI of power taken with an antenna pointing perpendicular to Earth's magnetic field a few degrees of zenith to the east. The color range has been chosen from 22 dB (around the background noise level at 15:00 LT) to 70 dB in order to highlight the different levels of radar backscatter signal. Among the strongest signals are the equatorial electro-jet (EEJ) around 100 km of altitude and the equatorial spread F (ESF) that happened roughly from 1 to 7 LT, and from 19 LT to 7 LT the following day (see Figure 3.11).

---

[3] Direction cosines are $\sin\theta\cos\phi$ and $\sin\theta\sin\phi$ with θ and ϕ indicating the zenith and azimuth angles in a JRO-originated coordinate system with $\hat{z}$ pointing perpendicular to the antenna array plane.

Table 3.2 – Parameters for the MST part of the MST-ISR-EEJ experiments at Jicamarca. IPP: Inter-pulse-period, Rx: Receiver.

Parameter	2016	2014-2015	2009	2005-2007
IPP	375 km (2.5 ms)	202.5 km (1.35 ms)	187.5 km (1.25 ms)	200.1 km (1.334 ms)
Consecutive IPPs (Burst)	10	20	20	20
Bursts period	18750 km (125 ms)	20250 km (135 ms)	18750 km (125 ms)	6000 km (40 ms)
Complementary code	128 bauds	64 bauds	64 bauds	64 bauds
Height Resolution	0.15 km	0.15 km	0.15 km	0.15 km
Transmitter peak power (MW)	~ 2 MW	~ 2 MW	~ 2 MW	~ 2 MW
Rx Antennas	E, W, V, S	E, W, V, S	E, W, N, S	E, W, N, S

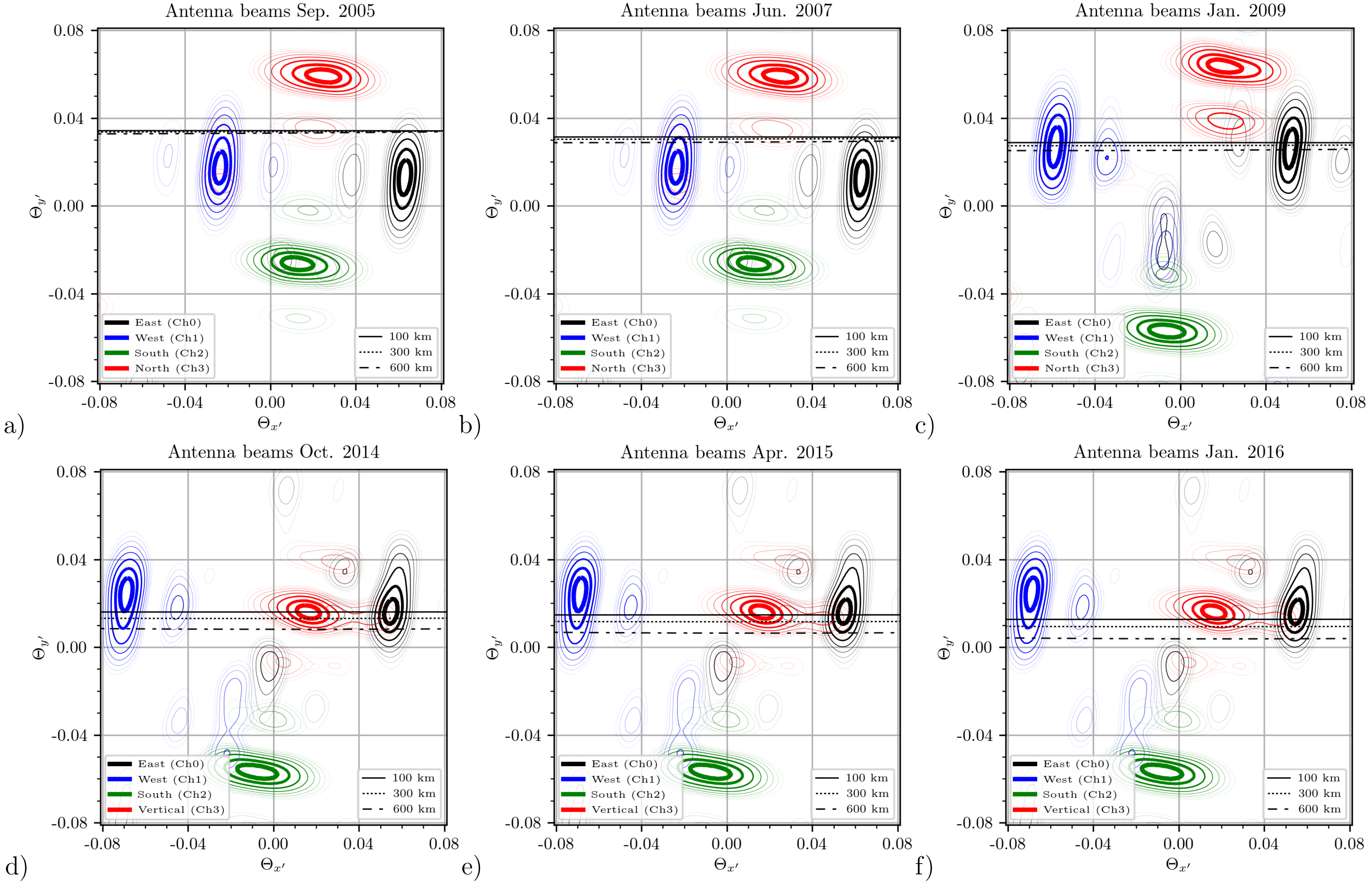

Figure 3.9 – Contour plots of the 2-way antenna beam patterns for the MST-ISR-EEJ campaigns from 2005 until 2016. Every figure shows superposed the contours of the 2-way radiation patterns of the 4 beams used in every campaign.

Figure 3.11 is plotted with a color range from 18 to 26 dB to distinguish the characteristics of the incoherent scattering of the F-region during daytime. In this last RTI, taken with an antenna with a beam pointing a few degrees off zenith and away from perpendicular to **B**, we can see the effect of Faraday rotation (explained in subsection 2.1.7): Notice that at local noon, the backscattering power has a local minimum around 270 km and local maximum around 200 km and also around 370 km. The reason for that behavior is that the transmission and reception of the signal is done with a linearly polarized antenna; hence, as the wave propagates through the ionosphere and its polarization experiences Faraday rotation we receive different stages of the rotation as a function of height. We can say that at around 270 km the wave would have been rotated 90 degrees; therefore, we detected less power from that altitude.

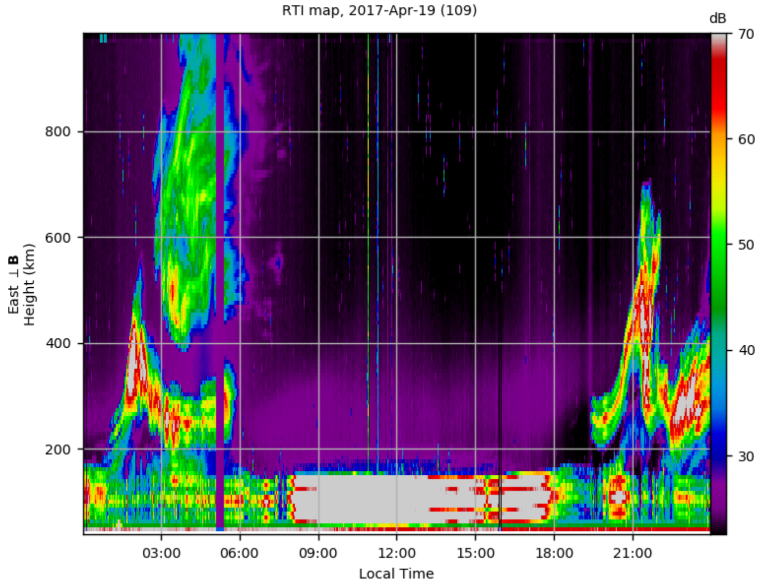

Figure 3.10 – RTI plot of the ISR mode showing a typical equatorial ionosphere for April 19, 2017. Strong backscatter echoes come from equatorial electro-jet (EEJ) and from equatorial spread F (ESF). This plot has been obtained using the MST-ISR-EEJ interactive website database: `http://remote2.ece.illinois.edu/MST_ISR_EEJ_V3_scripts/show_parts_summary.py` .

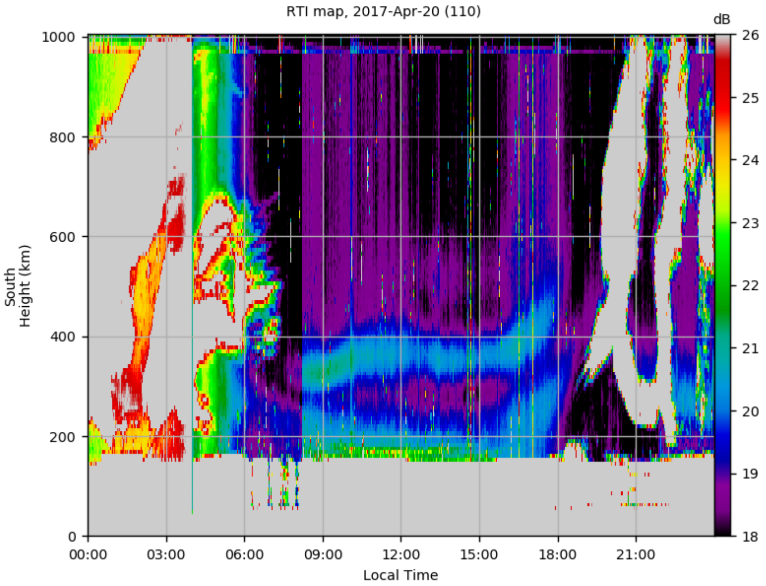

Figure 3.11 – RTI plot of the ISR mode showing a typical equatorial ionosphere for April 20, 2017. Plot obtained using the MST-ISR-EEJ interactive website database: `http://remote2.ece.illinois.edu/MST_ISR_EEJ_V3_scripts/show_parts_summary.py` .

3.2.2 Estimation of vertical plasma drift from the 150-km echoes

The technique of obtaining Doppler velocity estimates from radar backscattering power spectra at 150-km region altitudes over JRO was described by *Kudeki and Fawcett* [1993]. This technique has been used since as a means of monitoring ionospheric zonal electric fields at equatorial latitudes. Here we will apply this technique for data obtained in MST mode from the MST-ISR-EEJ campaigns. In order to obtain power spectra estimations, periodograms of 64 points were incoherently integrated. The periodograms were obtained with FFTs of decoded and coherently integrated data. The number of coherent integrations was either 10 or 20 according to the number of consecutive IPPs (see Table 3.2). To achieve 1 minute integrated spectra, the number of incoherent integrations varies according to the campaign; e.g., for the campaigns of 2005, 2006, and 2007 the number of incoherent integrations needed was 23, while all the other campaigns starting in 2009 needed 7 incoherent integrations.

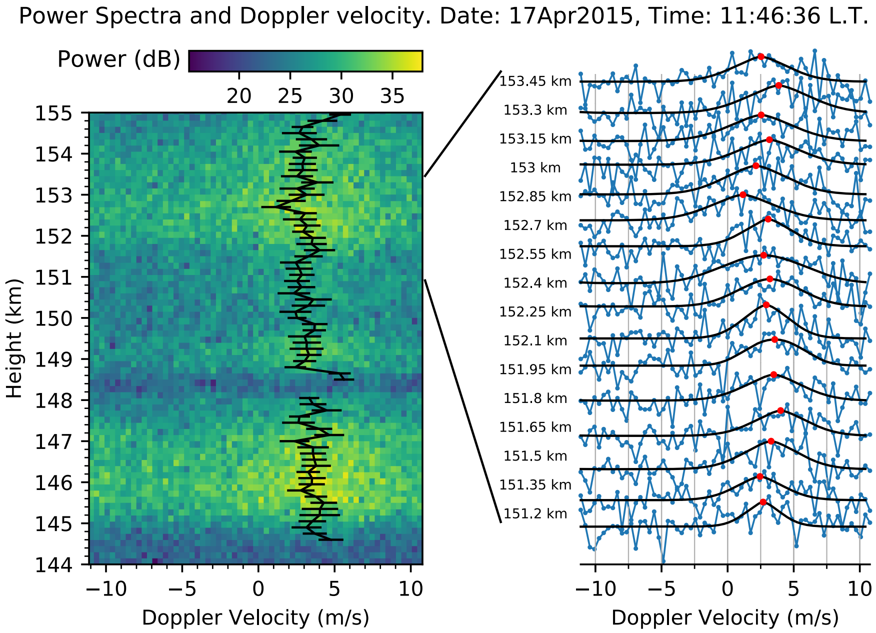

Figure 3.12 – Power spectra and the Doppler velocity estimations and error bars for a minute-worth integrated data. This data was taken during an MST-ISR-EEJ campaign on April 17, 2015, around 11:46:36 local time with the vertical beam. The column on the left shows the spectra in dB as a color map with the Doppler velocity estimations as black lines with error bars. The right panel shows the individual power spectra in blue, the fitted model in black and a red dot at the estimated Doppler shift for consecutive altitudes ranging from 151.2 km to 153.45 km.

Figure 3.12 shows an example of the estimated power spectra as a color map on the left panel with the estimated Doppler velocity shift resulting from fitting the spectra to the generalized Gaussian model:

$$\langle S(\omega)\rangle = N + A\, e^{-0.5\left|\frac{\omega - V}{\sigma}\right|^{p}}, \tag{3.1}$$

where N is the estimated noise level, A is the amplitude, V is the Doppler shift, σ is the spectral width (if $p = 2$) while p is a power parameter. To account for relatively wide spectra with power crossing the Nyquist frequency, equation (3.1) was modified by adding the two neighboring frequency aliased copies becoming

$$\langle S(\omega)\rangle = N + A\,e^{-0.5\left|\frac{\omega-V}{\sigma}\right|^{p}} + A\,e^{-0.5\left|\frac{\omega-\Omega_{Nyq}-V}{\sigma}\right|^{p}} + A\,e^{-0.5\left|\frac{\omega+\Omega_{Nyq}-V}{\sigma}\right|^{p}}, \qquad (3.2)$$

where Ω_{Nyq} is the sampling rate. Equation (3.2) will also work for narrow spectra with no aliasing because the contributions from the two side copies will be minimal once the optimizer finds the best fitting parameters. Therefore, we used equation (3.2) instead of equation (3.1) as the model used for fitting all the spectra. To fit the measured spectrum to this model, the following logarithmic misfit definition was used

$$\chi^2 = \frac{K}{n-5}\sum_{q=0}^{n-1}\left(\ln S(q\delta\omega) - \ln\langle S(q\delta\omega)\rangle\right)^2, \qquad (3.3)$$

where K is the number of independent periodograms, n is the number of FFT points, $n-5$ is the number of degrees of freedom, and $\delta\omega$ is the frequency resolution. The logarithmic fit was used because it has been found that logarithmic fits work better for narrow spectra [e.g. *Sheth et al.*, 2006]. The scipy.optimize routine fmin_l_bfgs_b was used to do the fitting. As the initial guess; the noise estimate, N_0, was obtained using *Hildebrand and Sekhon* [1974], $p_0 = 2$ assuming a Gaussian spectrum, V_0 and σ_0 was obtained using moment estimators [e.g. *Woodman*, 1985], and $A_0 = S(V_0)$, i.e. the measured power at the doppler shift. The fmin_l_bfgs_b routine accepts an entry of the permitted bounds for the parameters; we used (0, n-1) for V, (0.5,n-1) for σ, ($0.5A_0$, $1.5A_0$) for A, (1.5, 2) for p, and ($0.9N_0$, $1.1N_0$) for N. These bounds were used for the 2015 campaign, and they should also work for 2009, 2014, 2016, and 2017 campaigns that have a bandwidth of roughly ±11.1 m/s, but they should be adjusted for the 2005, 2006, and 2007 campaigns where the bandwidth was roughly ±36 m/s.

Correcting for frequency aliasing

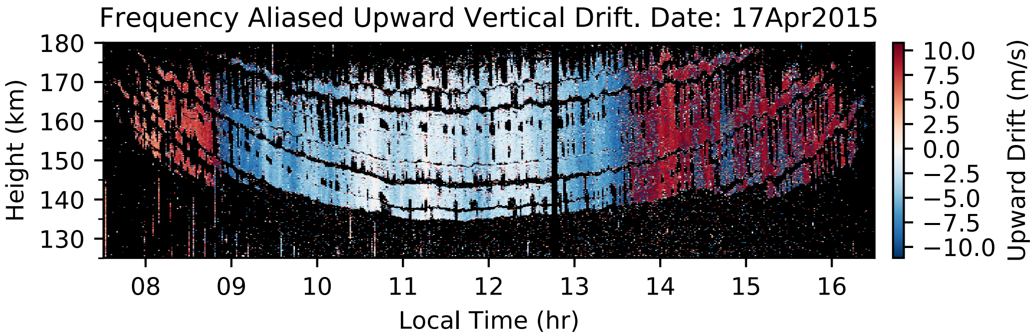

Figure 3.13 – RTI of frequency aliased upward plasma drift.

Figure 3.13 shows an RTI of upward plasma drift from inversion of estimated power spectra with values inside our limited bandwidth of roughly ±11.1 m/s. This figure clearly shows frequency aliasing problems around 9 and 13.5 LT because, unless drastic events happen e.g. solar flares, drifts do not change suddenly ±22.2 m/s. Figure 3.12 shows that we are able to detect Doppler velocities in the range of roughly ±11.1 m/s, but vertical plasma drifts usually surpass that range. Figure 3.13 shows an RTI of upward plasma drift without any corrections. Notice that around 9 and 13.5 local time, there is a wraparound of the drift. Normal vertical plasma drift during day time moves upward, hence the plasma drift from 9 to 13.5 L.T. should be corrected by adding Ω_{Nyq} that in this case is 22.227 m/s. We notice also that the drifts showing blue color between 13 and 16 L.T should also be shifted up by Ω_{Nyq}. The corrected upward $\mathbf{E} \times \mathbf{B}$ plasma drift from the 150-km region is depicted in Figure 3.14 together with a height averaged upward drift.

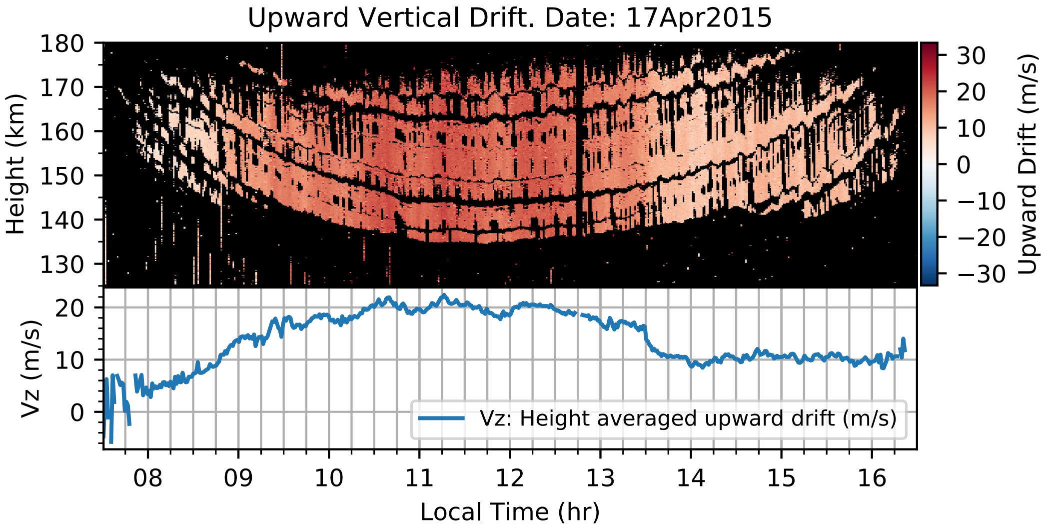

Figure 3.14 – RTI of upward $\mathbf{E} \times \mathbf{B}$ plasma drift from the 150-km region created based on the data used in Figure 3.13 but corrected for frequency aliasing. In the bottom panel a height averaged upward drift is shown.

Spectral width versus SNR

Chau and Kudeki [2013] identified two different populations of 150-km echoes based on their spectral width versus SNR dependence. They built a histogram of 150-km echoes as a function of SNR and spectral width including data from 9 days during the January 2009 campaign. The histogram was annotated with two ellipses separating NEIS and FAI echoes, with the spectral width of the NEIS echoes being linearly dependent on SNR, and those of the FAI echoes being independent of SNR. Figure 3.15 shows RTIs of SNR and spectral width that we are going to use to create the aforementioned histogram. Figure 3.16 shows the two-dimensional histogram of spectral width versus SNR with spectra from data collected with the vertical beam on April 17, 2005. The two ellipses are the same as those used in Figure 3 in *Chau and Kudeki* [2013]. We notice that while the ellipses separate the NEIS and FAI echoes for the January 2009 campaign, they do not match the population of spectra found on April 17, 2015. Figure 3.17 shows the spectra histograms for January 17, 2009 (left panel) and January 30, 2016 (right panel). These two January days have a population of large SNR and SNR-independent spectral width like the one shown in *Chau and Kudeki* [2013]. On all the histograms we have kept the same ellipses for comparison reasons. We notice that different campaigns/seasons have different distributions of spectral width versus SNR.

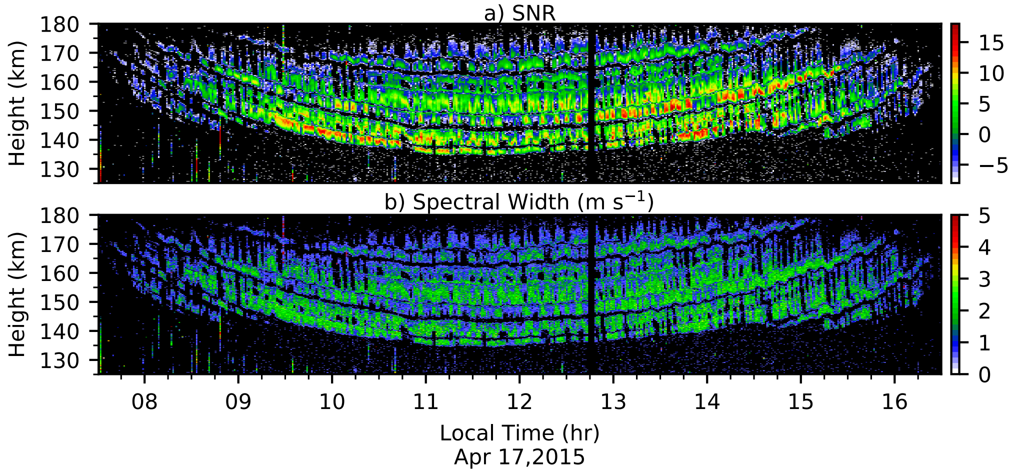

Figure 3.15 – a) RTIs of signal-to-noise ratio (SNR), and b) Spectral width for the vertical beam on April 17, 2015.

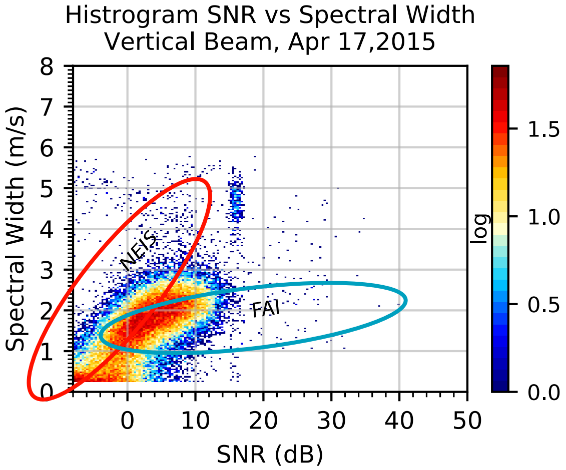

Figure 3.16 – Two-dimensional histogram similar to Figure 3 in *Chau and Kudeki* [2013]. The two ellipses have been placed at the same positions as those in Figure 3 of *Chau and Kudeki* [2013].

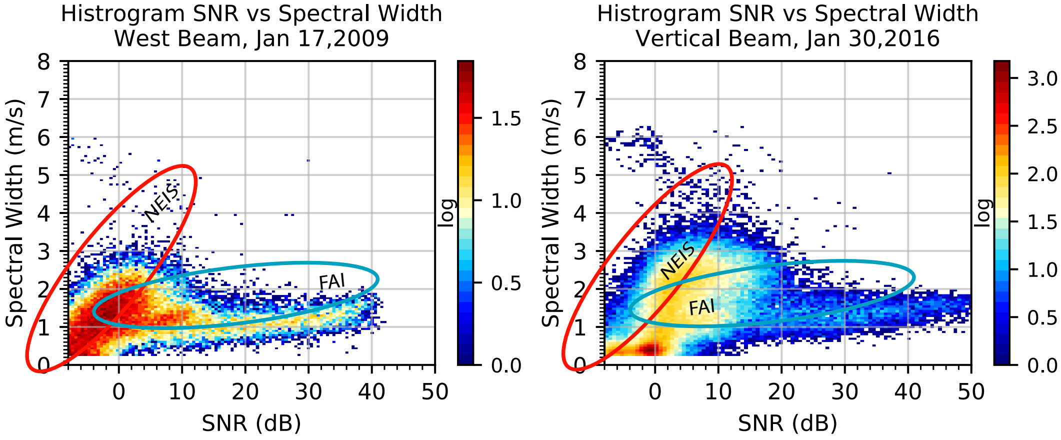

Figure 3.17 – Plots similar to Figure 3.16 for January 2009, and January 2016 data with the same ellipses used in Figure 3 of *Chau and Kudeki* [2013].

3.3 Ionograms using the Vertical Incidence Pulsed Ionospheric Radar (VIPIR) at Jicamarca

The JRO VIPIR ionosonde consists of a wide-band log-periodic antenna (see left part of Figure 3.18 and Figure 3.19) that sends vertically propagating radio wave pulses by means of a 4 kW peak power transmitter sweeping its frequency from 0.3 to 20 MHz. The transmitted pulses are 70 μs (10.5 km) long, tapered with a raised cosine pulse. The sequence of frequencies transmitted can be seen in the right part of Figure 3.20 where transmitted frequencies sweep in a lapse of 10 seconds from 1.6 MHz up to 12.5 MHz. On the left part of Figure 3.20 we see a zoomed in version of the transmitted frequencies where fast sweeps of 4 consecutive frequencies, e.g. 1600, 1606.25, 1612.5, 1618.75, and 1625 kHz, are sent with an inter-pulse-period (IPP) of 6.25 ms. That sequence is repeated 4 times, where a single frequency, e.g. 1600 kHz, is transmitted 4 times with an IPP of 25 ms. The reason for this particular sequence of pulses is to avoid range aliasing by using contiguous transmitted pulses at different frequencies, while still repeating the sequence 4 times to have a better estimate of the reflected power. The detection of the reflected pulses is done by 8 short dipoles (see right part of Figure 3.18) connected to 8 coherent receivers. The receiving antennas form two sets of orthogonal interferometric baselines, in the North-West and North-East directions, which will be used to detect the angle of arrival of the reflected radio waves. The antennas in the North-West baselines are polarized in the North-West direction, while the antennas in the North-East baselines are polarized in the North-East direction. Hence, all the antennas will be detecting both the ordinary (O) and the extraordinary (X) modes of propagation.

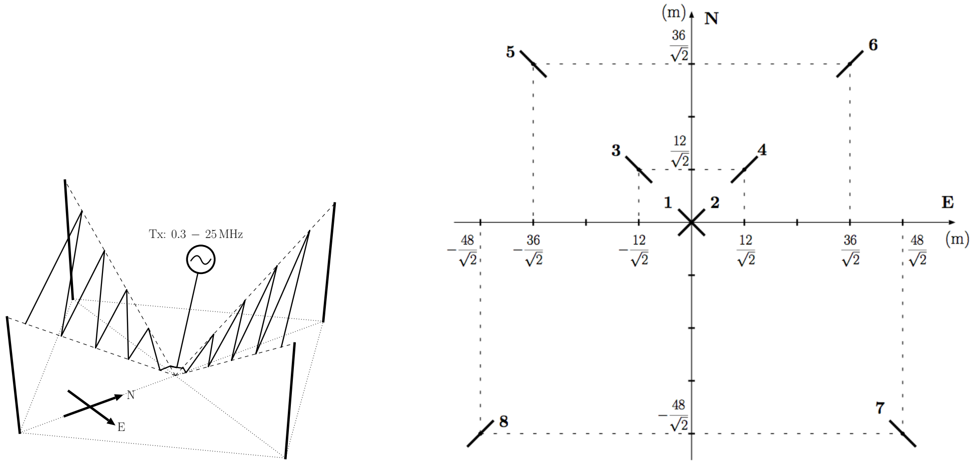

Figure 3.18 – The sketch on the left represents the VIPIR transmitting wide-band antenna. Notice that this antenna configuration will produce a linearly polarized electric field in the North-West direction, exciting both ordinary (O) and extraordinary (X) modes of propagation. The diagram on the right shows the location of the receiving antennas which form two sets of orthogonal baselines. These antennas are oriented to be sensitive to both the ordinary (O) and the extraordinary (X) modes of propagation.

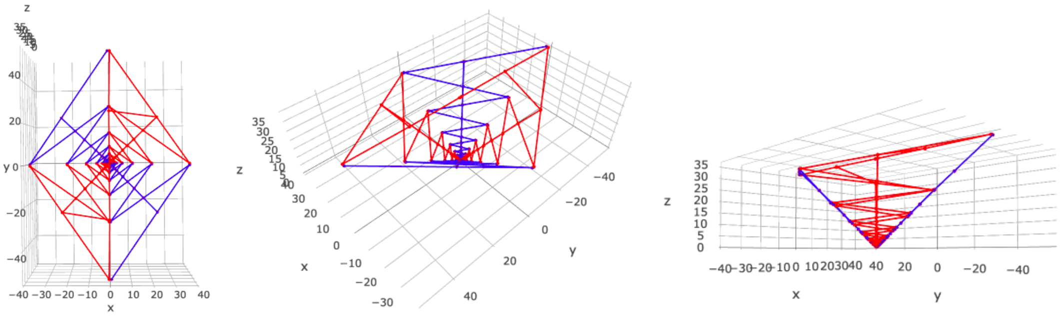

Figure 3.19 – Different views of the wide-band log-periodic antenna. The red wires are the transmitting elements, while the blue wires are there to maintain the structure of the antenna. The x axis points to the East, the y axis to the north, and the z axis points upward. This antenna configuration will generate a wave polarized in the North-West direction, hence exiting both O- and X-modes of propagation.

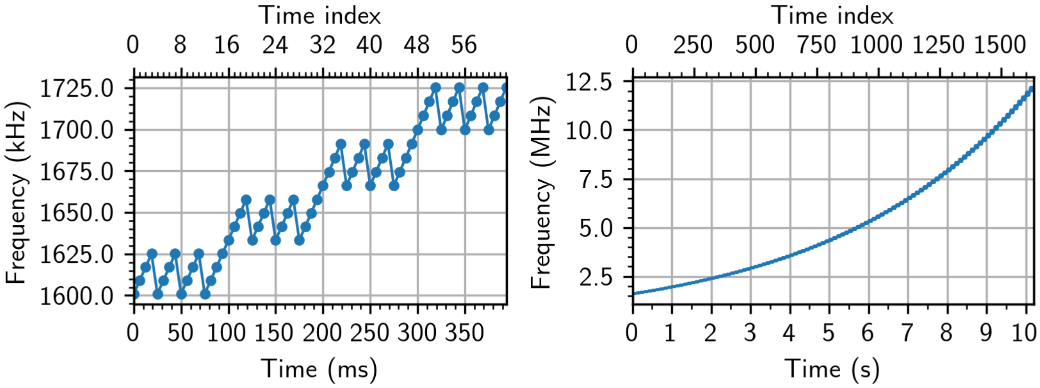

Figure 3.20 – Sequence of pulse frequencies transmitted by the VIPIR ionosonde on the January 2016 campaign. The plot on the left shows a zoomed in part at the beginning of the transmitting sequence. The plot on the right shows the complete sequence of frequencies used in this experiment where transmitted frequencies sweep in a lapse of 10 seconds from 1.6 MHz up to 12.5 MHz.

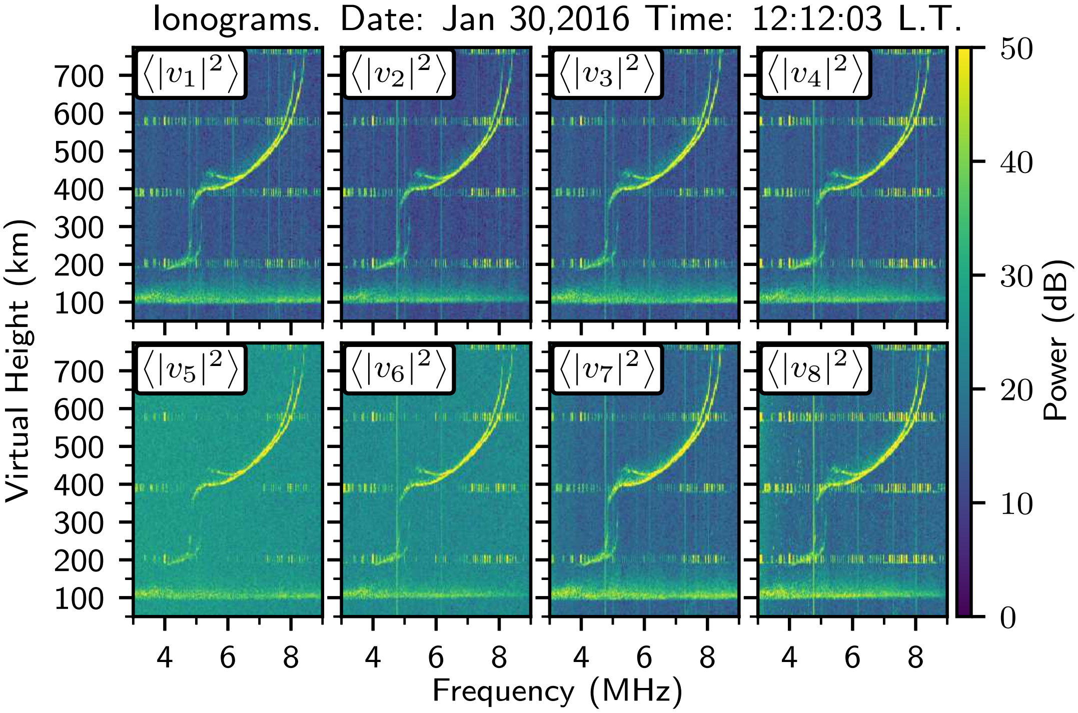

Figure 3.21 – VIPIR ionograms showing power of the 8 receivers in dB.

Figure 3.21 shows the power of the eight receivers as ionograms. Each of the received signals contains the reflected power of both ordinary (O) and extraordinary (X) modes of propagation, since both modes were excited in transmission and the receiving antennas are configured to detect both modes of propagation. This ionogram was obtained with data taken on January 30, 2016, at 12:12:03 local time. We can see that the f_OF2 critical frequency or penetration frequency (see subsection 2.1.5 for a review of the critical frequencies) is close to 8 MHz. Using the formula in equation (2.13), 8 MHz corresponds approximately to a $7.94 \times 10^{11}\,\mathrm{m}^{-3}$peak electron concentration N_m. The ionograms also show interference at intervals of 200 km which correspond to the JRO radar operation in the MST-ISR-EEJ mode.

For the separation of the O and X modes we are going to use the cross-polarized antennas 1 and 2 (see right panel in Figure 3.18 for the position and orientation of the antennas). To obtain the O-mode, we add the voltages of antennas 1 and 2, i.e.

$$v_O = v_1 + g\, v_2, \tag{3.4}$$

where v_1 and v_2 are the voltages of antenna 1 and antenna 2 respectively, and g is a complex value that serves as calibration parameter. This calibration parameter will account for any systematic phase and/or gain differences between the receivers and also for the magnetic declination angle which varies with altitude, but for a first approximation we can consider g being constant. Similarly for the X-mode we have

$$v_X = v_1 - g\, v_2. \tag{3.5}$$

In a single ionogram run, each frequency is transmitted 4 times in a lapse of 100 ms. The coherently detected complex voltages obtained for antenna a are v_{a0}, v_{a1}, v_{a2}, and v_{a3}. To estimate the power $\langle |v_a|^2 \rangle$ of a single antenna we average the 4 available values $|v_{ai}|^2$ as

$$\left\{ |v_a|^2 \right\} = \frac{1}{4} \sum_{i=0}^{3} |v_{ai}|^2, \tag{3.6}$$

where $\{|v_a|^2\}$ stands for an estimator of $\langle |v_a|^2 \rangle$. Similarly, our cross-correlation estimator from antennas a and b is

$$\{v_a^* v_b\} = \frac{1}{4} \sum_{i=0}^{3} v_{ai}^* v_{bi}. \tag{3.7}$$

To estimate the O-mode power, $\langle |v_O|^2 \rangle = \langle v_O^* v_O \rangle$, based on already calculated power and cross-correlation of antennas 1 and 2, we start conjugating (3.4) and multiplying by (3.4)

$$\left\langle |v_O|^2 \right\rangle = \left\langle (v_1^* + g^* v_2^*)\,(v_1 + g v_2) \right\rangle, \tag{3.8}$$

which yields

$$\left\langle |v_O|^2 \right\rangle = \left\langle |v_1|^2 \right\rangle + |g|^2 \left\langle |v_2|^2 \right\rangle + 2\,\mathbf{Re}\left\{ g \left\langle v_1^* v_2 \right\rangle \right\}, \tag{3.9}$$

which can be estimated using (3.6) and (3.7).

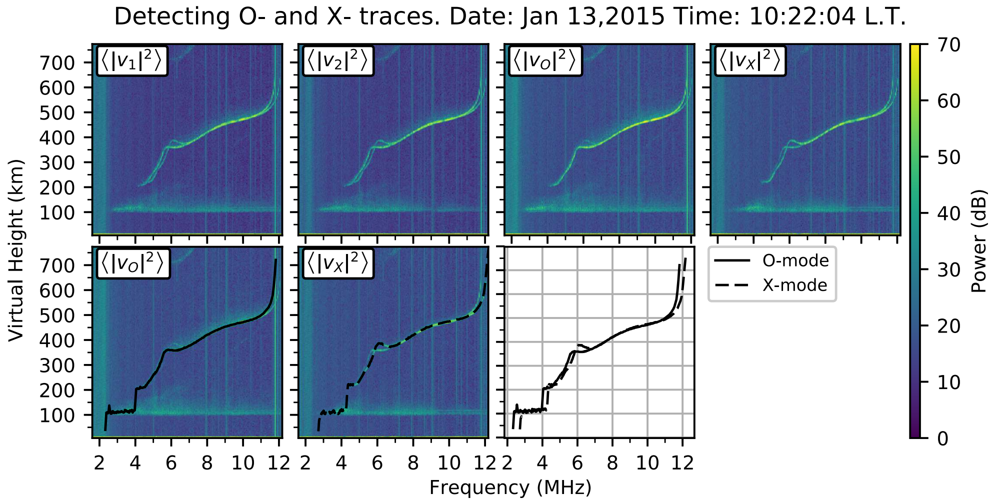

Figure 3.22 – The ionograms in column 1 and 2 in the first row show the estimated power returns for antennas 1 and 2, i.e. $\langle|v_1|^2\rangle$, and $\langle|v_2|^2\rangle$. The plots in columns 3 and 4 of the first row show the estimated power of O- and X-modes, $\langle|v_O|^2\rangle$ and $\langle|v_X|^2\rangle$. In the second row, $\langle|v_O|^2\rangle$ and $\langle|v_X|^2\rangle$ are plotted together with the estimated virtual height curves. The plot in column 3 , second row, shows the O- and X- traces of the ionogram.

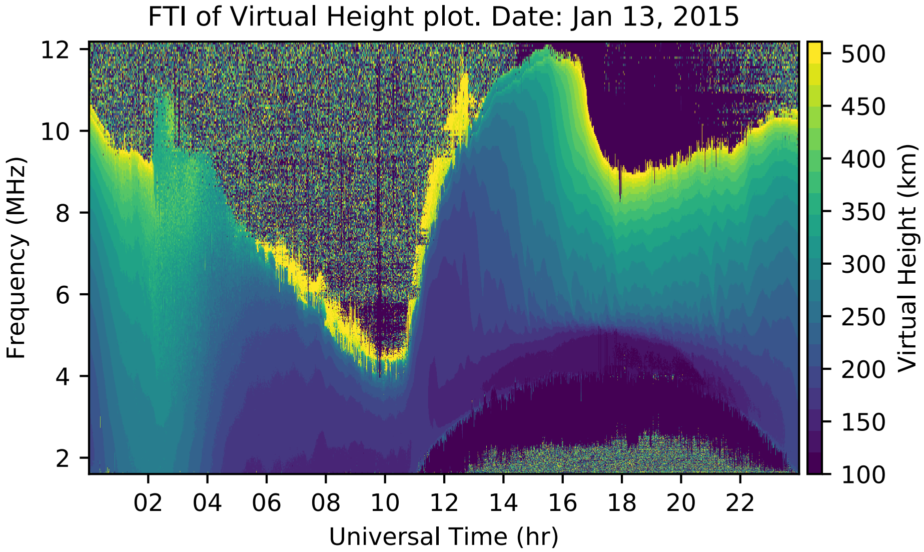

Figure 3.23 – Frequency-time-intensity (FTI) plot of ionosonde virtual reflecting height with data taken at JRO by the ionosonde VIPIR on January 13, 2015.

Similarly for the X-mode we obtain

$$\left\langle |v_X|^2 \right\rangle = \left\langle |v_1|^2 \right\rangle + |g|^2 \left\langle |v_2|^2 \right\rangle - 2\, \mathbf{Re} \left\{ g \left\langle v_1^* v_2 \right\rangle \right\}. \tag{3.10}$$

The process of separating the O and X modes and the detection of the traces is depicted in Figure 3.22. In the first row of Figure 3.22 we see the estimated versions of powers $\langle |v_1|^2 \rangle$, $\langle |v_2|^2 \rangle$, $\langle |v_O|^2 \rangle$, and $\langle |v_X|^2 \rangle$. In the second row of Figure 3.22 we see the detected O and X traces superposed to the ionograms of $\langle |v_O|^2 \rangle$, and $\langle |v_X|^2 \rangle$. The detection of the ionogram traces has been done with an algorithm described in Appendix A. Finally, the third column of the second row of Figure 3.22 shows both the O- and X-traces with continuous and dashed lines respectively. Using the O-traces just described, one can form a map of the whole day as frequency-time-intensity (FTI) maps with intensity being the virtual height. An example of an FTI plot is shown in Figure 3.23. This figure shows the sounding frequency of the ionosonde on the vertical axis and the time in universal time (UT) on the horizontal axis while the color corresponds to the virtual reflected height. For this graph we have chosen to use UT time because at Jicamarca (-5 hours from UT) the sunrise was around 11 UT which nicely separates the nighttime from the daytime ionospheres on left side and right side of the FTI plot. The color scale step has been reduced from the default 256 scales to 20 in order to emphasize and see the fluctuations of the constant virtual height contours.

3.3.1 Angle of arrival (AOA)

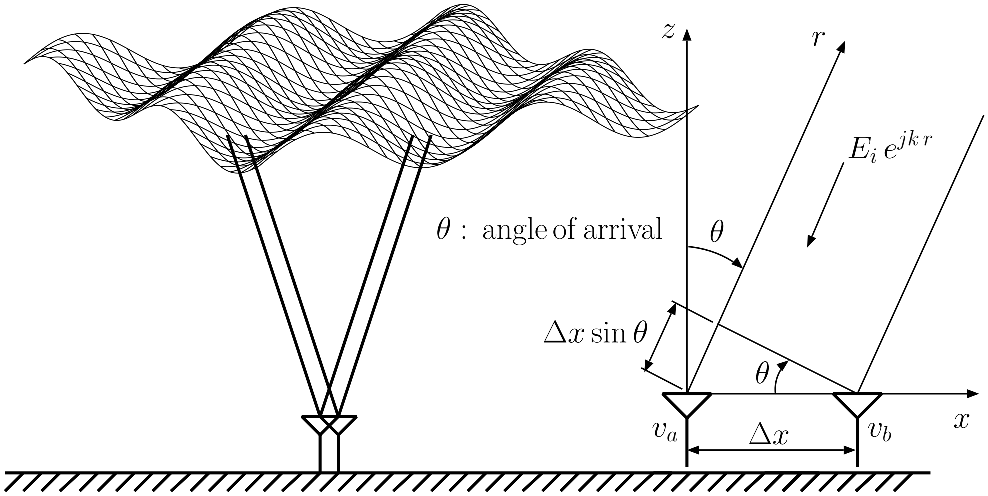

Figure 3.24 – Cartoon of electron density contour at a certain frequency being rippled by some wave. The two antennas indicate an interferometer, which is used to calculate the angle of arrival of the reflected TEM pulses.

The VIPIR receiving system consists of eight antennas distributed as depicted in the right panel of Figure 3.18. We used the largest baselines (84 m), i.e. between antennas 5 and 7 for the North-West direction and antennas 6 and 8 for the North-East direction. To explain our procedure to obtain the angle of arrival (AOA) we are going to use the cartoon depicted in Figure 3.24.

Let us define

$$v_a = E_i e^{jkr} \tag{3.11}$$

as the voltage received by antenna a. From the picture we recognize that the same signal arrives earlier to antenna b by a phase of $2\pi\Delta x\sin\theta/\lambda$, hence the signal received by antenna b is

$$v_b = v_a e^{-jk\Delta x\,\sin\theta}, \tag{3.12}$$

where Δx is the separation between the antennas, θ is the AOA, and $k = \frac{2\pi}{\lambda}$ is the wave number of the received TEM signal with wavelength $\lambda = \frac{c}{f}$, where c is the speed of light, and f is the signal frequency. We can get the phase difference of the two signals by calculating the angle of the cross-correlation of v_a and v_b

$$\angle v_a^* v_b = \angle\left(|E_i|^2\, e^{-jk\Delta x\,\sin\theta}\right) = -k\Delta x\,\sin\theta. \tag{3.13}$$

Hence, we can get the AOA from the cross correlation of the signals received at a and b as follows:

$$\theta = \sin^{-1}\left(-\frac{\angle v_a^* v_b}{k\Delta x}\right) = \sin^{-1}\left(-\frac{\lambda}{2\pi\Delta x}\angle v_a^* v_b\right). \tag{3.14}$$

Next we want to produce a map similar to Figure 3.23 but with AOA information. We start by estimating the cross-correlation ionograms using equation (3.7) between the pair of antennas of the largest baselines. Subsequently, from each cross-correlation ionogram we read off the transmission frequency, virtual height, and equation (3.14) based AOA data triplets along the O-trace coordinates previously established for the same ionogram estimation time. Data triplets collected for a whole day of observations allow the construction of FTI plots of AOA like the ones shown in the center and bottom panels of Figure 3.25. This map was obtained using the cross correlation phase from antennas 5 and 7, the largest baseline (84 m) for the North-West direction, and antennas 6 and 8 from the North-East baseline.

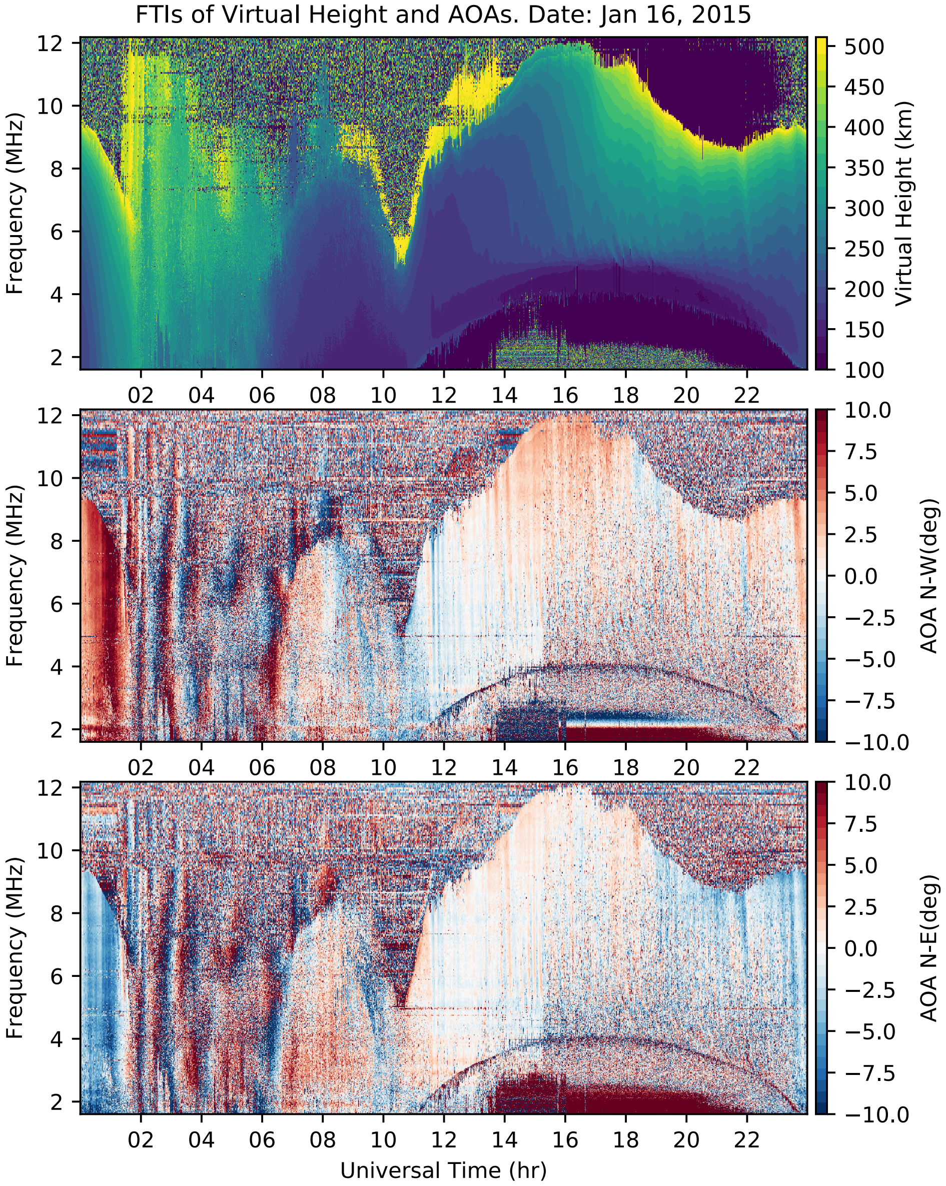

Figure 3.25 – Frequency-time-intensity (FTI) plots. Top panel: ionosonde virtual reflecting height. Center panel: angle of arrival of the reflected O-mode signal of the North-West interferometer. Bottom panel: same as center panel but for the North-East interferometer. The data was taken at JRO by the ionosonde VIPIR on January 16, 2015.

Figure 3.25 shows FTI plots of virtual height in kilometers, and angle of arrival for the O-mode data in degrees from the north-west, and north-east interferometers for VIPIR data taken on January 16, 2015. The plot in the top plate shows virtual heights in a similar way as in Figure 3.23. The plots in the center and bottom panels show the angle of arrival of the reflected waves. Interferometry analysis at the reflecting height indicates that for a quiet ionosphere most of the reflected pulses are coming from one single reflecting point in the range of ±5°, but for disturbed ionospheres, like from 00:00 to 6:00 UT in Figure 3.25, the AOAs can be larger than ±5° and the virtual reflected heights appear diffuse and not to come from a single point. The phenomenon causing this equatorial irregularity is called equatorial spread F (ESF) . This is depicted in Figure 3.26, where ionograms in the first row of plots were taken during the disturbed hours of the local night. These ionograms do not show a clear reflecting height, in contrast to the defined reflecting heights from the O- and X-traces that we can see in the second row of plots in Figure 3.26.

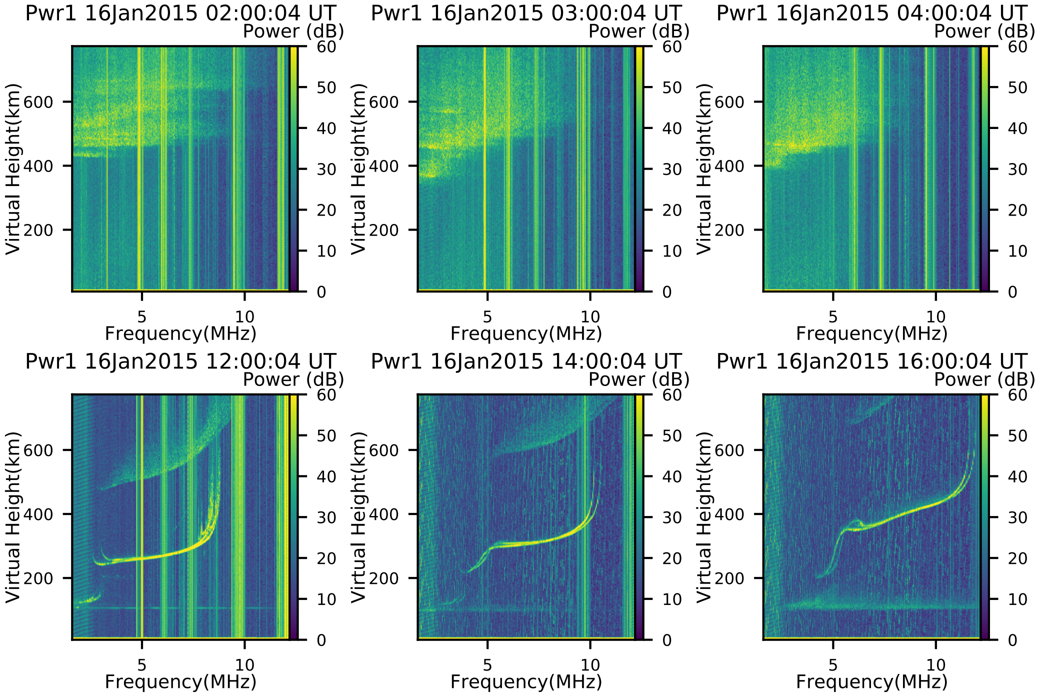

Figure 3.26 – Ionograms at different times for day January 16, 2015. The first row of plots show ionograms from a disturbed ionosphere at different local nighttimes, while the ionograms in the second row of plots belong to a quiescent ionosphere in the local daytime.

The diffuse F-region ionograms in Figure 3.26 have been observed ever since ionosondes were installed in equatorial regions (*Booker and Wells* [1938] reported them with observations done between years 1937 and 1938). Examples of ESF detected by the 50 MHz JRO radar operating in the MST-ISR-EEJ mode are shown in Figures 3.10 and 3.11. The RTI in Figure 3.1 corresponding to January 15, 2015, shows the start of an ESF around 22:00 local time; there is no radar data after that time, but from the ionograms shown in Figure 3.26 and the FTIs in Figure 3.25 we can observe that the ESF phenomenon continued during the night.

3.3.2 Direction of propagation of waves detected with VIPIR

In Figure 3.25 we notice that the oscillations of VIPIR virtual heights and angle of arrival (AOA) display downward phase progressions. It is well known, for internal gravity waves (IGW) (also known as buoyancy waves), to show downward phase propagation while at the same time energy propagates upwards as described in section 2.2. In that sense, through the day, we detect the activity of IGW with energy moving upwards. In this section we explain how to obtain information about the direction of propagation of IGW based on AOA information. AOA oscillations from the two orthogonal baselines should give us the plane of maximum oscillation of the gravity waves crossing the antenna field of view, i.e. the plane formed by $\hat{z}$ and $\mathbf{k}$ in Figure 2.8. For example, in Figure 3.27 we indicate with black and blue rectangles regions in time and frequency that we are going to pay closer attention to. The frequency-averaged AOAs from those regions are displayed in Figure 3.28.

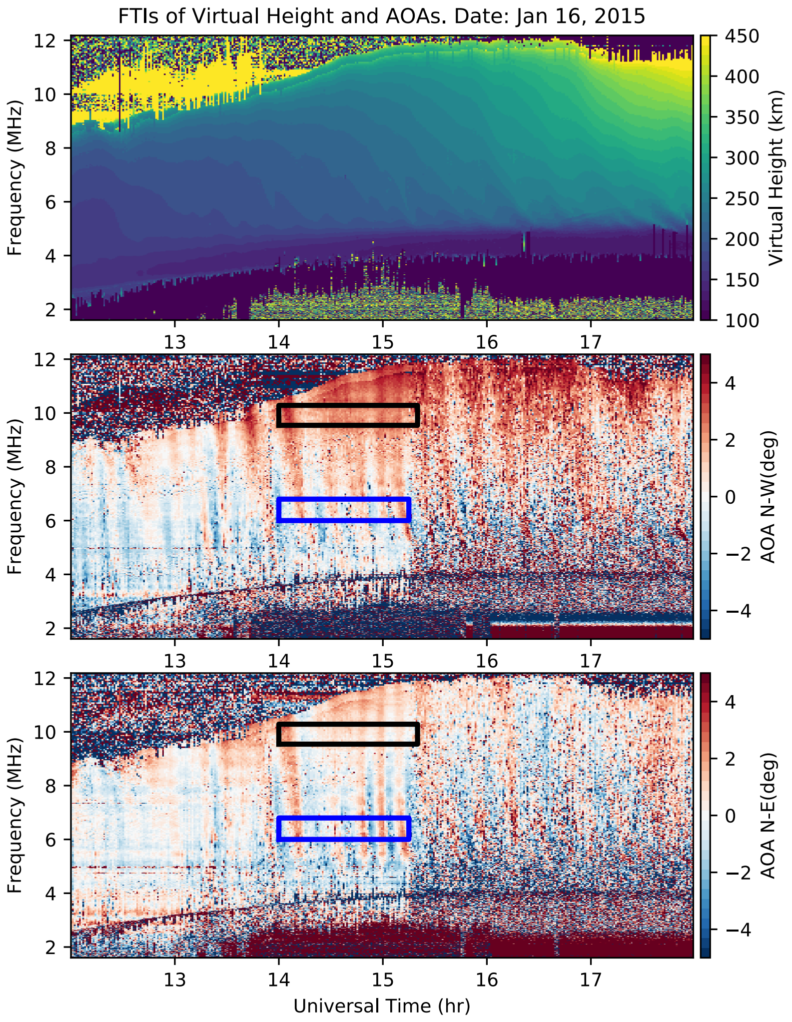

Figure 3.27 – A repeat of Figure 3.25 but for time ranging from 12 to 17 UT. The regions highlighted with the blue and black rectangles are analyzed further in Figure 3.28

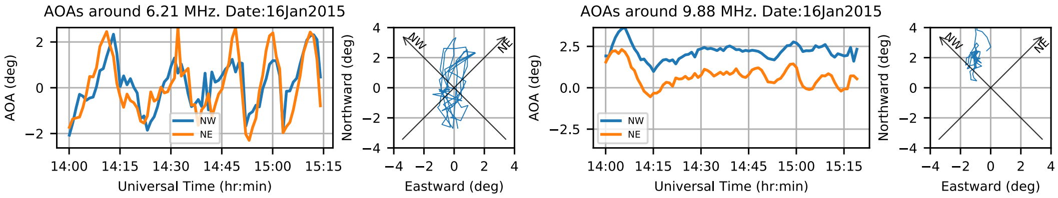

Figure 3.28 – Scatter plots of the frequency averaged AOA fluctuations corresponding to the cuts indicated with blue (left panel) and black (right panel) rectangles in Figure 3.27.

We notice that the AOAs at 6.2 MHz were oscillating symmetrically around the zenith in the North-South plane, while at 9.9 MHz (higher in altitude), the oscillations were asymmetrical with the centroid in the NW direction. We have two possible explanations for the AOAs getting asymmetrical with altitude:

(1) The steepening of the gravity waves is a well-known phenomena of the atmosphere [e.g. *Kudeki*, 1988]. It relates to how a perturbed atmosphere progresses from sinusoidal-shaped perturbations at lower altitudes to skewed sinusoids at high altitudes. To explain this phenomenon we make a plot with a simulated potential temperature in an isothermal atmosphere described by

$$\Theta(z) = \Theta_0 e^{\frac{(\gamma-1)}{\gamma}\frac{z}{H}} \tag{3.15}$$

disturbed by a monochromatic gravity wave

$$\frac{\delta\Theta}{\Theta} = Ae^{z/2H}\cos(\omega t - k_x x - k_z z), \tag{3.16}$$

depicted in the left panel of Figure 3.29. The right panel of the figure shows the plot of the disturbed potential temperature

$$\Theta(z) + \delta\Theta, \tag{3.17}$$

for $\Theta_0 = 1$, $A = 0.001$, $\gamma = 7/5$, and $k_x H = -k_z H = 2\pi$. Note that equipotential surfaces exhibit steepened sinusoid shapes at higher altitudes. If one assumes that ionospheric densities are advected like a passive scalar, then reflecting density surfaces would adhere to the steepened contours. In the figure, the short white line represents one such surface acting as a reflection plane of VIPIR EM pulses at $7/H$ of altitude, a preferred AOA for VIPIR pulses. This can help us identify the direction of the horizontal component of the gravity wave, because the horizontal component of $\mathbf{k}_{\mathrm{VIPIR}}$ points in the same direction as the horizontal component of

$\mathbf{k}_{\text{IGW}}$.

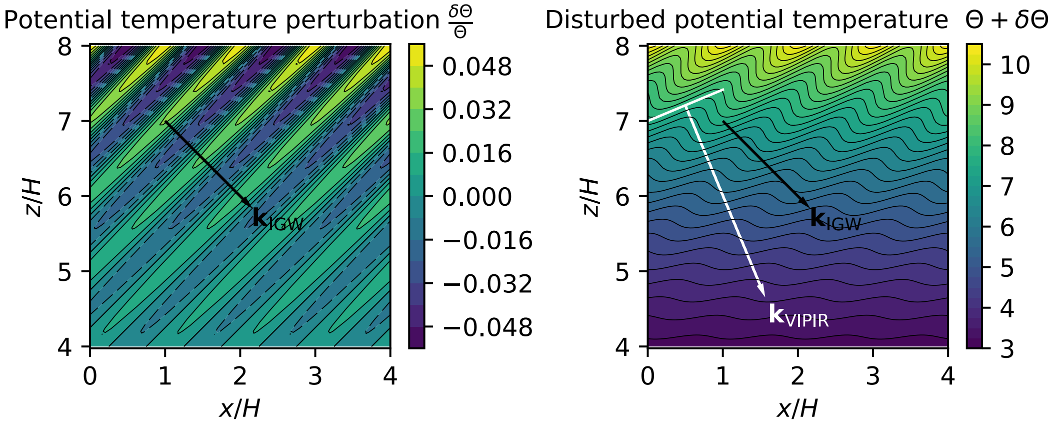

Figure 3.29 – Left panel: Contour map of the perturbation potential temperature. Right panel: Total potential temperature distribution. The vector $\mathbf{k} = \mathbf{k}_x + \mathbf{k}_z$ represents the wave vector of the gravity wave. Notice how the wave steepens as it goes higher in altitude. The white line represents a possible reflection plane and the white arrow the reflected EM wave.

(2) At the magnetic equator, with the magnetic field lines parallel to the ground, if $\mathbf{k}_{\text{IGW}}$ has an horizontal component in the North-South direction, the plasma density will accumulate along the phase fronts as shown in Figure 3.30. The thick wave fronts depicted in the figure represent regions with larger plasma density than the dashed thin lines. As the gravity wave pushes the atmosphere up and down according to the depicted arrows, the plasma, following the magnetic field lines, gets pushed towards the thick lines from both sides; likewise, the plasma is pushed away from the dashed thin lines.

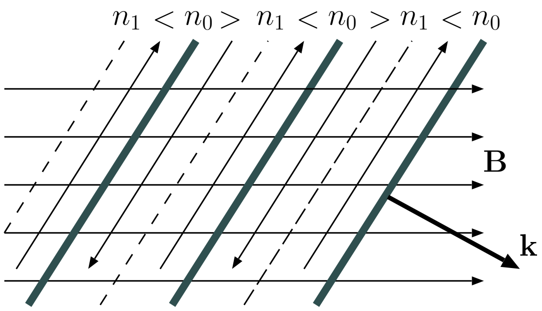

Figure 3.30 – Plasma accumulation at the wave fronts of a gravity wave in the magnetized ionosphere.

From the discussion of (1) and (2) we conclude that both mechanisms would imply that waves would be arriving from the sector of the observed centroid of the AOA. Lets see what the data tells us:

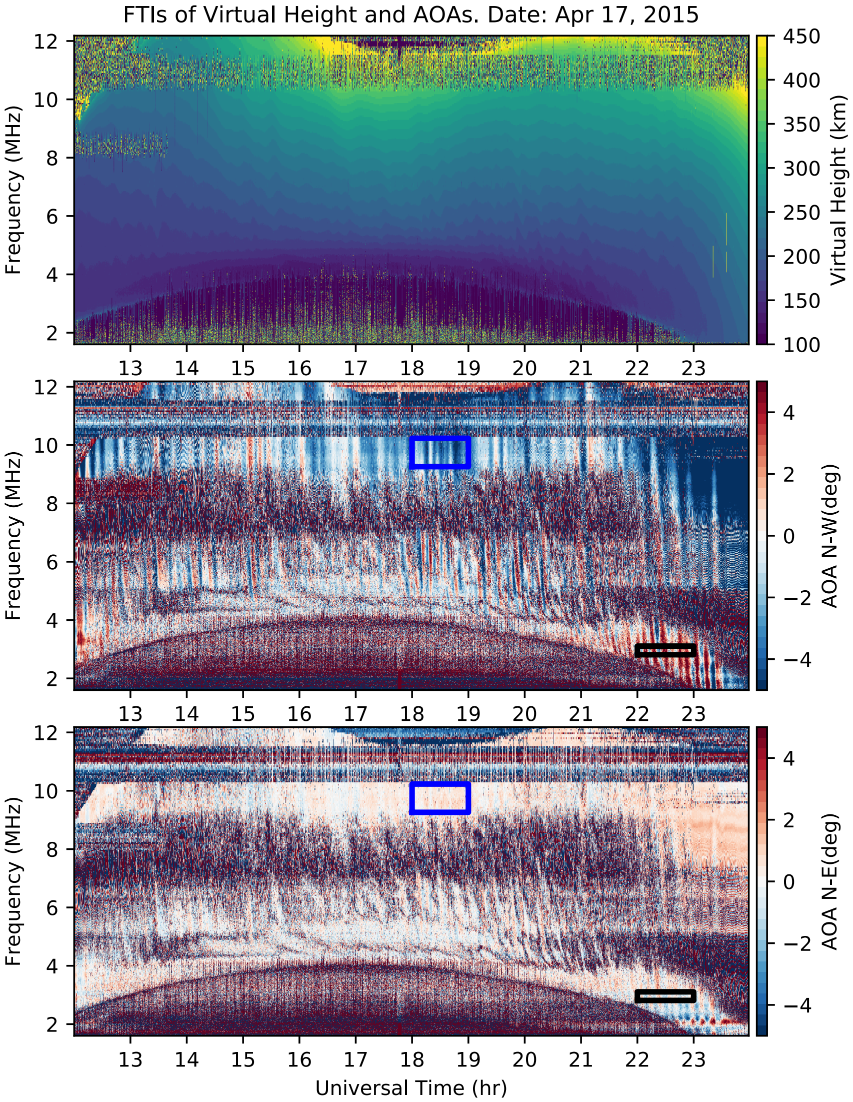

Figure 3.31 – Repeat of Figure 3.27 for April 17, 2015.

Observations

Going back to Figure 3.28, since the centroid of AOAs was leaning towards the North-West direction, that would imply that the IGW had the horizontal wave vector pointing to the South-East direction. AOA maps like the ones in

Figure 3.25 show how the waves, crossing the atmosphere, change propagation directions in time, e.g. 16 UT vs. 23 UT. In the same figure, at 16 UT we see that N-E AOAs show angles oscillating around 2.5 degrees, while at 23 UT, the N-E AOAs show angles oscillating around -2.5 degrees. An example of FTIs for April 17, 2015, is shown in Figure 3.31. In this figure, notice that not all the regions in the AOA maps show clear coherent phases; e.g., in the time range from 16 to 23 UT and from 2 to 6 MHz the AOAs look rather random, but still the downward phase progressions can be recognized. We have noticed that when the O- and X-traces coincide, then there is no clear separation of the modes, as a consequence the cross-correlation phases contain information from both O-mode and X-modes mixed, at least with our current methodology to extract AOA information. In order to extract information about the wave propagations we will use the places where AOA were well resolved.

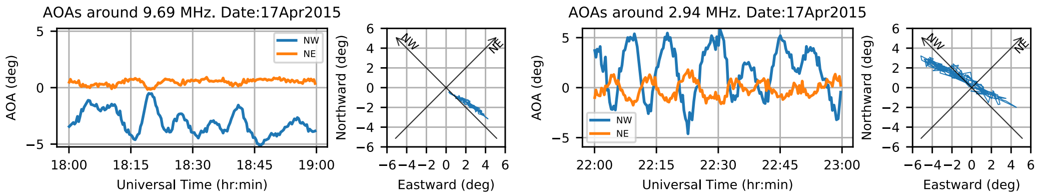

Figure 3.32 – Repeat of Figure 3.28 for April 17, 2015. Left panel: AOAs obtained from the region highlighted with a blue rectangle in Figure 3.31. This shows the centroid leaning towards SE, which means that the wave has $\mathbf{k}_x$ pointing to the NW. Right panel: AOAs corresponding to the region highlighted with a black rectangle in Figure 3.31. This shows that the centroid of oscillations was slightly leaning towards WNW, hence $\mathbf{k}_x$ was pointing to the ESE.

Figure 3.32 shows the frequency averaged AOAs from the highlighted rectangles in Figure 3.31. From Figure 3.32 we can tell that at 18 UT we seem to have a IGW with horizontal wave vector pointing to the NW, while at 22 UT, the centroid of oscillations marginally leans towards WNW, meaning that the horizontal component of the IGW was pointing to the ESE direction. In Figure 3.33

we show examples of AOA extractions for two consecutive days: April 18 and April 19, 2015. The examples show similar behavior for both days: horizontal component of IGW was pointing to the WNW at 18 UT and pointing to the ESE at 22 UT. Figure 3.34 corresponds to January 30, 2016, and is the last day we are going to analyze. On this day we see that the propagation direction of IGW based on AOA analysis changed from NNE around 22 UT to E around 23 UT, as depicted in the AOA cuts in Figure 3.35.

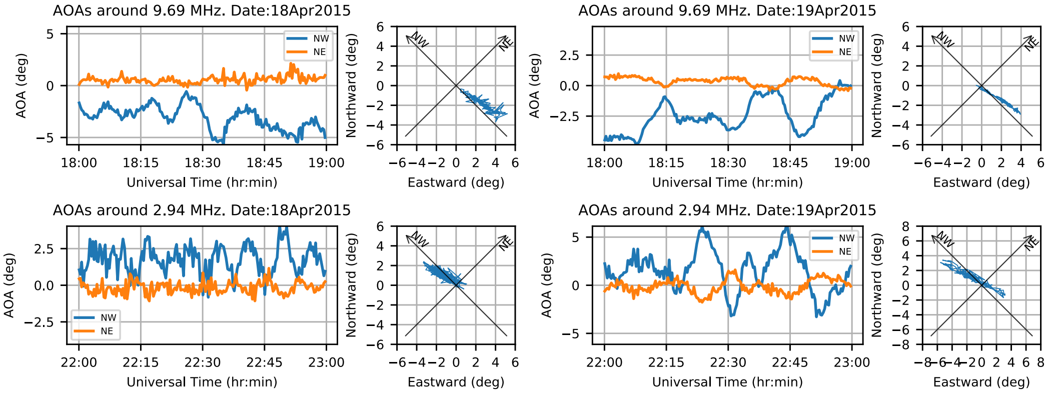

Figure 3.33 – Repeat of Figure 3.28 for April 18 and April 19, 2015. The AOA samples are taken at the same time and sounding frequency for two consecutive days. Both days agree in IGW horizontal component direction to the WNW at 18UT and to the ESE at 22 UT.

3.3.3 Alternative ways of representing VIPIR data

Figures 3.36 and 3.37 show different ways to represent VIPIR observations. Figure 3.36 is similar to Figure 3.23 but for January 30, 2016, and only showing the day-time ionosphere. A color scheme of 32 points has been used in order to emphasize the constant virtual height contours. These contours display oscillations that we are going to see in detail in Chapter 4. Figure 3.37 shows an alternative representation of the O-mode reflection height: Each curve represents virtual height versus time with the frequency indicated by its color. We will use this kind of representation in Chapter 4, when we compare it with 50 MHz radar data.

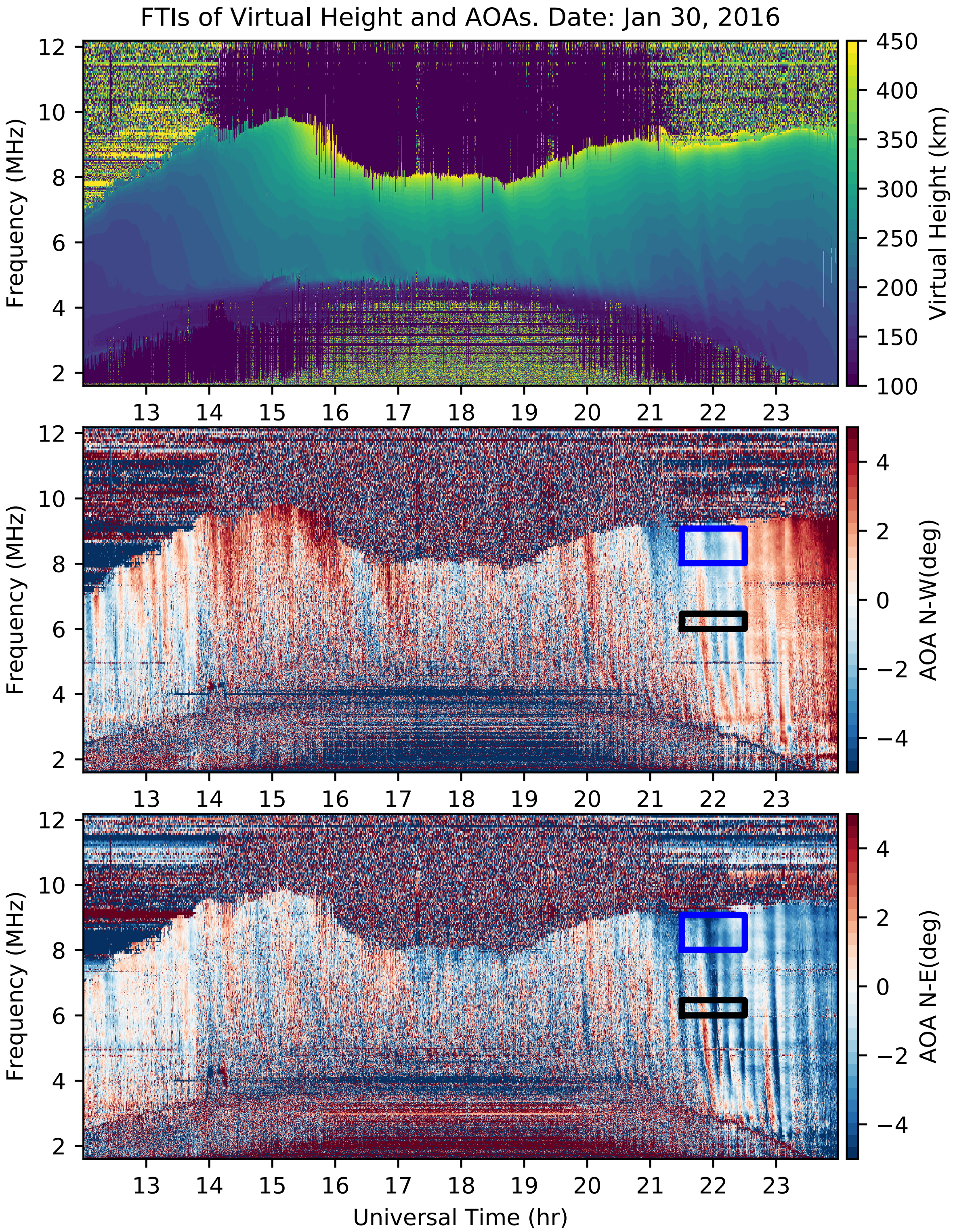

Figure 3.34 – Repeat of Figure 3.27 for January 30, 2016.

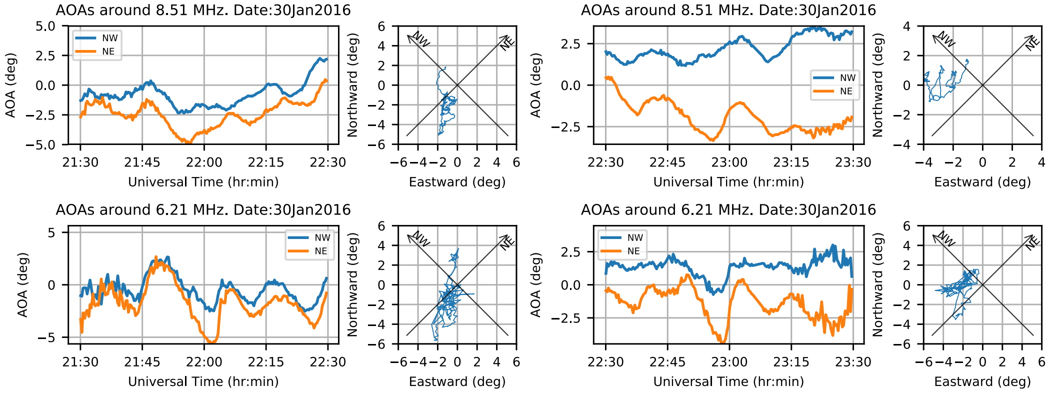

Figure 3.35 – Repeat of Figure 3.28 for January 30, 2016. The first column of panels represents the AOAs obtained from the region highlighted with a blue and black rectangles in Figure 3.34, while the right panel corresponds to same sounding frequency region but one hour later. While at 22 UT $\mathbf{k}_x$ points to the North, one hour later, at 23 UT, $\mathbf{k}_x$ points to the east.

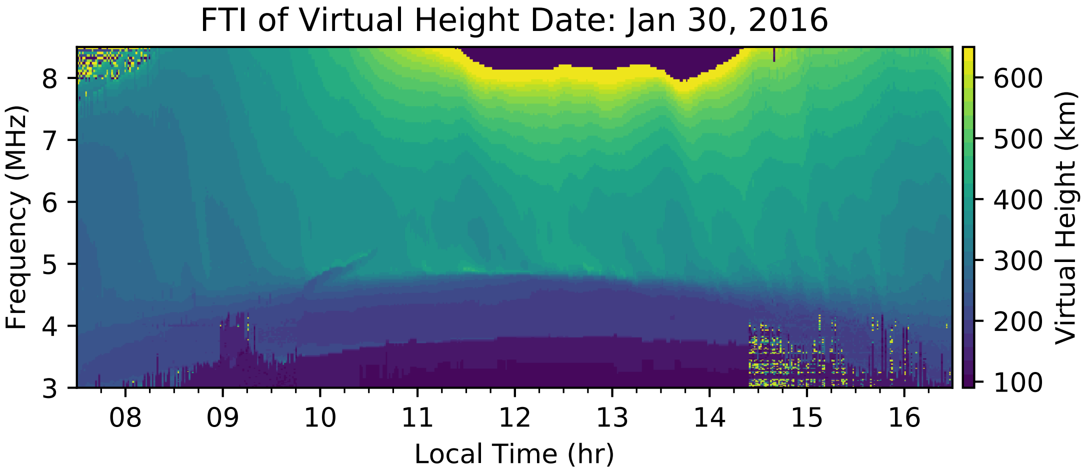

Figure 3.36 – Frequency-time-intensity (FTI) plot of O-mode ionosonde virtual reflecting height taken by the ionosonde VIPIR on January 30, 2016. To obtain the visual effect of virtual heights contours, the matplotlib colormap has been resampled with only 32 points out of its original 256 points.

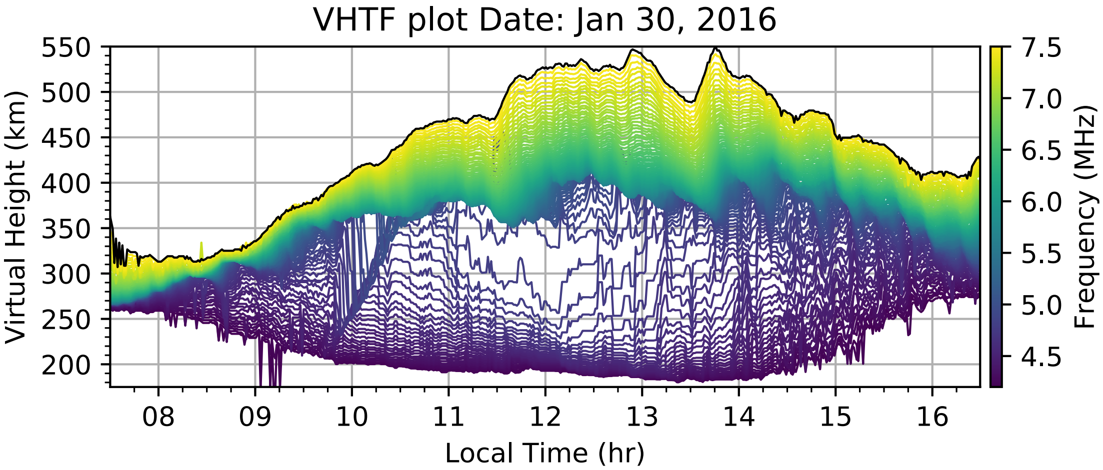

Figure 3.37 – An alternative representation of the O-mode virtual reflection height, transmission frequency, and observation time data of Figure 3.36: here, virtual reflection height time-series tagged by the transmission frequency are plotted as individual curves. The plot color indicates the VIPIR transmission frequency.

CHAPTER 4

COINCIDENT INTERNAL GRAVITY WAVE SIGNATURES DETECTED WITH VIPIR IONOSONDE AND 50 MHZ 150-KM ECHOES AT JICAMARCA

RTI plots from 3-meter Bragg scattering that are routinely detected around the 150 km altitude region at JRO exhibit thin undulating layers with periods of about 5-15 minutes [e.g. *Kudeki and Fawcett*, 1993]. Some of these layers show a thin backscatter power return adjacent to a thin layer without detectable power returns. It has been proposed that these oscillations imply a modulatory role of gravity waves propagating in the region [e.g. *Røyrvik*, 1982]. Using data obtained with a vertical incidence pulsed ionospheric radar (VIPIR), *Negrea et al.* [2016] have demonstrated the potential of this instrument to fully diagnose acoustic gravity waves (AGWs) by means of the dynasonde technique. In this chapter we develop simple techniques based on VIPIR raw data and display virtual reflecting height vs. time plots that show undulatory fluctuations of periodicity similar to that shown by the thin layers of the 150-km echoes. We claim that the AGW are indeed the modulatory force that shapes the 5-15 minute period fluctuations seen in the meter-scale radar backscatter at JRO.

4.1 Comparison between JRO 150-km Echoes RTIs and VIPIR Virtual Height Maps

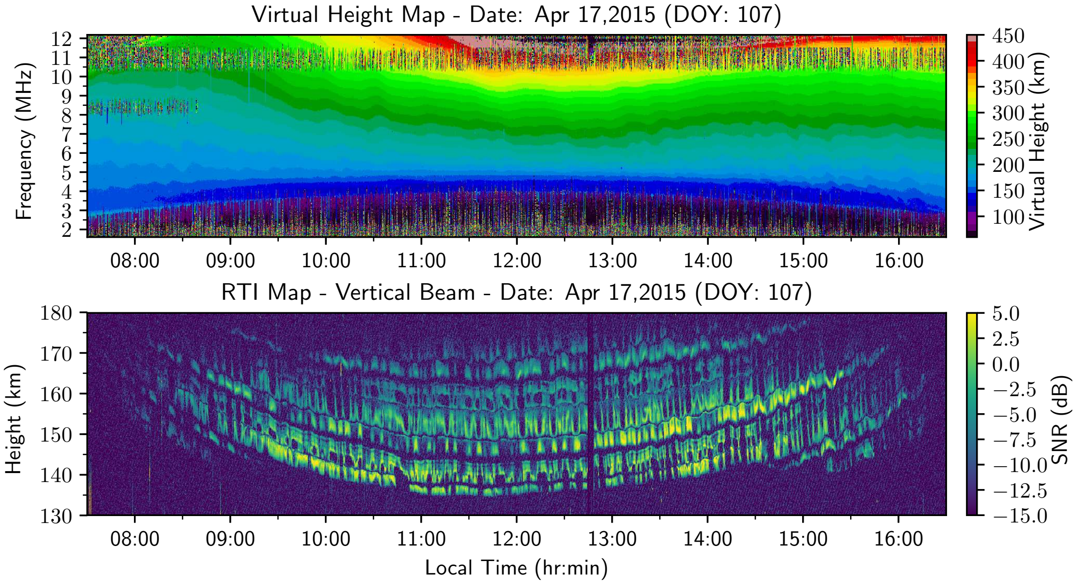

Figure 4.1 – Top panel: VIPIR map depicting the virtual height of reflection of O-mode transmissions as a function of observation time and transmission frequency. Bottom panel: A repeat of JRO RTI map of Figure 1.2.

Figures 4.1 and 4.2 show in their top panels frequency-time-intensity (FTI) plots of virtual height of the O-mode signal detected using the VIPIR ionosonde at JRO on April 17, 2015, and on their bottom panels concurrent RTI plots of signal-to-noise ratio (SNR) obtained at JRO using the MST-ISR-EEJ [e.g. *Akgiray*, 2007; *Lehmacher et al.*, 2009] mode with a beam pointing vertically slightly off of perpendicular to Earth's magnetic field (radar beam pattern can be seen in Figure 3.9e). The plots share the same time axis in local time (LT) for April 17, 2015, and for January 30, 2016. We notice that the thin "forbidden" zone layer undulations of the 150-km echoes shown in the RTI plot seem to coincide with the virtual height undulations shown in the FTI plot. In order to make this observation more evident, we will extract from the RTI the height information of one of the 150-km layers and plot it with the same time axis with virtual heights of VIPIR corresponding to several plasma frequencies. We will notice that the 150-km layer fluctuations are in agreement with the virtual height fluctuations for a particular plasma frequency. Hence, by matching their oscillations, we are also obtaining the plasma frequency associated to that 150-km echo layer.

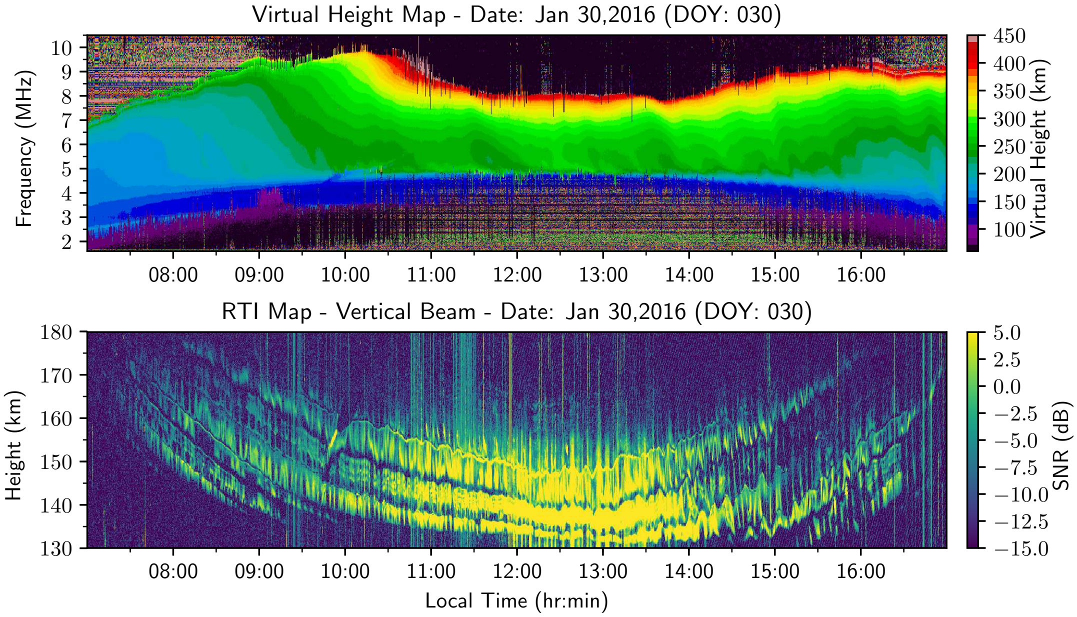

Figure 4.2 – A repeat of Figure 4.1 for January 30, 2016.

4.2 Methodology

For the comparison of the virtual height fluctuations detected with VIPIR and the layers of 150-km echoes we focused our attention to one of the thin "forbidden" zone layers. Figure 4.3 shows the 150-km echoes, in an RTI built based on data taken on April 17, 2015, with one of the "forbidden" or "quiet" zone layers highlighted with a red curve. This layer was chosen because its contrast was enhanced by an even thinner layer with slightly enhanced power just below it as can be seen in a blow-up RTI in Figure 4.4. For the detection of the thin layer, a large RTI figure 16 inches wide and 4 inches tall with 400 pixels/inch was recorded and a graphics tool was used to manually paint a red line following the bottom of the layer. Next, a code was written in order to read the modified figure and get the height and time information from the red line/150km layer. Using the information from the detected layer, an RTI with the layer superimposed to it was created (see Figure 4.3).

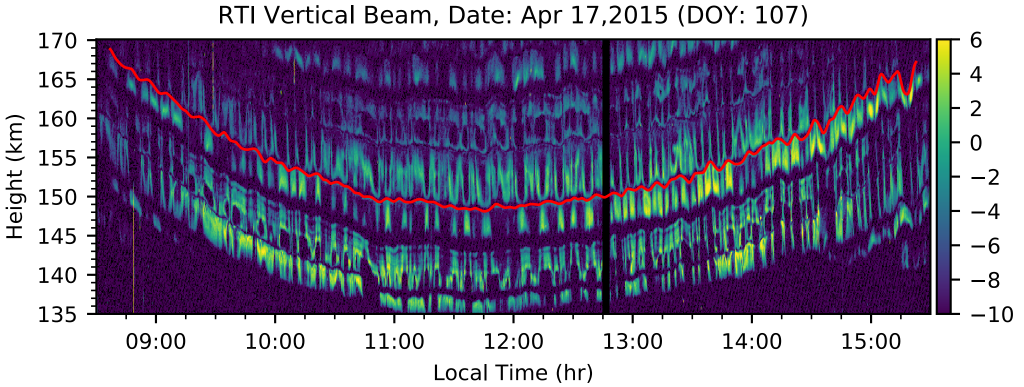

Figure 4.3 – RTI similar to that in Figure 1.2 showing one of the "forbidden" thin layers highlighted with a red curve.

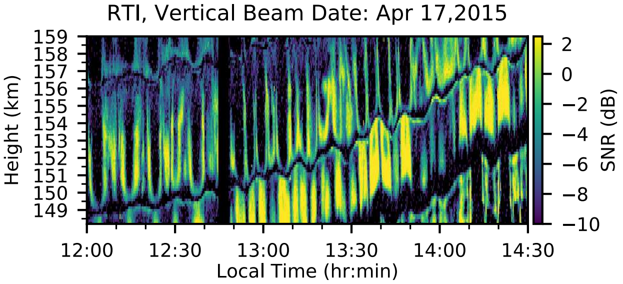

Figure 4.4 – RTI showing a thin "forbidden" zone layer ranging from about 149 km to 159 km of altitude. Notice that below that layer there is an enhanced thin layer that enhances the contrast of this layer and is useful for its detection.

4.2.1 Spectral analysis of the 50 MHz 150-km echo thin layer height fluctuations

Figure 4.5 shows the spectral content of the whole time series of height locations of the thin undulating layer aforementioned both in logarithmic and in linear scales. The data set consists of 3731 points with a sampling period of 6.52 seconds.

To obtain the power spectrum the data has been Fourier-transformed using a Hanning window. We notice that in the range of frequencies higher than 30 minutes period the frequency corresponding to the largest power is 1.479 mHz ≈ 11.27 min which is in the range of known oscillation periods of the 150-km echoes. Based on the power levels seen in the spectrogram we have decided to select 3 frequency regions that we call large-scale (frequencies less than 0.2 mHz), mid-scale (frequencies between 0.2 mHz and 0.7 mHz), and small-scale (frequencies between 0.7 mHz and 4 mHz). In order to compare the 50 MHz150-km oscillations with the virtual height fluctuations obtained from VIPIR we focus only on the small-scale range. The quasi-periodic fluctuations change in time throughout the day and to get an idea of how these oscillations change in time the reader is referred to the spectrogram in Figure 4.6 .

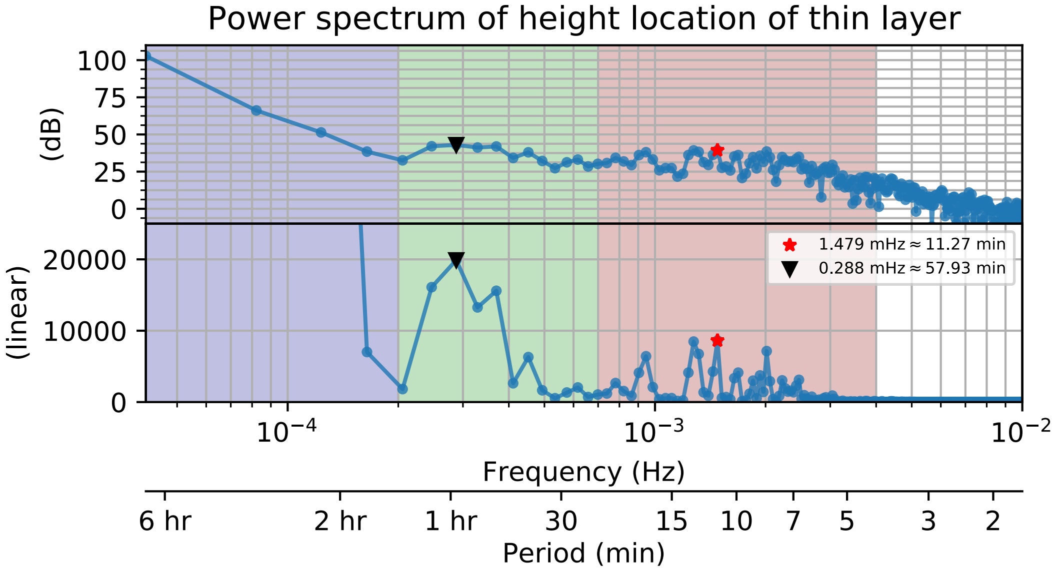

Figure 4.5 – Power spectrum in logarithmic and in linear scales of the height fluctuations of the thin “forbidden” zone layer from Figure 4.3. The frequency axis is specified both in Hz and in periods. The three highlighted frequency regions correspond to what we refer to as large-scale (blue), mid-scale (green), and small-scale (red) frequencies. In the plot legend we are indicating with distinct markers the maximum in the small-scale region (about 11 minutes), and the maximum in the mid-scale region (about 1 hour).

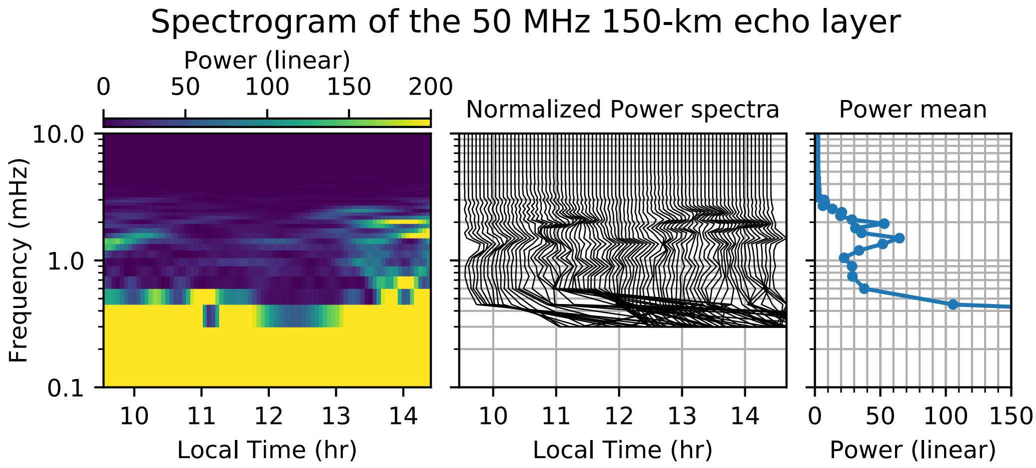

Figure 4.6 – Spectrogram in linear scale of the 50 MHz 150-km echo layer that is highlighted in Figure 4.3. This spectrogram has been obtained with a running FFT of 1024 points with 990 overlapping points between power profiles. To obtain the figure in the center panel each power spectrum has been normalized with its maximum in the range of frequencies larger than 0.6 mHz (27.8 min) and is plotted in linear scale. The plot in the right panel shows the mean of the power from the first panel. Notice that the energy spectrum of the small scale fluctuations is mainly in the frequency range from 0.6 mHz (~27.78 min) to 4 mHz (~4.17 min).

4.2.2 Different scale wave fluctuations in the 50 MHz 150-km echo heights for Apr. 17, 2015

In order to observe the influence of the different bands described in the previous subsection, three filters will be used: a lowpass filter with cutoff frequency of 0.2 mHz/1.39 hr for the large-scale band, a bandpass filter with cutoffs 0.2 mHz/1.39 hr and 0.6 mHz/27.8 min for the mid-scale band, and a bandpass filter from 0.6 mHz (~27.8 min) to 4 mHz (~4.17 min) for the small-scale band. Figure 4.7 shows the fluctuations corresponding to the small-scale fluctuations in red around what we call the trend which is the sum of large- and mid-scale fluctuations. The frequency response of the filters for the small-scale, mid-scale and large-scale regions are depicted in Figures 4.8, 4.9 and 4.10 respectively.

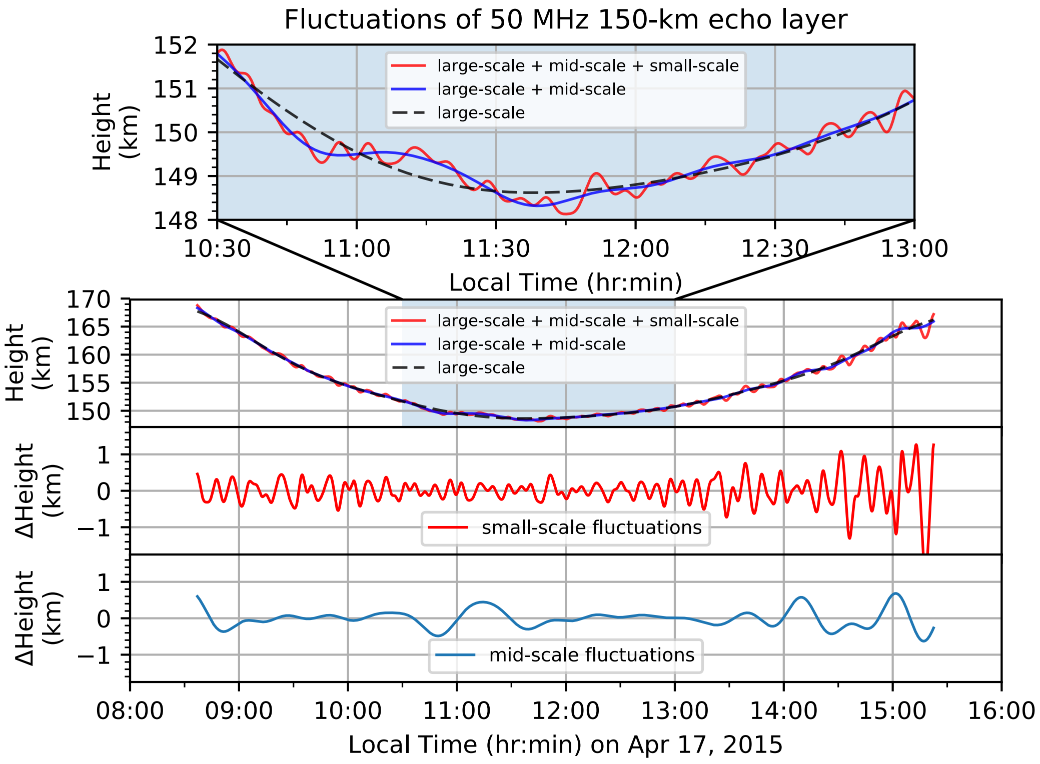

Figure 4.7 – Top panel: The red curve is the same thin layer 50 MHz 150-km echo layer from Figure 4.3. The black curve represents the large-scale fluctuation, i.e. frequencies less than 0.2 mHz (periods larger than 1.39 hr), while the blue curve represents both large-scale and mid-scale signal added together representing the trend, where mid-scale refers to frequencies in the range from 0.2 mHz (1.39 hr) to 0.7 mHz (23.81 min). Center panel: Same as the top panel but for the whole extent of the layer in time and space. Bottom panel: Mid-scale fluctuations.

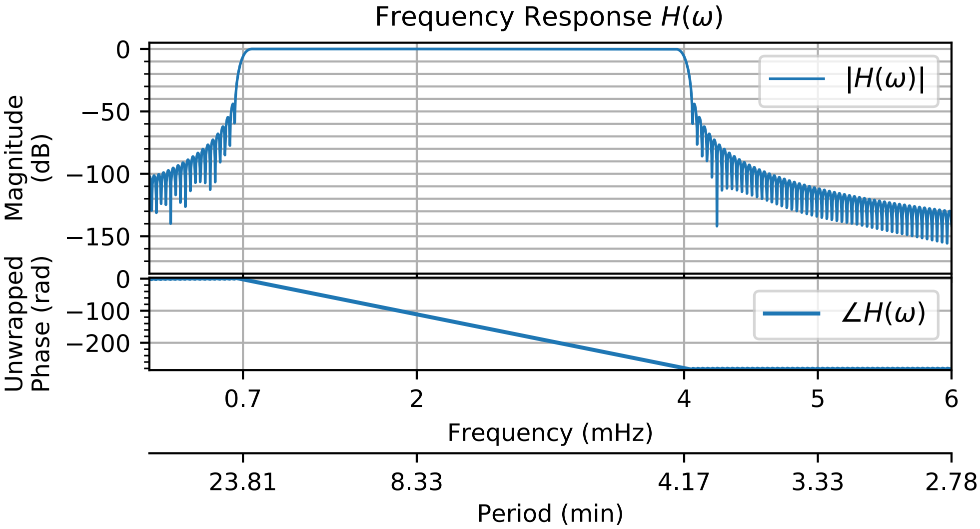

Figure 4.8 – Frequency response of the filter used to extract the small-scale fluctuations. It is a finite impulse response (FIR) bandpass filter with pass band from 0.7 mHz (~23.81 min) to 4 mHz (~4.17 min). This filter has been designed using the software package scipy.signal.firwin with 4096 taps and the Hanning window.

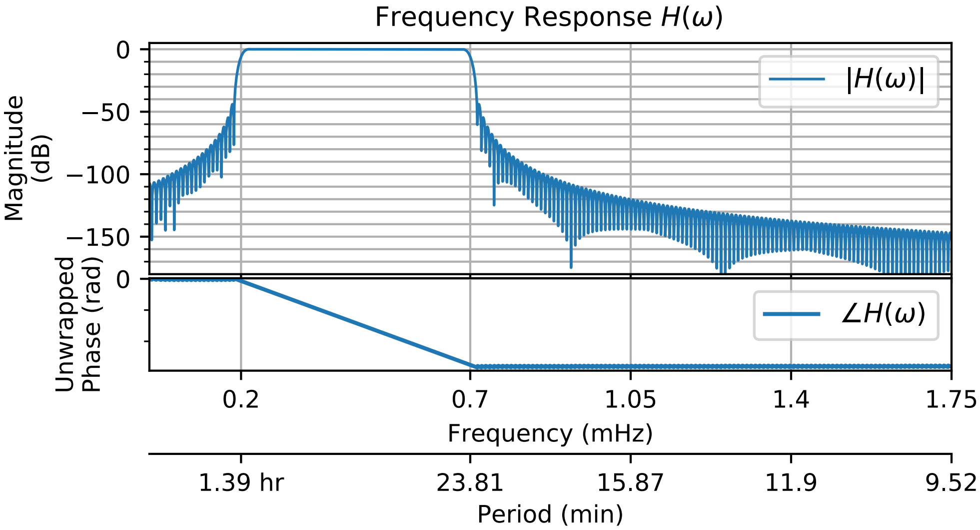

Figure 4.9 – Frequency response of the filter used for extracting the mid-scale fluctuations. It is a FIR bandpass filter with pass band from 0.2 mHz (1.39 hr) to 0.7 mHz (23.81 min). This filter has been designed using the software package scipy.signal.firwin using 16384 taps and the Hanning window.

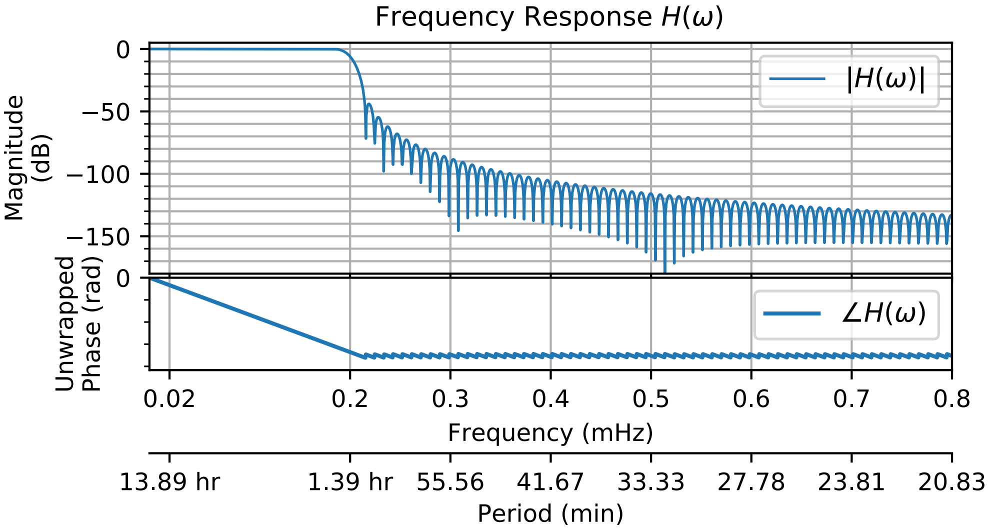

Figure 4.10 – Frequency response of the filter used for extracting the large-scale fluctuations. It is a FIR lowpass filter with cutoff frequency 0.2 mHz (1.39 hr). This filter has been designed using the software package scipy.signal.firwin using 16384 taps and the Hanning window.

4.3 Comparing Fluctuations of VIPIR Virtual Height and JRO 50MHz 150-km Echo Height

In Figure 3.37 and with more detail in Figure 4.11 we see a dense set of virtual reflection height versus time plots, each one colored by the corresponding ionosonde frequency shown in the color bar. Ripples exhibiting downward phase progression in Figure 4.11 are caused by the distortion of ionospheric iso-density contours by propagating waves through the region. The rippling of the ionosphere is also evident in the AOA maps, e.g. Figure 3.27, that show that reflections are not always coming from above; instead, they originate at the points where the line-of-sight starting from the antenna towards the reflecting height makes a 90 degree angle with the IGW-modulated iso-density contour. These fluctuations have all the characteristics of IGW that we discussed in section 2.2.2: we observe downward phase progression signatures as seen in Figure 4.11 for the virtual height, and in Figure 3.27 for the AOA, we observe as well that the implied vertical wavelengths and oscillation periods are all consistent with propagating gravity waves through the region with intrinsic frequencies just below the local Brunt-Väisälä frequency of about 10 min. Also we see that shorter wavelengths seen at lower altitudes are no longer seen at higher altitudes, meaning that they are being damped due to viscosity.

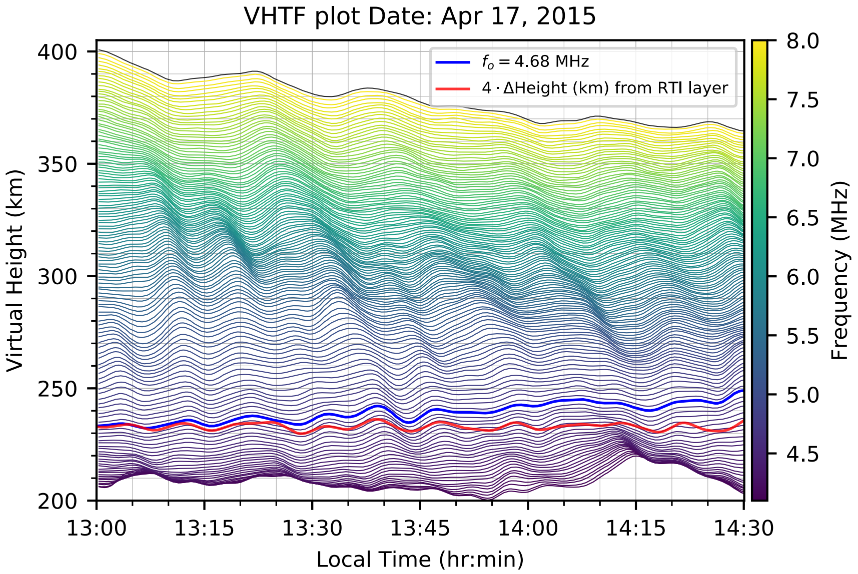

Figure 4.11 – Representation of the O-mode virtual reflection height, transmission frequency, and observation time similar to the one described in Figure 3.37. The data represents a 1.5 hr segment of Figure 4.1. The thick red curve indicates a scaled-by-4 curve taken from the 50 MHz RTI segment depicted in Figure 4.12, while the thick blue virtual height curve corresponding to 4.68 MHz transmission frequency has been highlighted.

In Figure 4.11 the overlaid red curve represents the small-scale time variations of the "forbidden zone" displacement of 50 MHz backscatter taken from Figure 4.12. This establishes a direct link between the VIPIR ionosonde and VHF 150-km echo radar data. A de-trended version of the red curve taken from Figure 4.12, representing real scattering heights centered about 155 km, best matched the virtual height variations depicted in Figure 4.11 at just about 232 km of virtual height and 4.68 MHz of plasma frequency corresponding to a plasma density of 2.72×10^{11} m^{-3}, as the blowup Figure 4.11 depicted in Figure 4.13 shows. The de-trending of virtual height curves in Figure 4.13 has been done with the same small-scale bandpass filter used for the de-trending of the 50 MHz 150-km echo layer, i.e. the filter in Figure 4.8.

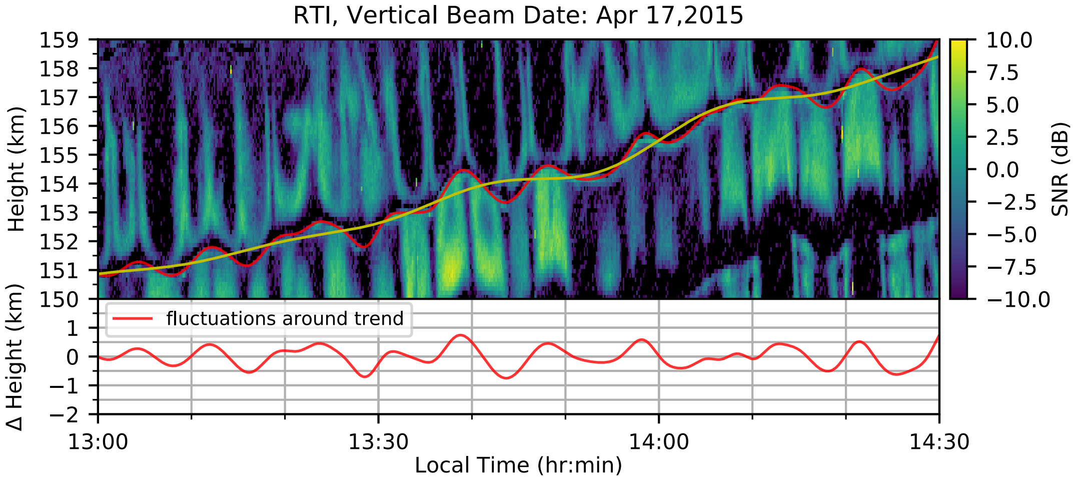

Figure 4.12 – Top panel: RTI segment overlaid with a red curve highlighting a “quiet zone” or “forbidden zone” of scattering between a pair of scattering layers of the RTI. Bottom panel: a plot versus time of a de-trended version of the red curve from the top panel.

Obtaining the virtual heights for low frequencies, used to construct Figure 4.11, was done by applying the algorithm described in the appendix A, followed by a revision of each individual O-trace plot and manual correction of the traces where the algorithm failed, as explained in the Appendix. A more robust O-trace detecting algorithm or a true height inversion technique could help do more detailed comparisons between VIPIR and JRO ISR. Nevertheless, FTVH plots in Figures 4.2 and 4.1, that where made with the automatic O-trace detection algorithm, show fluctuations of the same order as those of the 150-km echo layer displacements, though direct match with 150-km echoes was not possible because the automatically detected O-traces did not accurately resolve accurately the lower frequencies.

In order to compare true height fluctuations from VHF radar returns vs.

virtual height (VH) fluctuations in Figures 4.11 and 4.13 we used a scaling factor of 4 times the radar true height fluctuations to match those of the VH fluctuations. This factor was obtained by manually adjusting it until the fluctuations of both instruments were of the same order. Ideally, we would use true heights from ionosonde inversions to do the comparison with radar data, but obtaining the true height from the valley region is challenging especially because ionosonde pulses do not reflect from lower density regions that are hidden above higher density regions. Nevertheless, by comparing the de-trended oscillations we focus mainly in comparing fluctuations phases, which show great agreement between radar 150-km displacements and VIPIR virtual heights and helped us make the claim that IGW are indeed responsible for the undulating shape of the "forbidden" 150-km echo bands.

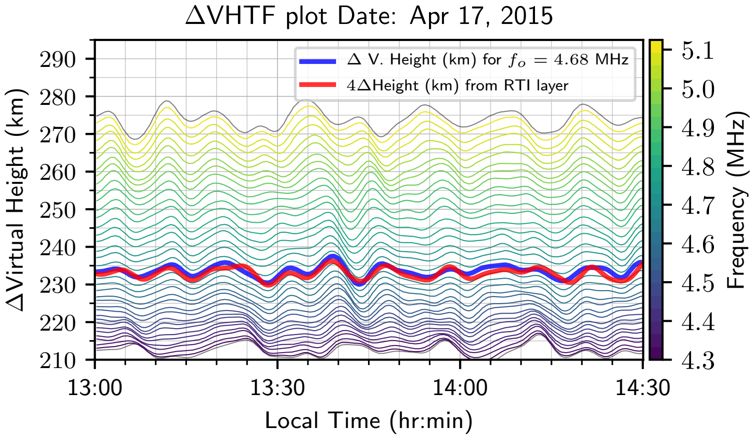

Figure 4.13 – A blow-up of Figure 4.11 near the virtual reflection height at 4.68 MHz corresponding to the true height of 150-km echoes. In this case, the virtual height curves have been de-trended but preserve their initial virtual height. The thick red curve is a scaled-by-4 version of the de-trended 150-km echo layer from Figure 4.12.

4.4 Comparing Fluctuations of Vertical Plasma Drift with Fluctuations in the Height of 150-km Echoes

In section 3.2.2 it was shown how to get upward $\mathbf{E} \times \mathbf{B}$ plasma drift from 50 MHz Doppler spectra estimations at JRO during MST-ISR-EEJ campaigns. Figure 3.14 showed an RTI plot of vertical drifts for data taken on April 17, 2015. Even though the vertical drift seems to have some variability with height, as is evident in Figure 3.12, we will use the height averaged upward plasma drifts to compare it with the small-scale oscillations of the 150-km echo displacements. First, we are going to observe the spectral content of the estimated vertical drifts. Figure 4.14 shows a spectral analysis of the time series of the height averaged vertical drift. To obtain the spectrum of the 400 data points with sampling frequency of 1 min, a Hanning window was applied before taking the FFT. We notice that with a criterion similar to that for the 50 MHz 150-km echo layer spectral analysis, we recognize three frequency regions that are similar to those found in the frequency spectrum of the 150-km echo layer displacements. We continue our comparison of the small-scale frequency region, and we see in Figure 4.15 that while the fluctuations seem to be of the same scale, in general they do not agree in phase. At some moments they seem in phase, e.g. between 9 and 10 L.T, and at other moments they are 180 degrees out of phase, e.g. between 13:00 and 13:45, or around 14:30. The fluctuations that we are reporting here are a first time observation, since in previous studies these fluctuations were not resolved. This might have been because the observed fluctuations are small compared to the full velocities: only 0.46 m/s r.m.s. compared to ~20 m/s. Another factor that increases our sensitivity to small Doppler shift fluctuations is the small bandwidth of ±10 m/s that the MST-ISR-EEJ offers. The drift fluctuations not being in sync with the small-scale fluctuations of the 150-km echo layer could be a consequence of the propagation direction of the IGWs. In certain propagation directions, the velocities that are induced are in phase with the displacement fluctuations, while for other propagation directions that is not the case. It is believed that any gravity-wave-generated electric fields, that would influence the $\mathbf{E} \times \mathbf{B}$ upward drift, will be shorted out by the highly conductive E-region. The shortening, in this case, might not be happening with full efficiency.

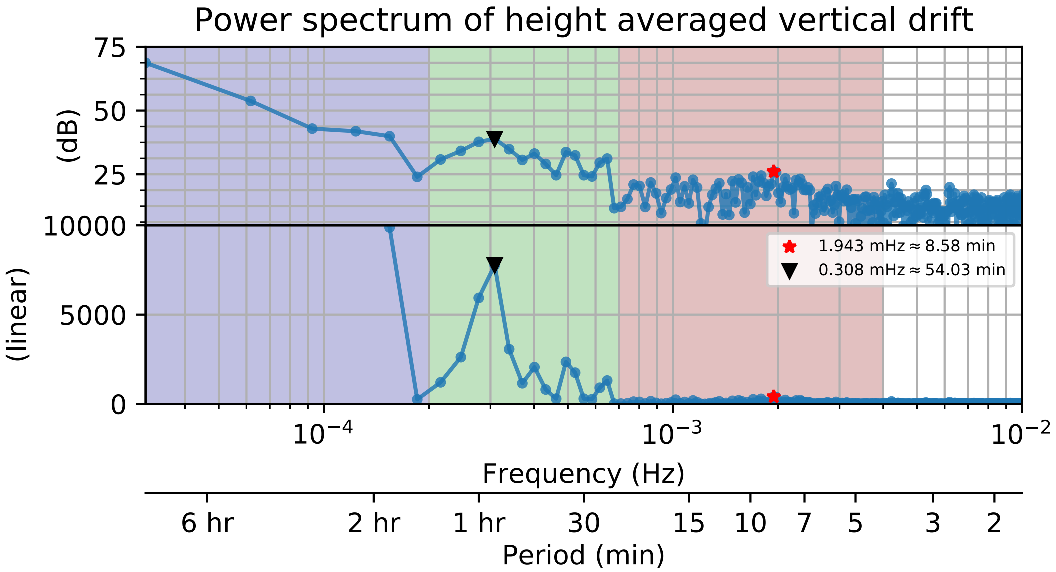

Figure 4.14 – Similar spectral analysis as in Figure 4.5 but for the height averaged vertical drift.

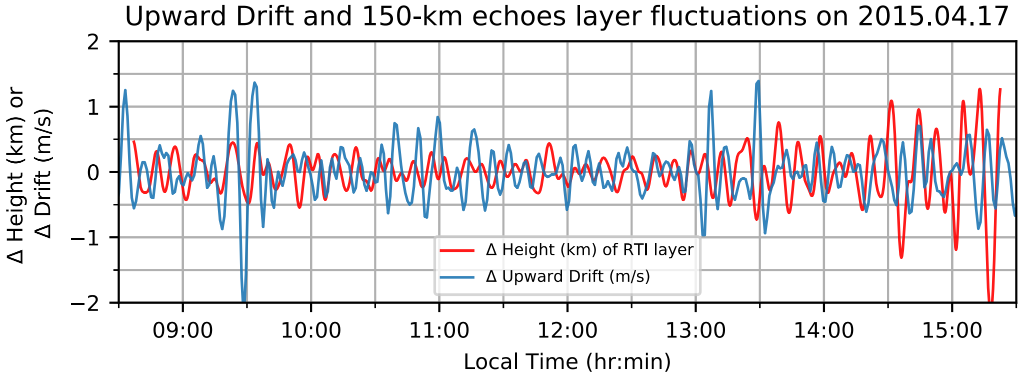

Figure 4.15 – Comparison of the fluctuations of 50 MHz 150-km echo plasma drift and the height of the thin “forbidden” zone layer.

4.5 Discussion

The high sensitivity of the JRO radar and the high temporal and spatial resolution of the MST mode (described in section 3.2) allowed us to detect significant backscatter power from 150-km echo RTIs at a spatial resolution of 150 m and about 8 seconds of time resolution. Figures 4.4 and 4.3 show the level of detail that can be found in the VHF 150-km echoes at JRO. The thin “forbidden” or “quiet” layer could be followed almost completely throughout the day, which helped us characterize it and compare it with VIPIR data. Ideally an inversion of the true height of electron density should take place in order to do comparisons with radar data. But doing inversions of true height at the valley region presents some challenges especially because the ionosonde pulses cannot penetrate into regions with less electron density than regions at lower altitudes. What existing inversion techniques do [e.g. *Scotto*, 2009] is model the E-F valley region with some smooth function with few parameters to do the inversion. For that reason a joint ISR-ionosonde effort becomes relevant and it should be part of the future directions following the current study. Nevertheless the analysis of virtual height fluctuations is useful since by de-trending the virtual heights and the 150-km echo displacements we focus on their coincident phases. The amplitudes of the fluctuations observed in the virtual heights would scale down when transformed to true height. In fact, in Figures 4.11 and 4.13 we needed to scale up by 4 times the height fluctuations of the 150-km echo layer in order to do the comparisons.

Fluctuations in the vertical plasma drifts obtained from the 150-km echoes seem to have the same oscillation frequencies as the vertical displacements of the 150-km echo layer, but do not necessarily share the same phase. These plasma drift fluctuations are small compared to the full velocities and in earlier work such fluctuations were either not noticed or ignored. Absence of fluctuations would mean total shorting out of the gravity wave induced polarization electric fields by E-region conductivity. However, a residual that we are noticing here indicates that shorting, though efficient, is not perfect.

Figure 3.12 showed how the plasma drift displays some gradients, and it also displays a very small downward phase progression, which is indicative of gravity wave activity. This is not surprising since it has been reported that F-region $\mathbf{E}\times\mathbf{B}$ drifts display signatures of modulation by gravity wave activity [e.g. *Kudeki et al.*, 1999; *Varney et al.*, 2009].

Another IGW signature that we notice by looking into the radar data is that the amplitude oscillations are larger at higher altitudes. This is evident in Figure 4.7 where fluctuations at 148 km around noon had 0.16 km of r.m.s. while fluctuations at 165 km around 15:00 LT had 0.82 km of r.m.s. We notice also that during the local morning hours the fluctuations had smaller amplitudes at the same altitude of those fluctuations at the local afternoon, but still larger than at the lower altitudes, which might indicate that IGW are being Doppler shifted by different horizontal wind magnitudes and/or different angles between the IGW horizontal wavenumber and the wind vector.

4.6 Summary and Conclusions

The main point that the reader should get from this chapter is that the great agreement in the VIPIR/50-MHz comparisons presented makes a strong case for IGW propagating through the equatorial valley region ionosphere and playing a crucial role in shaping the 50 MHz 150-km layers. *Oppenheim and Dimant* [2016] concluded through large-scale simulations that photoelectrons are enhancing the incoherent scatter (IS). While this conclusion might be valid, it addresses neither the cause of the suppression of IS seen in the “forbidden” zones, nor that of the pulsations and intricate structure shown by the data. Therefore we conclude that any theory that aims to explain the generation mechanism of the 150-km echoes that does not include the effect of internal gravity waves is going to be incomplete. It is only by finding the right mechanism that combines the inputs driven by gravity waves and inputs driven potentially by photoelectron effects, that a full explanation of how the necklace with its enhanced echo region as well as its “forbidden” regions are formed, can be achieved.

CHAPTER 5

SUB-MINUTE QUASI-PERIODIC (SMQP) POWER FLUCTUATIONS IN THE 150-KM ECHOES DETECTED AT JICAMARCA

In this chapter we report on the existence of sub-minute quasi-periodic (SMQP) fluctuations present in 150 km irregularities obtained at the Jicamarca Radio Observatory (JRO) located near Lima, Perú. Using a non-exhaustive search technique we have found SMQP fluctuations with periods ranging from a few seconds to about a minute. These periods are an order of magnitude shorter than the dominant quasi-sinusoidal altitudinal displacements with periods of about 5-15 minutes discussed in chapter 4. While we are claiming that the 5-15 minute oscillations imply a modulatory role for internal gravity waves (IGW) propagating in the region, the SMQP fluctuations, which also show an apparent height dependent periodicity, may be indicative of a wave resonance process taking place along the magnetic field lines connecting the 150 km region to the underlying E-region to the North and South of the geomagnetic equator.

5.1 Observations

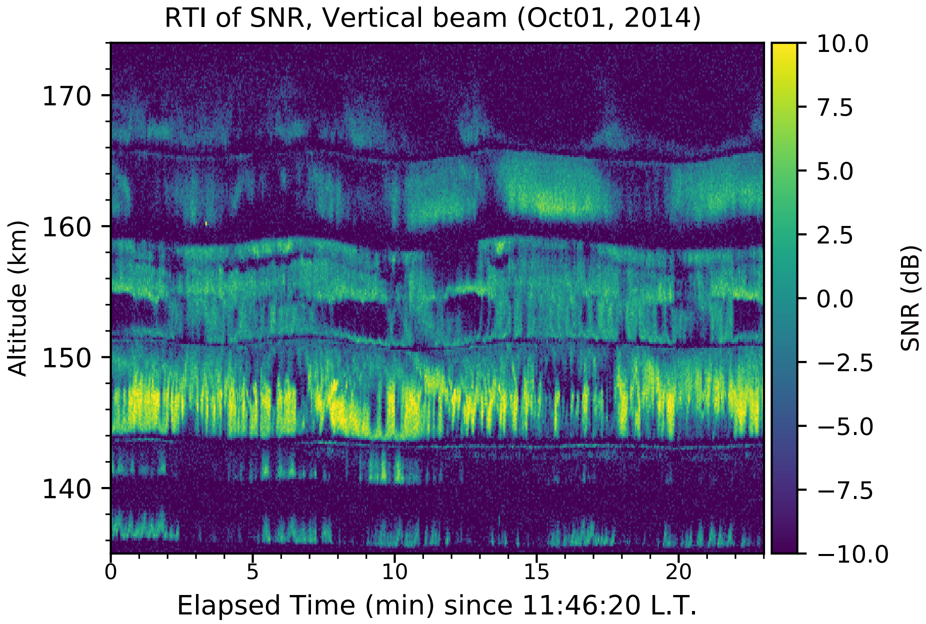

Figure 5.1 – RTI showing SNR of the 3-m Bragg scatter radar power returns taken on January 30, 2016.

Figure 5.1 shows an RTI where the SMQP and the 5-15 min large period oscillations can be seen simultaneously on October 1, 2014. The JRO configuration used was the MST-ISR-EEJ (see section 3.2 for the experiment details). Raw data is collected and backscatter power was estimated with temporal resolutions as short as 0.25 s. This high temporal resolution revealed fluctuations with periods as low as 1 s. For this analysis we have worked with the backscatter power and no spectral estimation in order to achieve as high temporal resolution as possible with enough statistics to characterize the returned signals. In the RTI in Figure 5.1, the 5-15 min oscillations can be recognized as layers of thin undulant sheet-like waves with adjacent “forbidden” or “quiet” zones (zones without detectable backscatter) located around 140,142, 152, 160, and 166 km of altitude. In the same figure the time span is about 23 minutes that roughly fits 3 of these waves, hence the period is about 7 minutes and 40 seconds. Between the layers one can recognize the SMQP as the shorter quasi-periodical vertical structures. We should acknowledge that in this particular case the SMQP filled up almost the entire space between the layers, which is not always the case when observing the occurrence of SMQP on different campaigns.

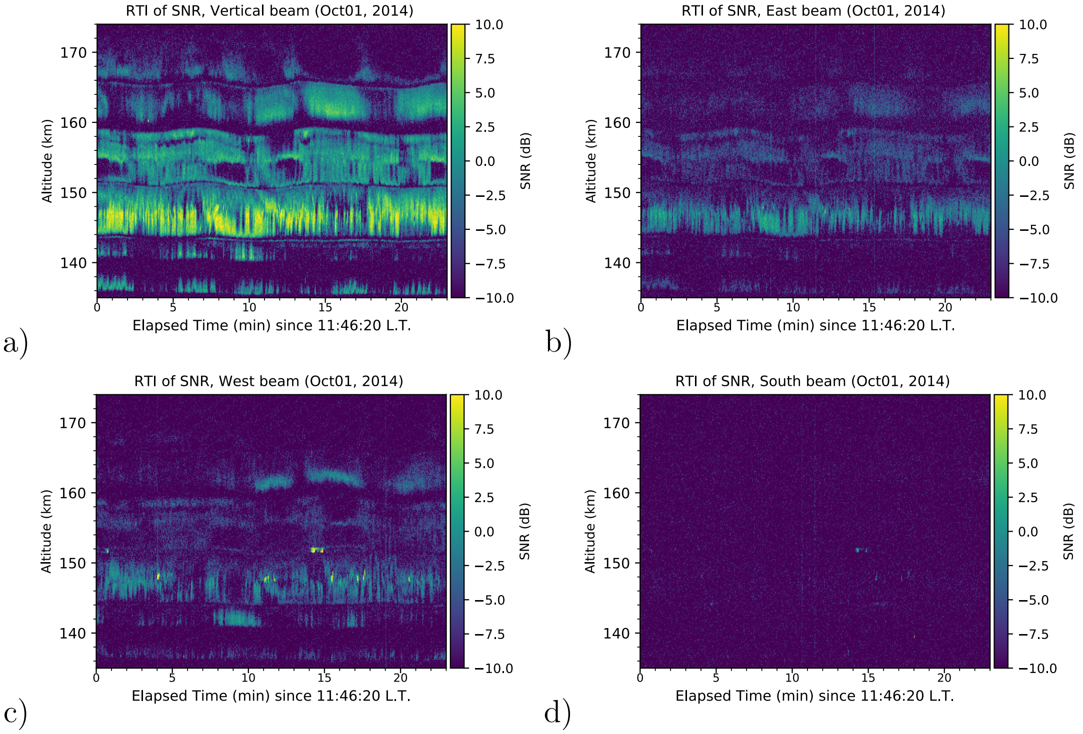

a) b) c) d)

Figure 5.2 – Repeat of Figure 5.1 for the four receiving antennas.

Figure 5.2 is a repeat from Figure 5.1 that shows RTIs from the four antennas. The 2-way radiation patterns for these antennas are depicted in Figure 3.9 (d). Notice that the signal strength detected in these plots scales with spatial extent of the radar field of view in directions perpendicular to the magnetic field lines. Hence, the vertical beam detected the largest signal, while the South beam detected almost no backscattering signal.

Since we are analyzing several MST-ISR-EEJ campaigns, the reader should review section 3.2, where the several parameters associated with each campaign are discussed. The earlier campaigns of 2005 and 2007 (see Table 3.2) that were named MST-ISR (without the EEJ part) used IPPs of 200.1 km (1.334 ms), with a burst of 20 consecutive MST pulses followed by only two ISR pulses of 999 km (6.66 ms). The bursts of 20 MST pulses came every 6000 km (40 ms) and were decoded and coherently integrated in real time. Hence, an integration time of ~ 1 s for the power estimation is achieved after averaging 25 of those 20 coherently integrated pulses. In the more recent MST-ISR-EEJ campaign of January 2016 the IPP used for the MST part was about 375 km (2.5 ms) with a transmitted pulse coded with complementary code of 128 baud with a baud width of 0.15 km (1 μs). The MST part, which consists of ten of those 375 km IPPs pulses transmitted consecutively, is interleaved with the ISR mode and the EEJ mode pulses in such way that the burst of ten consecutive MST pulses is repeated exactly every 18750 km (125 ms). Hence, an integration time of 1 s is achieved by averaging 8 data points of 10 coherently integrated IPPs.

5.1.1 Power estimation

The radar parameters used in MST-ISR-EEJ experiments have changed over the years. Table 3.2 shows a summary of the main parameters used in each campaign for the mesosphere-stratosphere-troposphere (MST) part since year 2005. Figure 3.9 shows the different antenna radar beam 2-way radiation pattern configurations used in all the MST-ISR-EEJ experiments since 2005 until 2016. The horizontal solid and dashed black lines represent the loci of perpendicularity to the geomagnetic **B** field obtained for 100, 300, and 600 km of altitude. The 2015 IGRF model [e.g., *Thébault et al.*, 2015] has been used to obtain the geomagnetic field vector **B** within the antenna beams. The contour line thickness in each of the 2-way radiation patterns is proportional to the antenna gain at the following levels: -1, -3, -6, -9, -12, -15, -18, and -21 dBs from the maximum gain of the particular beam. $\Theta_{x'}$ and $\Theta_{y'}$ are the direction cosines with respect to the plane of the antenna that has been rotated in such a way that the loci of perpendicularity to **B** appear as nearly horizontal contour lines.

5.1.2 Methodology

In an effort to gather information about the location in time and altitude of the occurrence of SMQP fluctuations, an interactive tool was designed to zoom into high time resolution RTIs and manually record those events[1]. Several data sets were inspected using the web-based tool to perform a non-exhaustive search to get an idea how frequently the fluctuations were occurring. We found out that sub-minute fluctuations can be observed in every MST-ISR and MST-ISR-EEJ campaign.

Figure 5.3 shows an example screenshot of the visual interactive tool that was used to zoom into regions of the RTI and record the boundaries of the selected region that showed the SMQP fluctuations. Using this tool, the user visually estimates the number of pulsations seen inside each box, which is then used to determine the period of the pulsations. A variety of pulsation streaks were found, and in order to normalize the measurement every streak was counted as a period. Superposed in this RTI plot, the small rectangles indicate the regions where the SMQP fluctuations have been observed. After selecting a region, the user counts the number of streaks within the rectangle and records the number in the table shown below the RTI; subsequently the program calculates the estimated mean period of the fluctuations. This non-exhaustive search method was applied to the MST-ISR-EEJ database to estimate where the sub-minute fluctuations take place. For future work we are developing digital processing techniques to make the search of SMQP more systematic and to be able to perform a more exhaustive search of the available data. Next, we show some of our findings.

---

[1] The tool is at URL: `http://remote2.ece.illinois.edu/~pablo/150km_short_pulses/RTI_tool_chs_TrueHeight.html`. This tool will be maintained for at least a 3 year period after the submittal of this thesis.

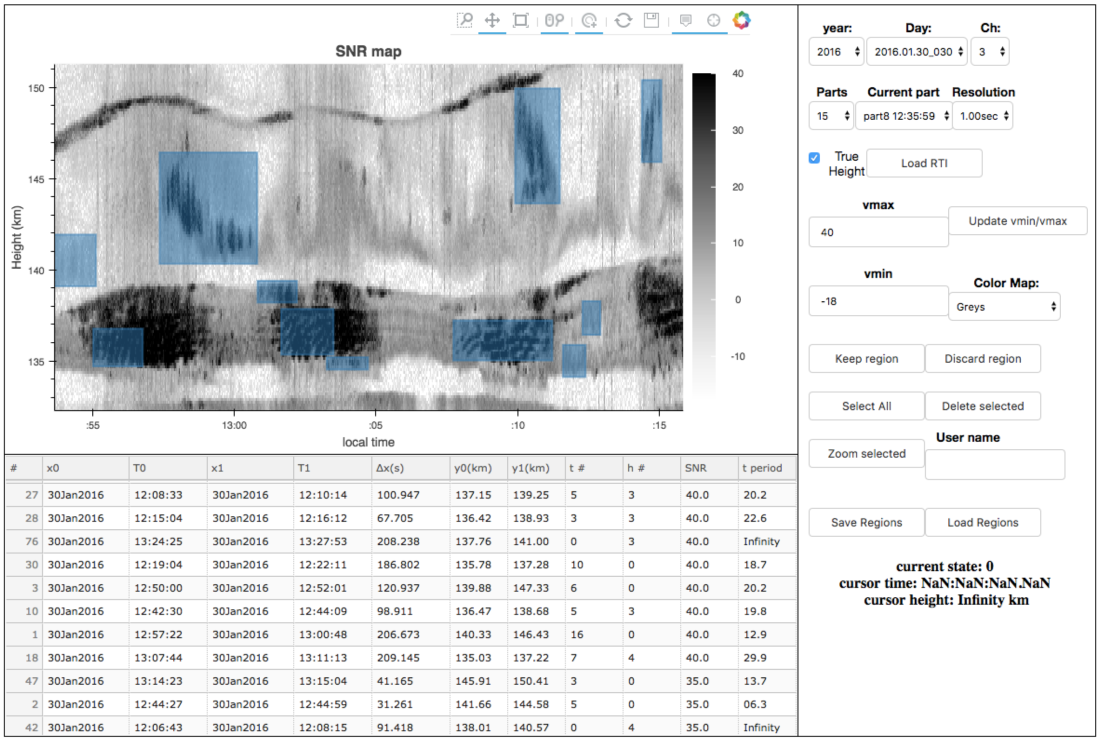

year: 2016
Day: 2016.01.30_030
Ch: 3
Parts: 15
Current part: part8 12:35:59
Resolution: 1.00sec
☑ True Height
vmax: 40
vmin: -18
Color Map: Greys
User name:

current state: 0
cursor time: NaN:NaN:NaN.NaN
cursor height: Infinity km

#	x0	T0	x1	T1	Δx(s)	y0(km)	y1(km)	t #	h #	SNR	t period
27	30Jan2016	12:08:33	30Jan2016	12:10:14	100.947	137.15	139.25	5	3	40.0	20.2
28	30Jan2016	12:15:04	30Jan2016	12:16:12	67.705	136.42	138.93	3	3	40.0	22.6
76	30Jan2016	13:24:25	30Jan2016	13:27:53	208.238	137.76	141.00	0	3	40.0	Infinity
30	30Jan2016	12:19:04	30Jan2016	12:22:11	186.802	135.78	137.28	10	0	40.0	18.7
3	30Jan2016	12:50:00	30Jan2016	12:52:01	120.937	139.88	147.33	6	0	40.0	20.2
10	30Jan2016	12:42:30	30Jan2016	12:44:09	98.911	136.47	138.68	5	3	40.0	19.8
1	30Jan2016	12:57:22	30Jan2016	13:00:48	206.673	140.33	146.43	16	0	40.0	12.9
18	30Jan2016	13:07:44	30Jan2016	13:11:13	209.145	135.03	137.22	7	4	40.0	29.9
47	30Jan2016	13:14:23	30Jan2016	13:15:04	41.165	145.91	150.41	3	0	35.0	13.7
2	30Jan2016	12:44:27	30Jan2016	12:44:59	31.261	141.66	144.58	5	0	35.0	06.3
42	30Jan2016	12:06:43	30Jan2016	12:08:15	91.418	138.01	140.57	0	4	35.0	Infinity

Figure 5.3 – An example screenshot of the visual interactive tool used to register the regions where the SMQP pulsations occur. The shaded rectangles are the regions selected by visual inspection. This example presents data collected on January 30, 2016. The table below is populated each time a new selection box is added and the user manually estimates the number of pulsations within the box.

5.1.3 Sub-minute fluctuations found on day October 1, 2014

A 23 minute RTI of this day was shown in Figure 5.1. On this day the sub-minute fluctuations were almost ubiquitous. That RTI contains 3 periods of the large sheet-like oscillations with a period of 7 minutes and 40 seconds. We can see the SMQP fluctuations filling almost the entire space between the larger period oscillations. The power estimation RTI was obtained with 2 seconds integration time and using the vertical radar beam. The radiation pattern can be seen in Figure 3.9 (d). On this day, the vertical beam had the best perpendicular to **B** pointing direction compared to other campaigns. Figure 5.4 shows a histogram of the periods in seconds encountered on this day; e.g., there were about 32 occurrences of periods between 15 and 17 seconds. Figure 5.5 shows the location of the found SMQP fluctuations. Here we can notice that smaller-period fluctuations on the order of 10-15 seconds tend to be at lower altitudes, while larger periods from 20 to 30 seconds appear at higher altitudes. Some examples of the zoomed in RTIs with periods around 15 seconds can be seen in Figure 5.6

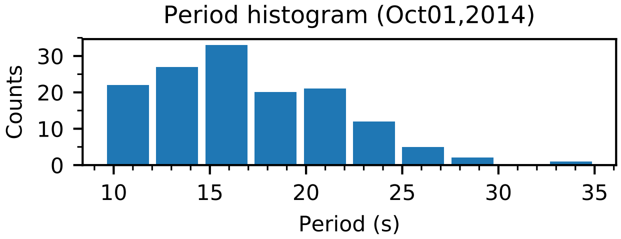

Figure 5.4 – Histogram of the sub-minute periods detected in the 150-km region on October 1, 2014, using a non-exhaustive search method.

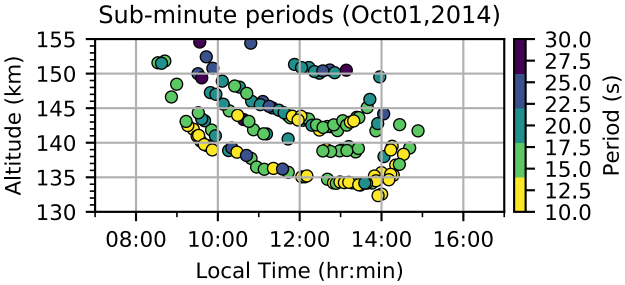

Figure 5.5 – Scatter plot showing the locations in time and altitude and the periods where the short fluctuations have been detected in the 150-km region on October 1, 2014, using a non-exhaustive search method.

5.1.4 Sub-minute fluctuations found on day September 7, 2005

Figure 5.7 shows an RTI plot of SNR of the 3-m Bragg scatter radar power returns obtained with a beam pointing to the west (see the 2-way radiation pattern for this antenna in Figure 3.9 (a)). The non-exhaustive search showed for

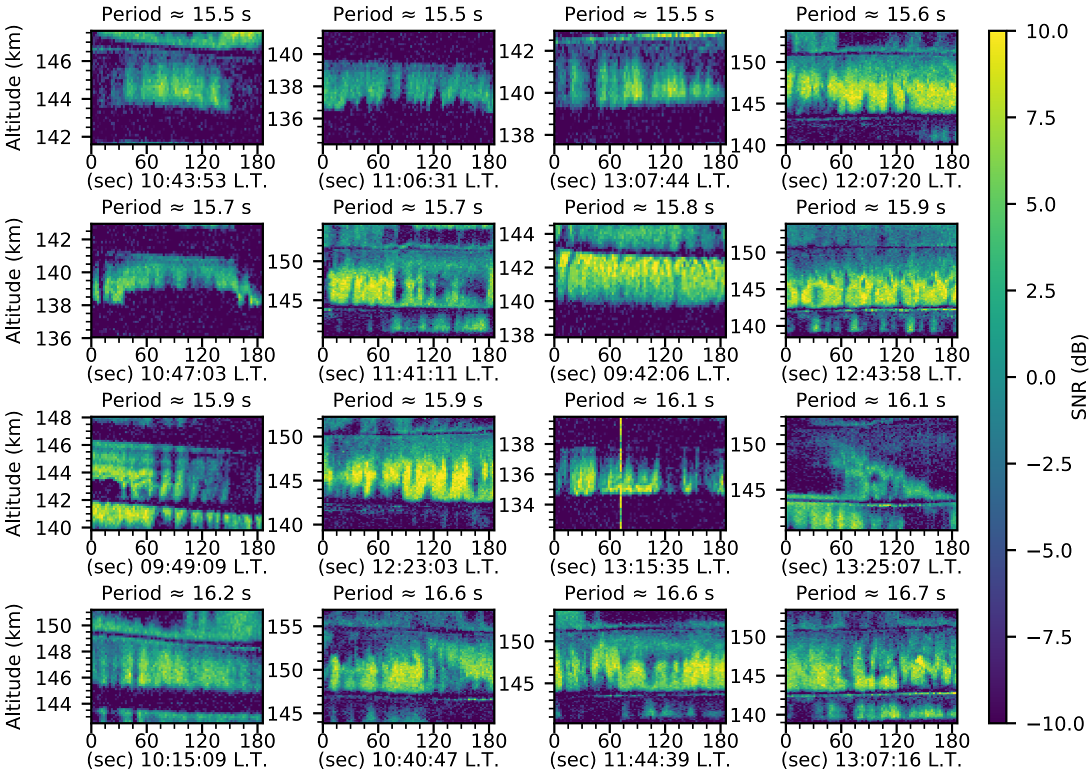

Figure 5.6 – Zoomed in RTIs showing some examples of sub-minute fluctuations in the 150-km region above JRO on October 01, 2014.

September 7, 2005, fewer occurrences of SMQP fluctuations than for Oct 1, 2014, shown before. Figure 5.8 shows a histogram of the periods encountered on this day, while Figure 5.9 is a scatter plot showing the locations in time and altitude where the short pulsations were detected. Figure 5.10 shows examples of the zoomed in RTIs of the few SMQP encountered this day. This particular day was one of the cases studied by *Reyes* [2012] for solar flare effects on the Jicamarca data due to an X17.1 solar flare event that hit Earth around 12:30 local time.

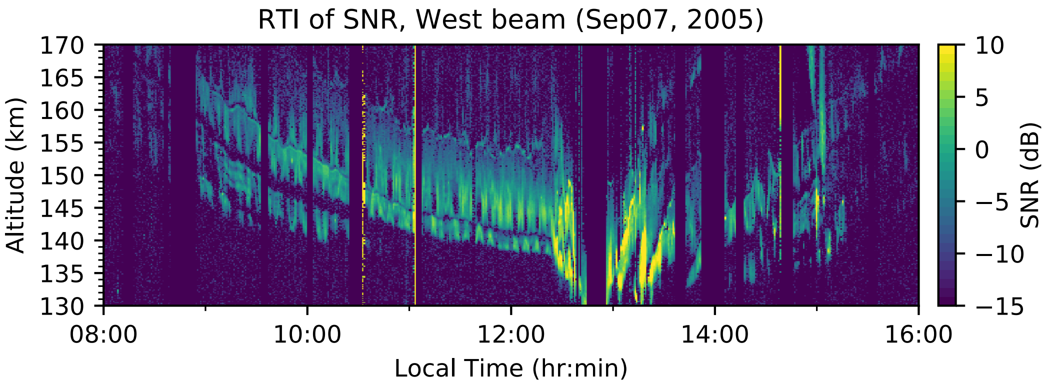

Figure 5.7 – RTI showing a daytime SNR of 150-km echoes of the MST-ISR-EEJ experiment obtained on September 7, 2005.

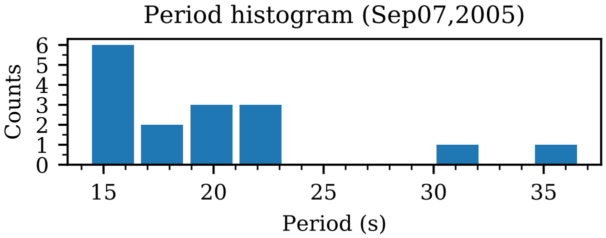

Figure 5.8 – Histogram of the sub-minute periods detected in the 150-km region on September 7, 2005, using a non-exhaustive search method.

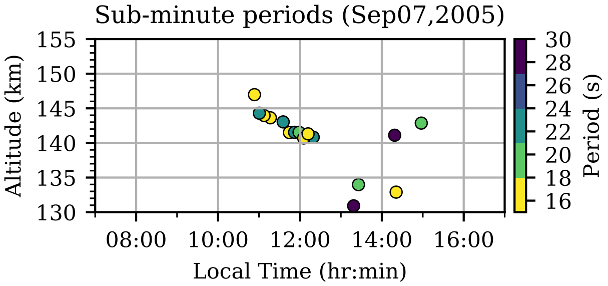

Figure 5.9 – Scatter plot showing the locations in time and altitude and the periods where the short fluctuations have been detected in the 150-km region on September 7, 2005, using a non-exhaustive search method.

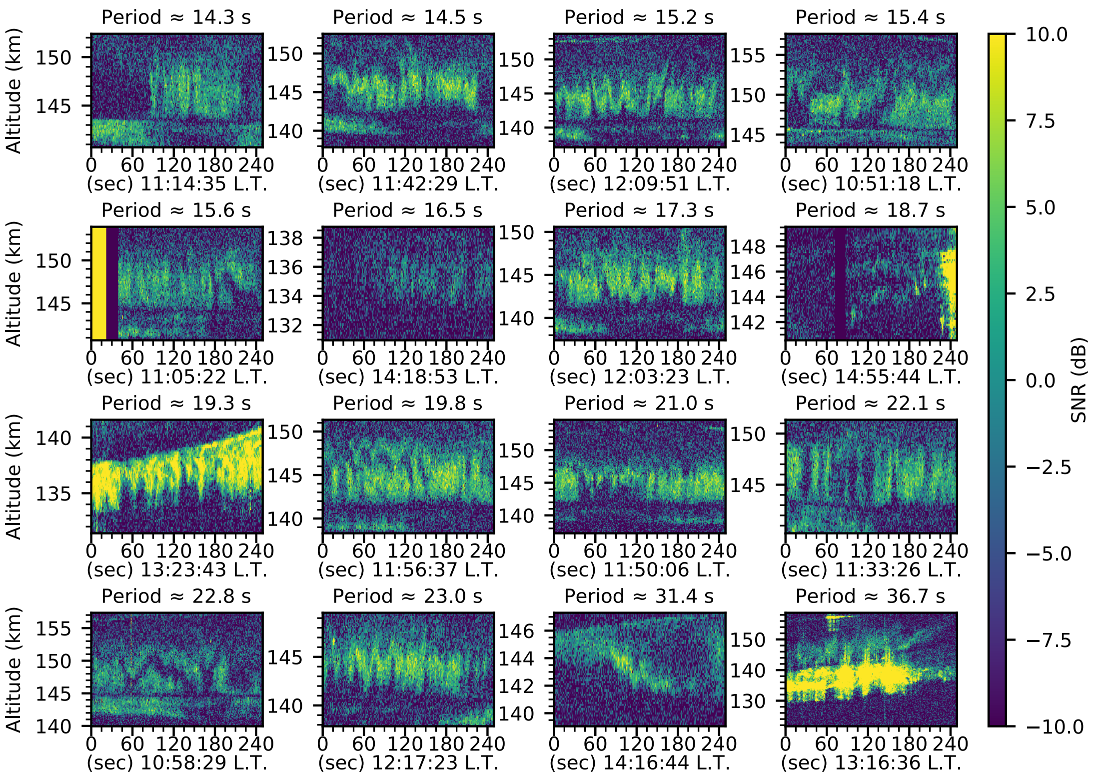
Period ≈ 14.3 s
Period ≈ 14.5 s
Period ≈ 15.2 s
Period ≈ 15.4 s
Period ≈ 15.6 s
Period ≈ 16.5 s
Period ≈ 17.3 s
Period ≈ 18.7 s
Period ≈ 19.3 s
Period ≈ 19.8 s
Period ≈ 21.0 s
Period ≈ 22.1 s
Period ≈ 22.8 s
Period ≈ 23.0 s
Period ≈ 31.4 s
Period ≈ 36.7 s

Figure 5.10 – Zoomed in RTIs showing some examples of sub-minute fluctuations in the 150-km region above JRO on September 7, 2005.

5.1.5 Sub-minute fluctuations on January 30, 2016

Figure 5.11 shows a range-time-intensity (RTI) plot of signal-to-noise (SNR) of the 3-m Bragg scatter radar power returns obtained with a beam pointing toward the zenith (vertical) direction. The radiation pattern for this experiment can be seen in Figure 3.9 (f) during a MST-ISR-EEJ experiment on January 30, 2016.

The non-exhaustive search for this day showed a predominance of pulsations in the 15 to 20 seconds range. Figure 5.12 shows a histogram of the periods encountered on this day, while Figure 5.13 is a scatter plot showing the locations in time and altitude where the short pulsations were detected.

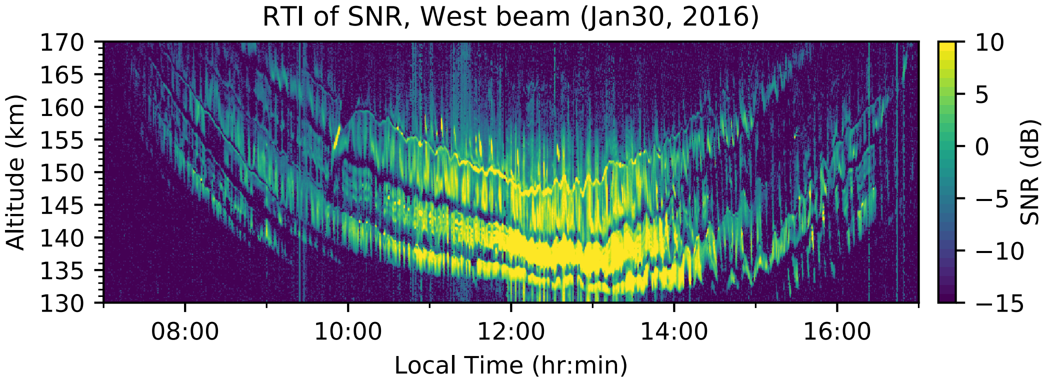

Figure 5.11 – Range-time-intensity (RTI) plot of signal-to-noise (SNR) for the vertical beam of the MST-ISR-EEJ experiment obtained on January 30, 2016.

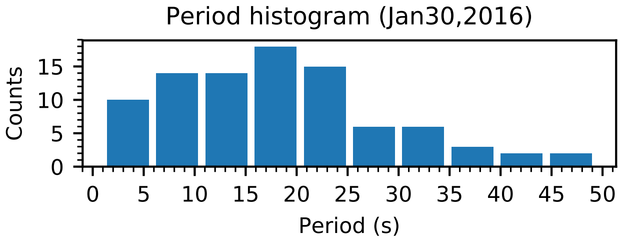

Figure 5.12 – Histogram of the sub-minute periods detected in the 150-km region on January 30, 2016, using a non-exhaustive search method.

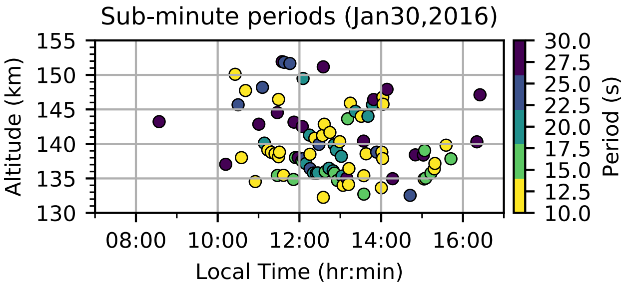

Figure 5.13 – Scatter plot showing the locations in time and altitude and the periods where the short fluctuations have been detected in the 150-km region on January 30, 2016, using a non-exhaustive search method.

To show evidence of the different instances of fluctuations found in the 150 km region, samples of zoomed in RTIs are presented in Figure 5.14. The sample includes 12 RTIs of the regions where sub-minute fluctuations have been detected spanning from a few seconds up to around 20 seconds. Each subplot has a title

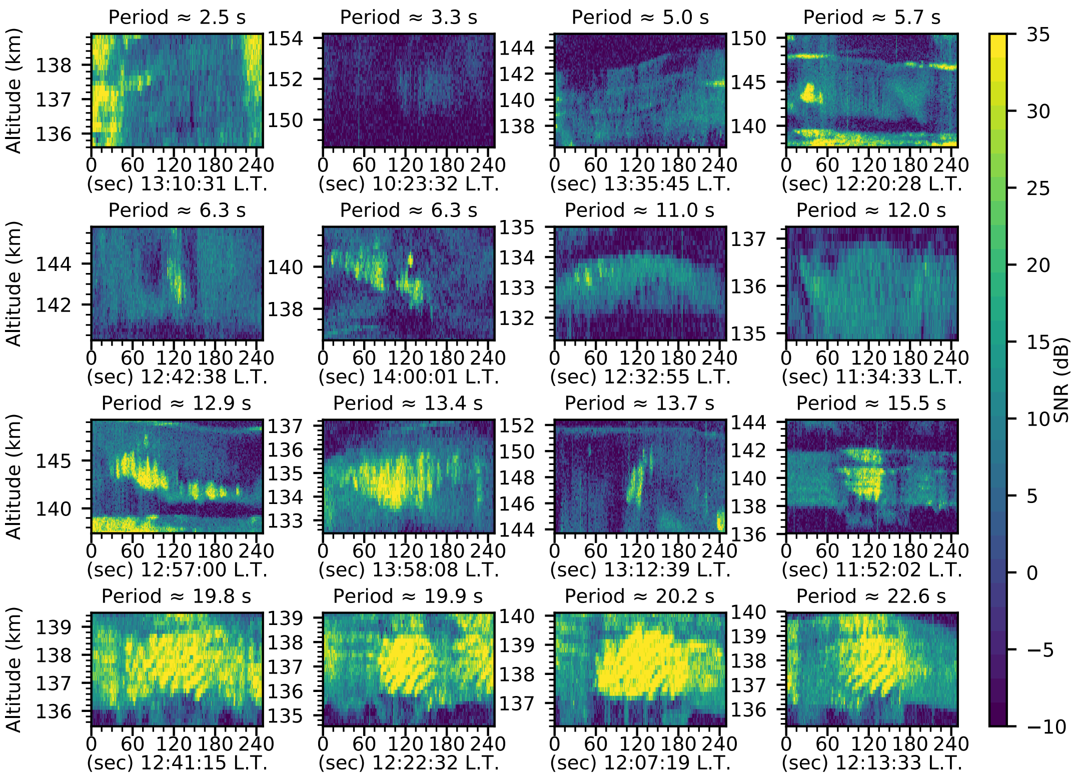

Figure 5.14 – Zoomed in RTIs showing some examples of sub-minute fluctuations in the 150-km region above JRO on January 30, 2016. Notice that in the bottom row of plots, we are showing SMQPs that are tilted. We are going to discuss those in subsection 5.14.

indicating the estimated period of the fluctuations. The same color scale has been used for comparison of the SNR levels.

Tilted SMQP

In Figure 5.14 we show examples of a different type of SMQP that we have identified as tilted SMQPs. While other SMQP are very slightly tilted and mostly vertical, the tilted SMQPs show about 20 seconds of periodicity horizontally and 1 km periodicity vertically. These values of very small vertical wavelength and intrinsic frequency of 20 seconds are way outside the conditions needed for internal gravity waves. Also, the tilted SMQPs show a surprising characteristic: They exhibit upward phase progressions, which in the analogy of a gravity wave would indicate that the energy carried by the wave is moving downwards. Another characteristic is that the tilted SMQPs are 20 dB stronger than the regular SMQP.

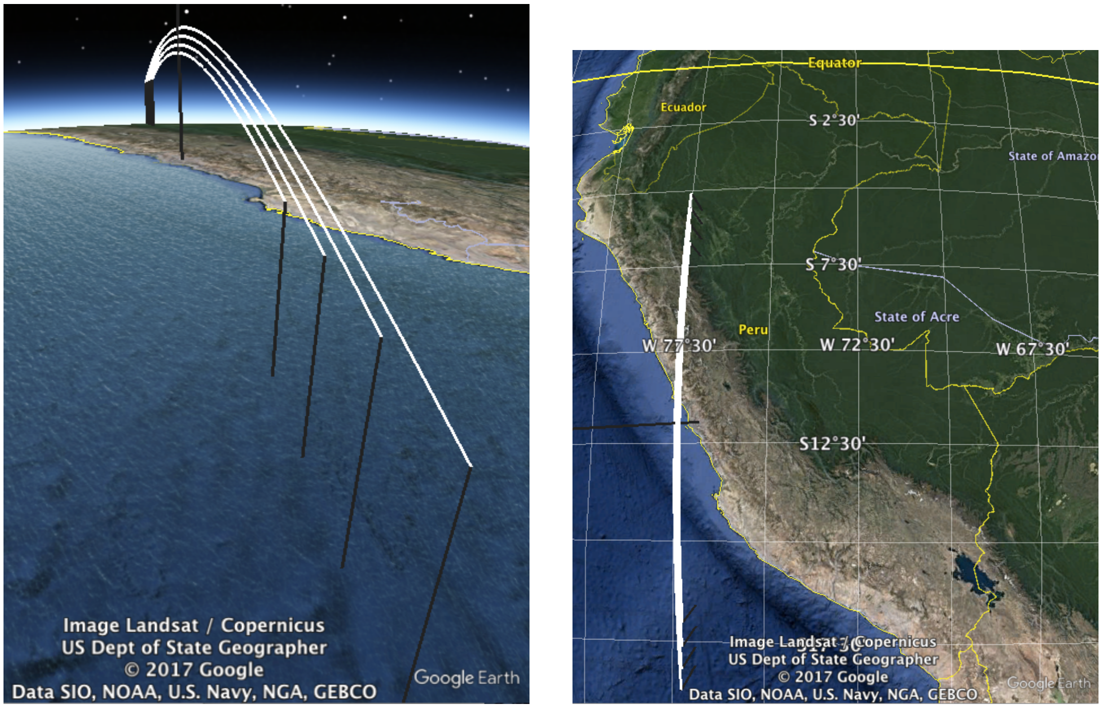

Figure 5.15 – Google Earth screenshots of the equatorial 150 km region with magnetic field lines connecting altitudes of 140 km, 150 km, 160 km, and 170 km from the geomagnetic equator through magnetic field lines to the 100 km altitude E-regions, located to the North and South. Notice that the TL longitudes range from about -17.5 degrees South to -7.5 degrees South.

5.1.6 Cavity resonator along the magnetic field lines

Here we will present a possible mechanism that may explain the observed sub-minute fluctuations in the 150-km region. Let us consider a transmission line (TL) analogy for magnetic field lines **B** crossing the 150 km region above JRO and terminated at E-region heights to the North and South of the magnetic equator. In one such transmission line segment we would expect to observe resonant modes of oscillations corresponding to North and South propagating trapped waves. To have an idea of the dimensions of the transmission line, we show in Figure 5.15 Google Earth screenshots of lines connecting JRO altitudes of 140 km, 150 km, 160 km, and 170 km through magnetic field lines that end at 100 km altitude to the North and to the South of the magnetic equator. The data used for this figure was obtained using the IGRF model for October 01, 2014. Consider next low frequency electromagnetic waves guided by field lines in the magnetized plasma of the region propagating at the local Alfvén speed [e.g. *Kelley*, 2009]

$$v_{ph} = \frac{B}{\sqrt{\mu_0 n_i M_i}}, \tag{5.1}$$

where B is the magnetic flux density, μ_0 is the permeability of free space, n_i is the ion density, and M_i is the ion mass. This formula is valid in magnetized plasmas for waves with frequencies satisfying $\omega \ll \Omega_i$, where $\Omega_i = qB/M_i$ is the ion gyro frequency. Since the frequencies that we observed in our pulsations were in the order of fractions of Hz, while the gyro frequency at the valley region is about 20 Hz, the condition $\omega \ll \Omega_i$ is well satisfied.

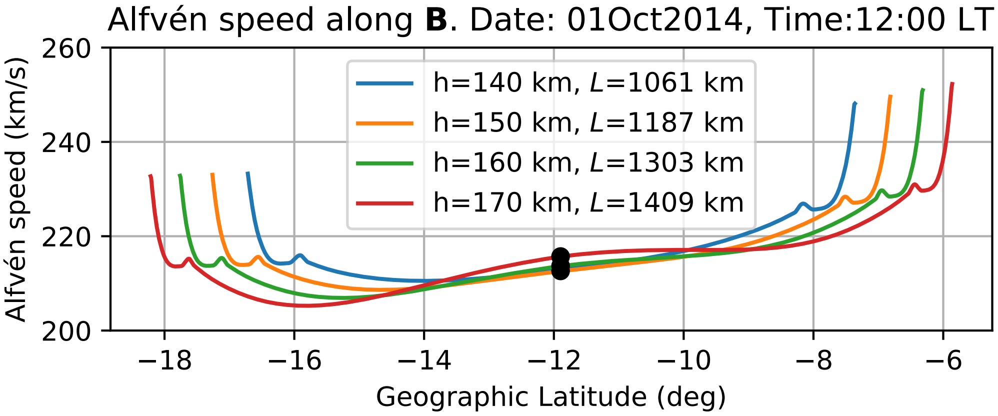

Figure 5.16 – Alfvén speed along magnetic field lines connecting the equatorial valley region to the North and South at 100 km of altitude. The black dots correspond to the location of JRO. The legend displays the total distance, L, and the altitude, h, where the corresponding magnetic field lines cross above JRO. The data for this plot was obtained using the IRI model for the ion composition (NO+, O_2+, O+), and the IGRF model for the magnetic field. The date and time was set up for October 01, 2014, at local noon.

In Figure 5.16 we plot the Alfvén speed computed using equation (5.1) along the magnetic field lines depicted in Figure 5.15. Starting at the altitudes of 140 km, 150 km, 160 km, and 170 km along the zenith above JRO, the magnetic field lines were followed until reaching 100 km of altitude to the North and to the South. Notice in Figure 5.16 that close to both ends, the wave speed increases smoothly, then it experiences a small but abrupt decrease and finally increases again. The abrupt change is due to the sharp increase in ion density at the top of the E-region, and we are going to assume that the waves get reflected at those locations. Now that the end points are identified we can calculate the length of the TL and the time it takes for the waves to propagate from end to end by integrating $dt = dx/v_{ph}$ along the lines. With the total time and distance we obtain an effective wave speed:

$$v_w = \frac{\text{Total distance}(L)}{\text{Total time}} = \frac{\int dx}{\int (1/v_{ph}) dx}. \tag{5.2}$$

Finally, in order to find the wave frequency and wavelength we use the formula for periodic oscillations in lossless transmission lines shorted at both the ends:

$$\lambda_w = \frac{v_w}{f} = \frac{v_w}{1/T} = \frac{2L}{n}, \tag{5.3}$$

where v_w is the wave velocity, f the wave frequency, $T = 1/f$ the wave period , L the length of the TL, and n the standing wave mode that we let be 1. With (5.3) we can calculate the wave period T of the normal mode of the cavity resonator and the results are shown for different days and hours in Figures 5.17, 5.18, 5.19, and 5.20. In these figures the transmission lines have been terminated at the top of the E-region, and the calculated effective wave speed, v_w, and the period of the standing waves, T, are indicated in the legend of each plot.

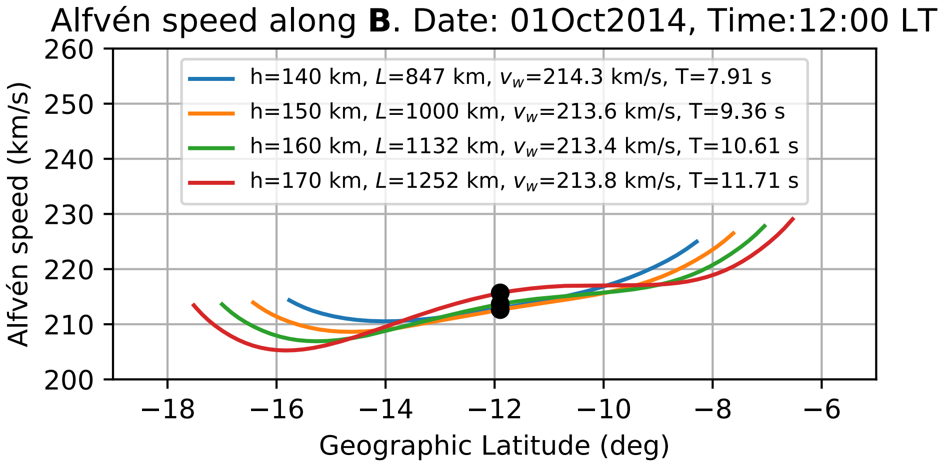

Figure 5.17 – Similar to Figure 5.16 but ending the lines at the top of the E-region, right before the abrupt change in Alfvén speed.

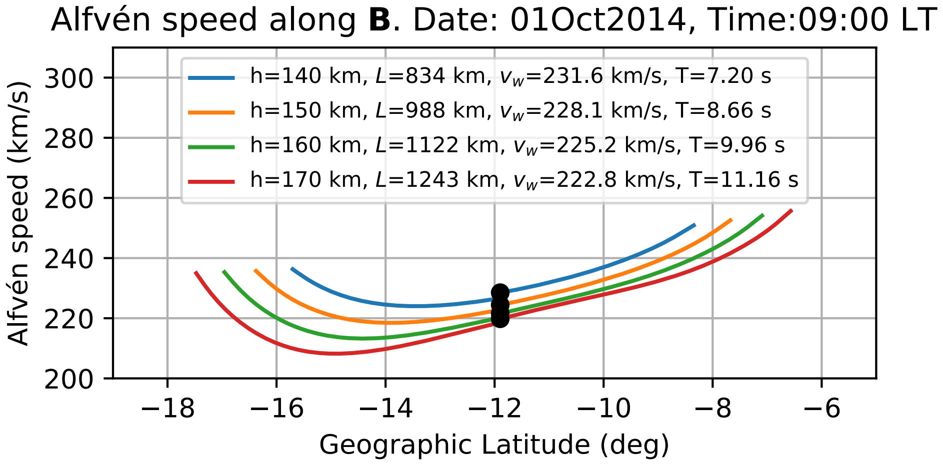

Figure 5.18 – Repeat of Figure 5.17 but for 9:00 local time conditions.

Figure 5.18 was obtained for October 1, 2014, at 9:00 a.m., when the ionization was lower. Notice that the periods do not change too much, and they remain in the range from 7 to 11 seconds. Figure 5.19 shows the TL calculations for January 30, 2016. Notice that this day, at noon, the effective Alfvén speed was slightly larger than in October 2014, but the periods remain in the range from 7 to 11 seconds. Finally in Figure 5.20 we display the TL calculations for September 07, 2005. On this day, the periods were also in the range from 7 to 11 seconds. We observe that overall the periods found using the model of periodic standing waves with low frequency electromagnetic waves traveling at the Alfvén speed are in the range of the SMQP periods that we find in the data.

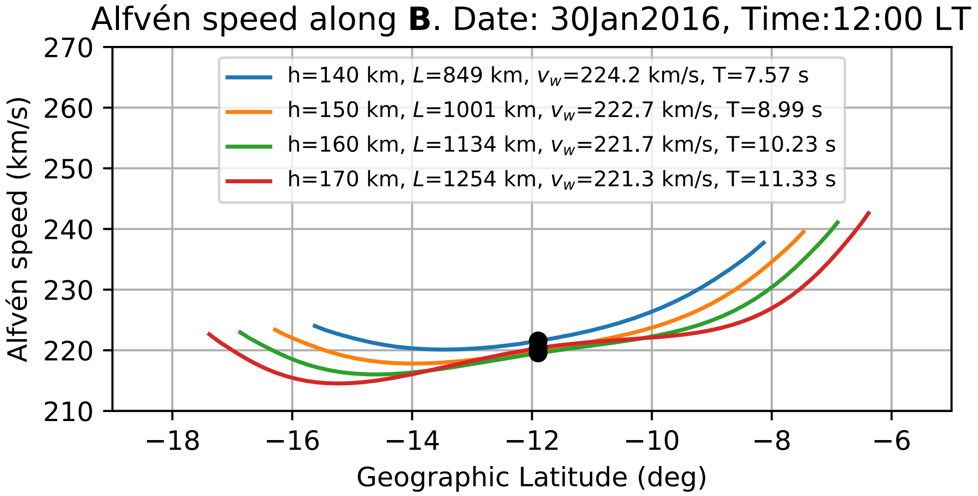

Figure 5.19 – Repeat of Figure 5.17 for January 30, 2016, at local noon.

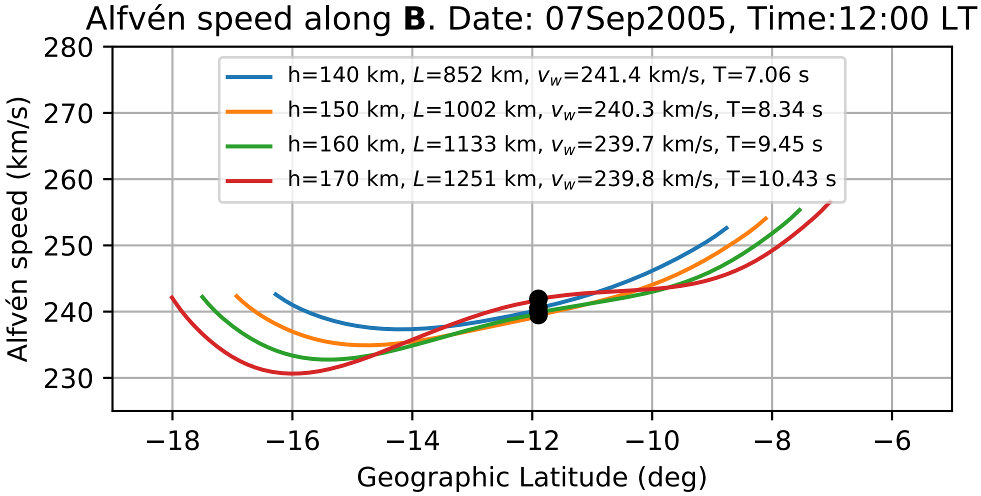

Figure 5.20 – Repeat of Figure 5.17 for September 07, 2005, at local noon.

5.2 Discussion

In this chapter, we have shown evidence of SMQP fluctuations found in the JRO 150-km echoes. In section 5.1.6 we explored the possibility of waves oscillating in the TL resonator formed by the geomagnetic field lines connecting the geomagnetic equator 150 km region with the top of the E-region to the North and South. The close coincidence of the periods found in the data with those predicted by the TL hypothesis suggests that electromagnetic waves, traveling at the Alfvén speed, could have an effect in the enhancements seen in the SMQP fluctuations. The resonant modes in the cavity need an energy source that can trigger the resonant modes, and that could be the internal gravity waves that cross the valley region and that we have studied in Chapter 4. As for the relevance that the SMQP could have in enhancing the meter-scale radar backscatter signal at the 150-km region in the equatorial ionosphere, we will speculate that the energy in the resonant waves of a cavity formed by the field lines connecting the off-equator E-regions to the 150 km region could be a feeding mechanism of the amplification of thermally driven electron density irregularities in the region, causing the radar scattering cross section at VHF to be enhanced above the thermal equilibrium incoherent scatter levels.

5.2.1 Possible biases in the estimation of SMQP periods

The non-exhaustive visual search method undoubtedly carries some possible biases subject to errors by the user of the web tool; e.g., the periods registered by the user could be slightly off or up to twice or half-as-large as the real periods depending on whether echoes are enhanced once or twice per period of the driver waves causing the enhancements. As a general rule, we have counted all the streaks inside each region. Histograms could also be biased, in the sense that some period estimations were taken using only a fraction of a whole patch of SMQP fluctuations. A future direction to overcome this difficulty is to perform a Fourier analysis to search for peaks in the power spectra and perform a comprehensive search in the MST-ISR-EEJ database, similar to the spectral analysis done in

Chapter 4 with the 150-km 5-15 minute fluctuations, depicted in Figure 4.6. Nevertheless, the method used in this study was enough to detect the SMQP, report their existence and characterize the occurrence rate.

5.2.2 Predominance of SMQP in directions perp to B

The data taken on October 1, 2014, using the vertical beam, was one of the richest data sets in the sense of occurrences of SMQP. We could explain this by looking at the radar beam that was used: The 2-way radar beam pattern of the vertical beam used for this campaign is shown in Figure 3.9 (d). We can notice that the vertical beam is elongated along the locus of perpendicularity to **B** around 150 km of altitude. This means that data obtained with this antenna collected mostly radar backscattering coming from the directions perpendicular to the magnetic field lines. In fact, comparing with beam patterns from other campaigns, October 2014 was the MST-ISR campaign with a beam collecting the most perpendicular to **B** echoes. Another interesting fact of the October 2014 campaign is that the geomagnetic equator, moving in time through the years, happened to cross exactly over JRO around years 2014/2015. Probing the valley region right at the magnetic equator, like in October 2014, meant that the radar was probing the transmission line right at the center of it. Needless to say, the center of a transmission line is where the peak of the oscillation can be found.

In view of the above discussion, the reader might conclude that SMQP fluctuations are field aligned irregularities (FAI) that are only detected perpendicular to **B**. In fact many of the signals detected by the South beam, the one that looks the farthest away from perpendicular to **B**, came from cross-talk with the other beams or from signal detected through coincident sidelobes. *Chau and Kudeki* [2013] found that the majority of the 150-km echoes at Jicamarca are from naturally enhanced incoherent scatter (NEIS), but in order to find NEIS longer integration times (e.g. 1 to 5 minutes) are needed, which in turn makes it impossible to detect SMQP fluctuations. Therefore, due to our short integration times, we cannot discount the possibility that SMQPs could be inherent in NEIS echoes too.

CHAPTER 6

CONCLUSIONS AND FUTURE DIRECTIONS

The equatorial valley region has been studied with two instruments: the Jicamarca ISR and the VIPIR ionosonde. The main conclusions drawn from the studies described in this work can be summarized as follows:

1. The quiet stratified electron density contours are being rippled by gravity waves propagating through the ionosphere. Evidence for this is the variation of AOA and of virtual reflection height in the ionosonde data with downward phase progression as depicted in Figure 4.11 for virtual height and in Figure 3.27 for AOA. As seen by the comparisons of VIPIR data with the 50 MHz radar data, the waves that are rippling the ionosphere are evidently of the same scale as the fluctuations of the "forbidden" or "quiet" zone thin layers of the 50 MHz 150-km echo fluctuations. Consequently, any theory aimed to explain the generation of the 150-km echoes, with its enhanced and "forbidden" zones and their undulations, needs to include the gravity wave as one of its inputs.

2. Plasma drift fluctuations from 50 MHz 150-km echoes are small compared with the overall plasma drift and that might be the reason they were not resolved or ignored in previous studies. We compared them with 150-km echo displacements and we found that both plasma drift fluctuations and

displacements have similar periods of oscillation. The oscillation phases, though do not seem to agree all the time, and that is maybe just a consequence of the propagation direction of gravity waves. We can conceive that in certain propagation directions of the gravity waves the velocities that are induced are in phase with the displacements, while in other propagation directions the drift fluctuations are not in phase. Usually the E-region through currents along magnetic field lines acts as an effective short for gravity-wave induced electric fields. However, we are noticing here a residual, which indicates that shorting, although efficient, is not perfect.

3. From the phase profiles of the cross-correlation of cross-polarized antennas in the Valley experiment (see Figure 3.2), we observe that incoherent scatter Faraday rotation exhibits a smooth progression with altitude. We conclude that there is no indication of sharp density gradients from the IS measurements. Still, there is evidence for longer scale spatial variation of electron density in the region that can cause field aligned currents upon polarization that could be modulating the enhancement mechanism operating in the region.

4. The sub-minute quasi-periodic fluctuations (SMQP) seen in the range-time-power maps of 150-km echoes could be normal modes of the field line coupled system excited by the energy sources driving the 150-km echoes. We tested our hypothesis that electromagnetic waves traveling at the Alfvén speed in the wave guide formed along magnetic field lines connecting the Valley region with the E-region would generate standing waves with periods of about 10 seconds. These periods are of the same order found in the data. Therefore, we think that there is strong evidence that the SMQP fluctuations can be manifestations of waves resonating in the cavity formed

by the magnetic field lines and the E-region. The energy needed to support the resonant waves generating the SMQPs might well be coming from the gravity waves that constantly cross the valley region.

5. An interesting new observation is that of the tilted SMQP echoes that show upward phase progression. In an analogy to gravity waves, upward phase progression would indicate energy flowing downwards for the tilted SMQPs, but these waves have periods and vertical wavelengths too short to be gravity waves.

6.1 Future Directions

While plasma physics simulations have made progress toward explaining the enhancement mechanism of the 150-km echoes [e.g . *Oppenheim and Dimant*, 2016], the questions remain: What is the mechanism of suppression of the echoes? What causes the intricate shape of "forbidden" and enhanced zones? We reiterate that a theory capable of explaining the generation of the 150-km echoes, one that captures the necklace shape together with its enhancements and its "forbidden" or "quiet" zones, should include the effect of the waves crossing the valley region, i.e. the gravity waves, and maybe the SMQP fluctuations. The waves that generate the SMQPs could drive field aligned currents that should be included in conjunction with the theory of photoelectron induced IS enhancements to better capture the physics of the valley region.

Based on our experimental perspective gained and the evidence presented in this thesis, we can make the following suggestions for designing new experiments and developing better processing techniques in order to better understand the equatorial valley region physics:

1. Joint JRO/VIPIR observations of the equatorial E-F valley region should

continue to be scheduled while better processing techniques should be developed in order to jointly invert for electron density profiles. The Valley experiment should be given particular emphasis since this mode is capable of resolving a wider power spectrum bandwidth. Perhaps a new dedicated experiment should be designed that combines the high spatial resolution capabilities of the MST mode with the high Doppler spectral resolution from the Valley experiment.

2. *Reyes* [2012] described the impact of solar flares on the strength, location, shape, and spectrum of the 150-km echoes in a series of events during the 2005 and 2006 MST-ISR campaigns. This supports the analysis by *Oppenheim and Dimant* [e.g. 2016] on the importance of photoionization as an enhancer of the plasma waves. Still, during these events, the different layers that form the 150-km necklace seem to maintain their continuity, with the exception that the layers seem to be squeezed closer and pushed down in altitude as if they were trapped in magnetic flux tubes that came closer together probably due to the increased currents in the E-region. Theory of photoionization on its own will not be able to capture the full physics, unless it also inputs the waves and field aligned currents in the region.

3. With the existing MST-ISR-EEJ database, a more comprehensive characterization of the sub-minute fluctuations should be performed. Signal processing techniques should be developed that completely characterize the SMQP fluctuations. Spectrograms like the one in Figure 4.6 could be applied for this purpose.

APPENDIX A

ALGORITHM FOR DETECTING THE VIRTUAL REFLECTION HEIGHTS FROM VIPIR IONOGRAMS

The detection algorithm that gets the virtual reflection heights from O-mode traces of the VIPIR ionograms can be described in the following steps:

1. Separation of O- and X- modes
2. Detection of portions of the O-trace with the largest reflecting power
3. Filling the gaps by following the most likely local maximum between each pair of adjacent traces.

The separation of O-mode and X-modes is done by combining the orthogonal antennas 1 and 2 (see Figure 3.18 for their location). Each antenna, polarized in the N-W or the N-E direction, receives reflected signals from both modes of propagation by adding and subtracting the signals of the two orthogonal antennas. One gets the polarization in the N-S direction (O-mode) with the sum and in the E-W direction with the difference. This process does not completely clean each of the modes, which leads to imperfections in the detection algorithm described above. After visual inspection of the resulting O-traces, one can manually revise the ionogram trace and proceed with the manual detection that we describe next.

For the manual detection of the virtual heights, ionogram figures of 6 x 4 inches with 300 pixels per inch were recorded superposed with the traces detected by the algorithm using a thin black line on top of the ionogram. The figure axes are also marked with a red rectangle to serve as a reference at the time of using a program for reading the marked figures. Figure A.1 is an example of this type of figure.

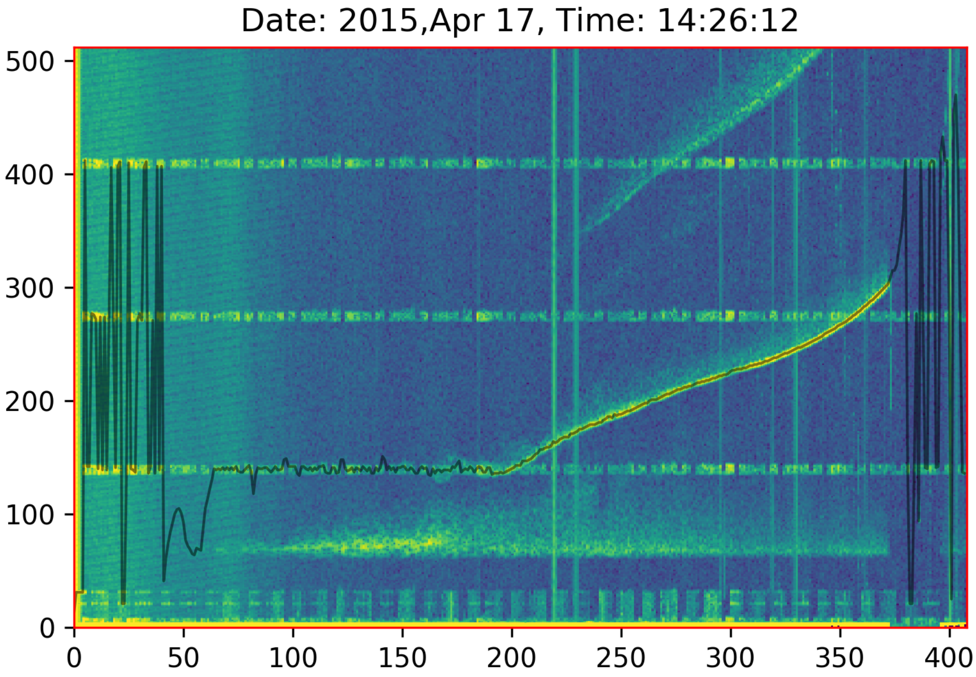

Figure A.1 – VIPIR ionogram with the output of the O-trace detecting algorithm superposed as a thin black line.

The next step is to use a graphics software in order to superimpose a red line path on top of the O-trace. The result of this is shown in Figure A.2. In this particular ionogram there was also a malfunction, manifested in frequency indexes from about 375 to 400, where no transmitted pulses were launched, possibly due to a system protection against large VSWR. Another challenge is the presence of the VHF pulse from the JRO system in the MST-ISR-EEJ mode that contaminates the VIPIR data due to the vicinity of their antennas. Finally a simple code in Python was developed to read the pixel information of the figure and extract the location of the pixels painted in red.

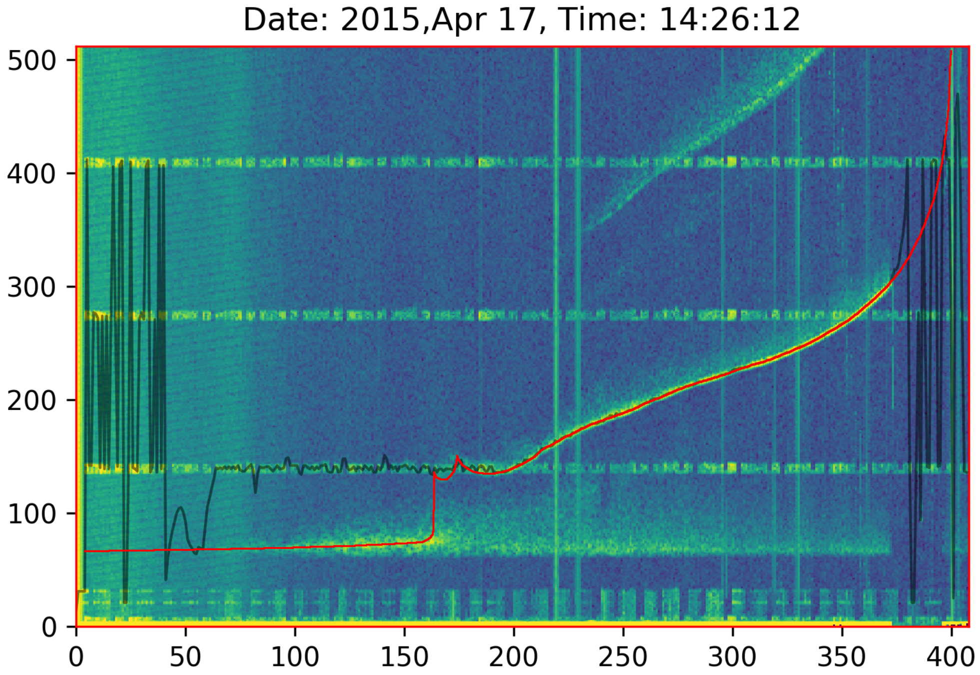

Figure A.2 – VIPIR ionogram showing the manually detected O-trace for the same ionogram shown in Figure A.1.

While the manual method is not perfect either since it includes the human detection uncertainties and is a long process even for a trained user, it is still preferred in certain places where a good quality of O-traces is needed, e.g. in the VIPIR figures from Chapter 4.

For future directions in the detection of O-traces, a detection that uses both VIPIR and JRO incoherent scatter information should be created that will improve the overall remote sensing of the equatorial ionosphere.

APPENDIX B

JRO SYSTEM CONFIGURATION DOCUMENTS

When an experiment is configured at JRO, a couple of documents are provided to the user: the switchyard transmitter and receiver connections including hybrid combiners (Figure B.1, B.2, and B.3), and the phasing of all the 128 modules including the orthogonal up and down polarizations, and extra phasing arrangements (Figure B.4, B.5, and B.6). Using those documents one can determine the radiation beam pattern of the antennas used, the transmitted and received polarization of the backscatter signals, and the acquisition system channels used in reception. In this appendix we provide these documents as received from the JRO staff. For understanding key characteristics of the 50 MHz main dipole array at JRO, the reader is referred to the *Ochs* [1965] manual.

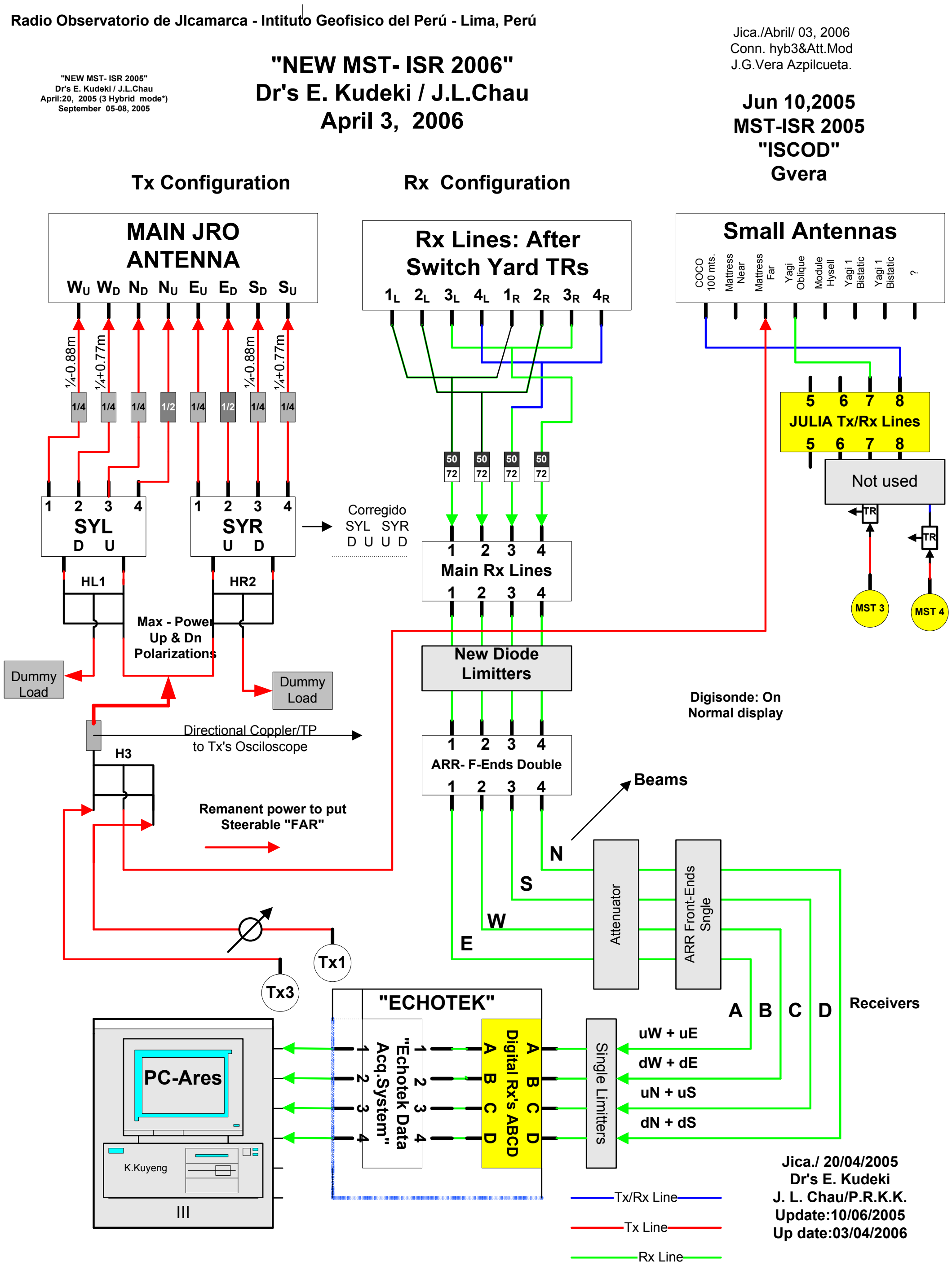

Figure B.1 – Switchyard configuration for MST-ISR experiment for years 2005, 2006, and 2007.

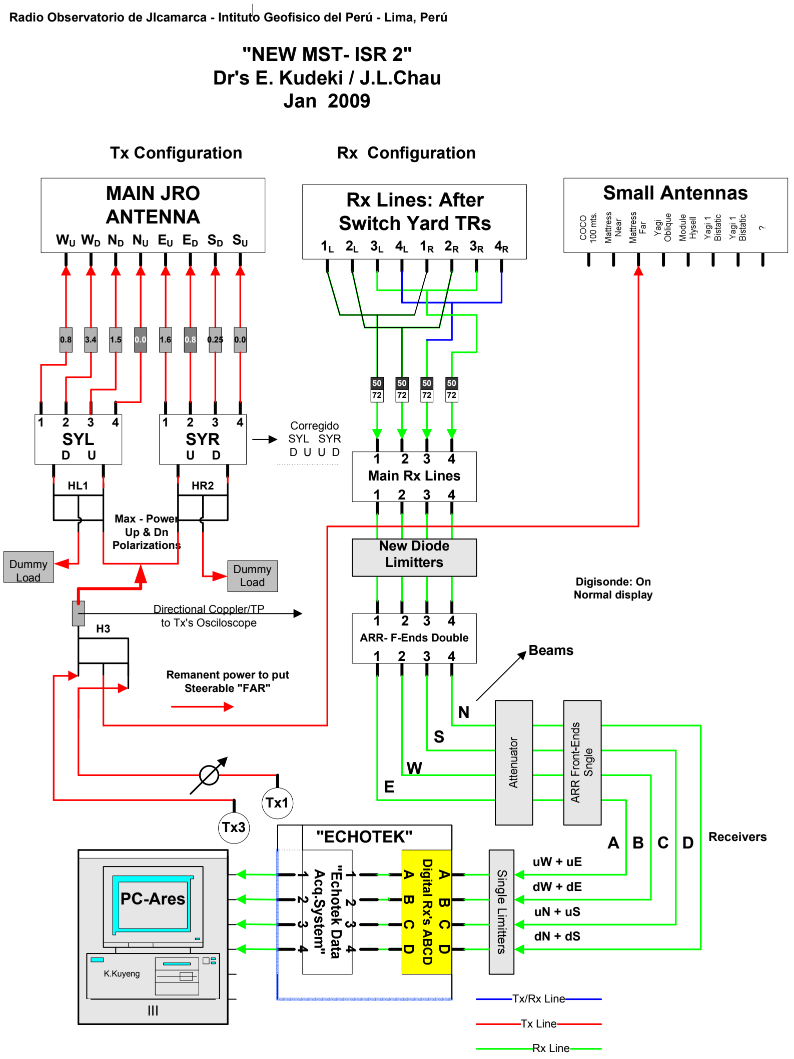

Figure B.2 – Switchyard configuration for MST-ISR experiment for year 2009.

Manual de experimento MST-ISR-EEJ (21 -31 Enero , 2016)

1. Configuración switchyard

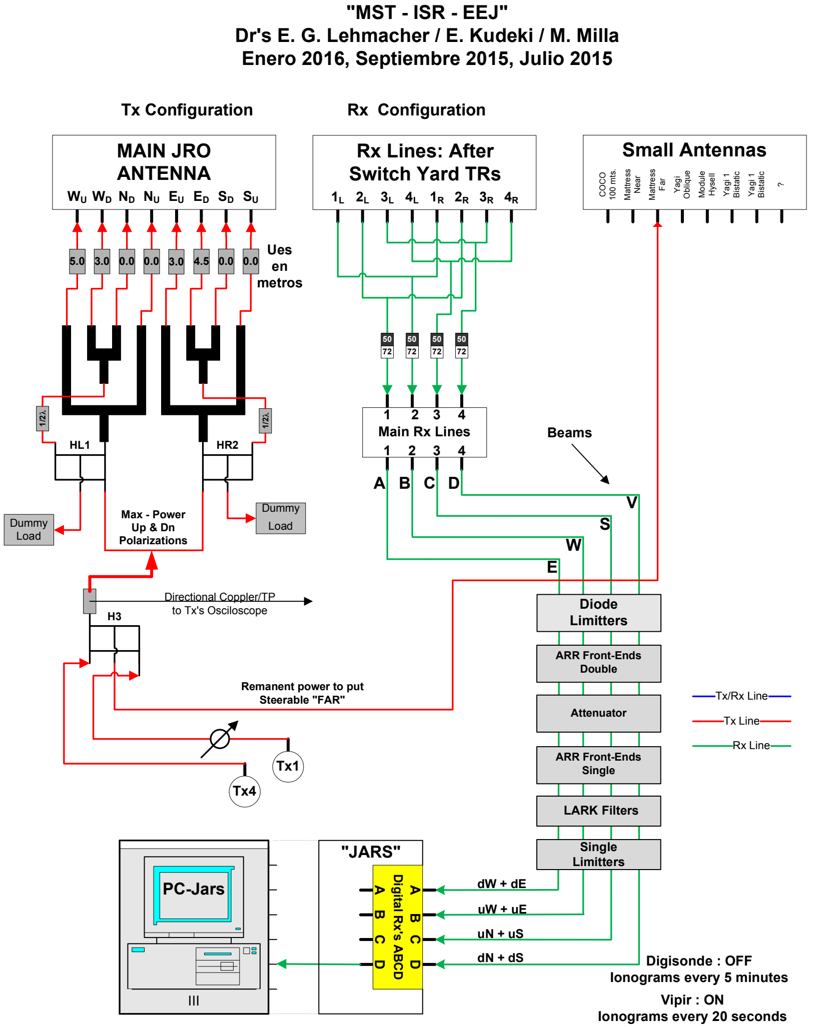

Digisonde : OFF
Ionograms every 5 minutes

Vipir : ON
Ionograms every 20 seconds

JARS system is synchronized with the PPS from a GPS

Figura 1

Figure B.3 – Switchyard configuration for MST-ISR experiment for years 2014, 2015, and 2016.

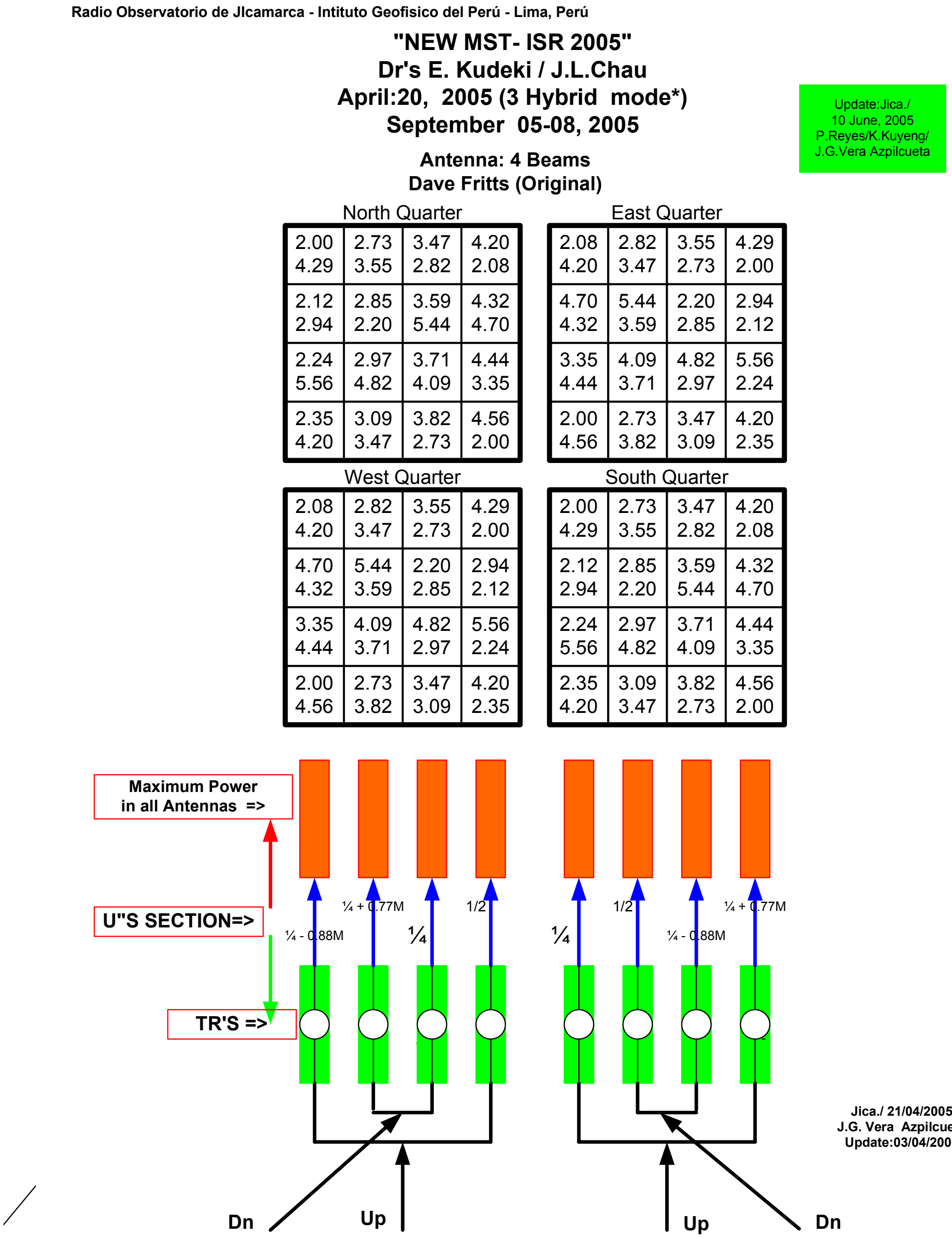

Radio Observatorio de Jlcamarca - Intituto Geofisico del Perú - Lima, Perú

"NEW MST- ISR 2005"
Dr's E. Kudeki / J.L.Chau
April:20, 2005 (3 Hybrid mode*)
September 05-08, 2005

Update:Jica./
10 June, 2005
P.Reyes/K.Kuyeng/
J.G.Vera Azpilcueta

Antenna: 4 Beams
Dave Fritts (Original)

North Quarter

2.00 4.29	2.73 3.55	3.47 2.82	4.20 2.08
2.12 2.94	2.85 2.20	3.59 5.44	4.32 4.70
2.24 5.56	2.97 4.82	3.71 4.09	4.44 3.35
2.35 4.20	3.09 3.47	3.82 2.73	4.56 2.00

East Quarter

2.08 4.20	2.82 3.47	3.55 2.73	4.29 2.00
4.70 4.32	5.44 3.59	2.20 2.85	2.94 2.12
3.35 4.44	4.09 3.71	4.82 2.97	5.56 2.24
2.00 4.56	2.73 3.82	3.47 3.09	4.20 2.35

West Quarter

2.08 4.20	2.82 3.47	3.55 2.73	4.29 2.00
4.70 4.32	5.44 3.59	2.20 2.85	2.94 2.12
3.35 4.44	4.09 3.71	4.82 2.97	5.56 2.24
2.00 4.56	2.73 3.82	3.47 3.09	4.20 2.35

South Quarter

2.00 4.29	2.73 3.55	3.47 2.82	4.20 2.08
2.12 2.94	2.85 2.20	3.59 5.44	4.32 4.70
2.24 5.56	2.97 4.82	3.71 4.09	4.44 3.35
2.35 4.20	3.09 3.47	3.82 2.73	4.56 2.00

Figure B.4 – Antenna phasing for the MST-ISR-EEJ experiment years 2005, 2006, and 2007.

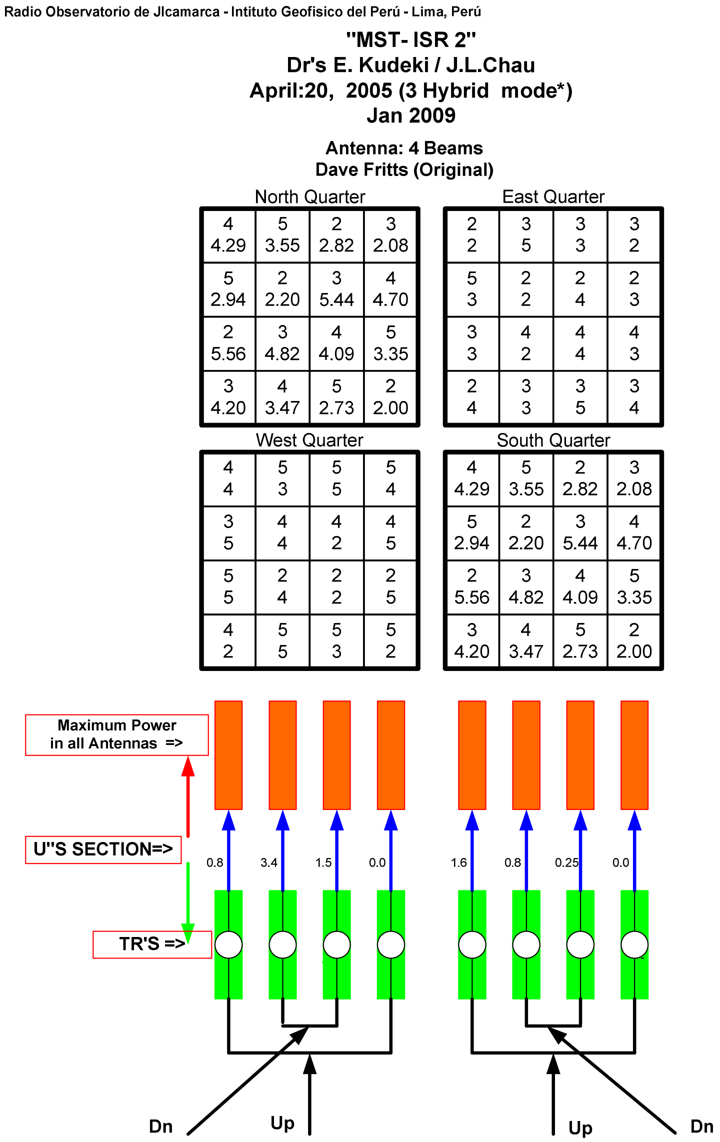

Radio Observatorio de JIcamarca - Intituto Geofisico del Perú - Lima, Perú

"MST- ISR 2"
Dr's E. Kudeki / J.L.Chau
April:20, 2005 (3 Hybrid mode*)
Jan 2009

Antenna: 4 Beams
Dave Fritts (Original)

North Quarter

4 4.29	5 3.55	2 2.82	3 2.08
5 2.94	2 2.20	3 5.44	4 4.70
2 5.56	3 4.82	4 4.09	5 3.35
3 4.20	4 3.47	5 2.73	2 2.00

East Quarter

2 2	3 5	3 3	3 2
5 3	2 2	2 4	2 3
3 3	4 2	4 4	4 3
2 4	3 3	3 5	3 4

West Quarter

4 4	5 3	5 5	5 4
3 5	4 4	4 2	4 5
5 5	2 4	2 2	2 5
4 2	5 5	5 3	5 2

South Quarter

4 4.29	5 3.55	2 2.82	3 2.08
5 2.94	2 2.20	3 5.44	4 4.70
2 5.56	3 4.82	4 4.09	5 3.35
3 4.20	4 3.47	5 2.73	2 2.00

Figure B.5 – Antenna phasing for the MST-ISR-EEJ experiment year 2009.

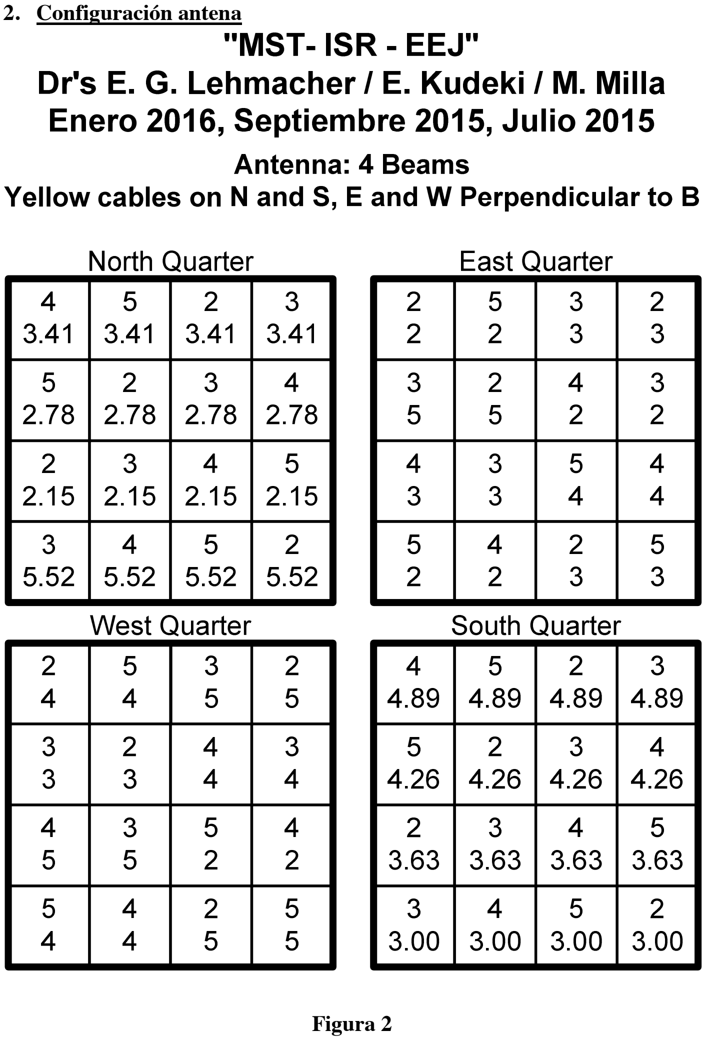

2. **Configuración antena**

"MST- ISR - EEJ"

Dr's E. G. Lehmacher / E. Kudeki / M. Milla

Enero 2016, Septiembre 2015, Julio 2015

Antenna: 4 Beams

Yellow cables on N and S, E and W Perpendicular to B

North Quarter

4 3.41	5 3.41	2 3.41	3 3.41
5 2.78	2 2.78	3 2.78	4 2.78
2 2.15	3 2.15	4 2.15	5 2.15
3 5.52	4 5.52	5 5.52	2 5.52

East Quarter

2 2	5 2	3 3	2 3
3 5	2 5	4 2	3 2
4 3	3 3	5 4	4 4
5 2	4 2	2 3	5 3

West Quarter

2 4	5 4	3 5	2 5
3 3	2 3	4 4	3 4
4 5	3 5	5 2	4 2
5 4	4 4	2 5	5 5

South Quarter

4 4.89	5 4.89	2 4.89	3 4.89
5 4.26	2 4.26	3 4.26	4 4.26
2 3.63	3 3.63	4 3.63	5 3.63
3 3.00	4 3.00	5 3.00	2 3.00

Figura 2

Figure B.6 – Antenna phasing for the MST-ISR-EEJ experiment years 2014, 2015, and 2016.

REFERENCES

Akgiray, A. H. (2007), Calibration of Jicamarca radar using F-region incoherent scatter for measurements of D-region backscatter RCS, master's thesis, Dept. of Electrical and Computer Engineering, University of Illinois at Urbana-Champaign, Urbana, Illinois.

Balsley, B. B. (1964), Evidence of a stratified echoing region at 150 kilometers in the vicinity of the magnetic equator during daylight hours, *Journal of Geophysical Research*, *69*(9), 1925–1930, doi:10.1029/JZ069i009p01925.

Bilitza, D. (2001), International Reference Ionosphere 2000, *Radio Science*, *36*(2), 261–275, doi:10.1029/2000RS002432.

Booker, H. G., and H. W. Wells (1938), Scattering of radio waves by the f-region of the ionosphere, *Terrestrial Magnetism and Atmospheric Electricity*, *43*(3), 249–256, doi:10.1029/TE043i003p00249.

Chau, J. L., and E. Kudeki (2006), First E- and D-region incoherent scatter spectra observed over Jicamarca, *Annales Geophysicae*, *24*(5), 1295–1303.

Chau, J. L., and E. Kudeki (2013), Discovery of two distinct types of equatorial 150 km radar echoes, *Geophysical Research Letters*, *40*(17), 4509–4514, doi:10.1002/grl.50893.

Chau, J. L., and R. F. Woodman (2004), Daytime vertical and zonal velocities from 150-km echoes: Their relevance to F-region dynamics, *Geophysical Research Letters*, *31*(L17801), 1–4, doi:10.1029/2004GL020800.

Chau, J. L., and R. F. Woodman (2005), D and E region incoherent scatter radar density measurements over Jicamarca, *Journal of Geophysical Research*, *110*(A12314), 1–7, doi:10.1029/2005JA011438.

Chau, J. L., R. F. Woodman, M. A. Milla, and E. Kudeki (2009), Naturally enhanced ion-line spectra around the equatorial 150-km region, *Annales Geophysicae*, *27*(3), 933–942.

Davies, K. (1969), *Ionospheric Radio Waves*, 1 ed., Blaisdell Publishing Company, Waltham, MA.

Farley, D. T. (1969), Faraday rotation measurements using incoherent scatter, *Radio Science*, *4*(2), 143–152, doi:10.1029/RS004i002p00143.

Hargreaves, J. K. (1992), *The solar-terrestrial environment: An introduction to geospace - the science of the terrestrial, upper atmosphere, ionosphere and magnetosphere.*, Cambridge Atmospheric and Space Science Series (5), 1 ed., Cambridge University Press.

Hedin, A. E. (1991), Extension of the MSIS thermosphere model into the middle and lower atmosphere, *Journal of Geophysical Research*, *96*(A2), 1159–1172, doi:10.1029/90JA02125.

Hildebrand, P. H., and R. S. Sekhon (1974), Objective determination of the noise level in doppler spectra, *Journal of Applied Meteorology*, *13*(7), 808—811.

Hines, C. O. (2013), *The Upper Atmosphere in Motion*, pp. 248–328, Geophysical Monograph Series, American Geophysical Union, doi:10.1029/GM018p0248.

Hocking, W. K., J. Röttger, R. D. Palmer, T. Sato, and P. B. Chilson (2016), *Atmospheric Radar: Application and Science of MST Radars in the Earth's Mesosphere, Stratosphere, Troposphere, and Weakly Ionized Regions*, Cambridge University Press, doi:10.1017/9781316556115.

Kelley, M. C. (2009), *The Earth's Ionosphere*, second edition ed., Academic Press, Burlington, MA.

Kudeki, E. (1988), *Lecture Notes on the Constitution and Behavior of the Upper Atmosphere*, Department of Electrical and Computer Engineering at the University of Illinois at Urbana-Champaign, Urbana, Illinois.

Kudeki, E., and C. D. Fawcett (1993), High resolution observations of 150 km echoes at Jicamarca, *Geophysical Research Letters*, *20*(18), 1987–1990, doi:10.1029/93GL01256.

Kudeki, E., and M. A. Milla (2011), Incoherent scatter spectral theories–Part I: A general framework and results for small magnetic aspect angles, *IEEE Transactions on Geoscience and Remote Sensing*, *49*(1), 315–328, doi:10.1109/TGRS.2010.2057252.

Kudeki, E., S. Bhattacharyya, and R. F. Woodman (1999), A new approach in incoherent scatter F region $E \times B$ drift measurements at Jicamarca, *Journal of Geophysical Research*, *104*(A12), 28145–28162, doi:10.1029/1998JA900110.

Lehmacher, G. A., E. Kudeki, A. H. Akgiray, L. Guo, P. M. Reyes, and J. L. Chau (2009), Radar cross sections for mesospheric echoes at Jicamarca, *Annales Geophysicae*, *27*(7), 2675–2684.

Negrea, C., N. Zabotin, T. Bullett, T. Fuller-Rowell, T.-W. Fang, and M. Codrescu (2016), Characteristics of acoustic gravity waves obtained from dynasonde data, *Journal of Geophysical Research: Space Physics*, *121*(4), 3665–3680, doi:10.1002/2016JA022495, 2016JA022495.

Ochs, G. R. (1965), The large 50 mc/s dipole array at Jicamarca radar observatory, *NBS Report 8772*, National Bureau of Standards, 1965.

Oppenheim, M. M., and Y. S. Dimant (2016), Photoelectron-induced waves: A likely source of 150 km radar echoes and enhanced electron modes, *Geophysical Research Letters*, pp. n/a–n/a, doi:10.1002/2016GL068179.

Prakash, S., S. P. Gupta, and B. H. Subbaraya (1969), Irregularities in the equatorial E region over Thumba, *Radio Science*, *4*(9), 791–796, doi:10.1029/RS004i009p00791.

Prölss, G. W. (2004), *Physics of the Earth's Space Environment, An Introduction*, 1 ed., Springer Berlin / Heidelberg.

Reyes, P. M. (2012), Solar-flare effects observed over Jicamarca during MST-ISR experiments, master's thesis, Dept. of Electrical and Computer Engineering, University of Illinois at Urbana-Champaign, Urbana, Illinois.

Rishbeth, H., and O. K. Garriott (1969), *Introduction to Ionospheric Physics*, *International Geophysics Series*, vol. 14, 1 ed., Academic Press, INC., New York, NY and London.

Røyrvik, O. (1982), Drift and aspect sensitivity of scattering irregularities in the upper equatorial e region, *Journal of Geophysical Research: Space Physics*, *87*(A10), 8338–8342, doi:10.1029/JA087iA10p08338.

Scotto, C. (2009), Electron density profile calculation technique for autoscala ionogram analysis, *Advances in Space Research*, *44*(6), 756–766, doi:doi:10.1016/j.asr.2009.04.037.

Sheth, R., E. Kudeki, G. A. Lehmacher, M. F. Sarango, R. F. Woodman, J. L. Chau, L. Guo, and P. M. Reyes (2006), A high-resolution study of mesospheric fine structure with the Jicamarca MST radar, *Annales Geophysicae*, *24*(5), 1281–1293, doi:10.5194/angeo-24-1281-2006.

Su, Y.-J., J. L. Horwitz, G. R. Wilson, P. G. Richards, D. G. Brown, and C. W. Ho (1998), Self-consistent simulation of the photoelectron-driven polar wind from 120 km to 9 R_E altitude, *Journal of Geophysical Research: Space Physics*, *103*(A2), 2279–2296, doi:10.1029/97JA03085.

Thébault, E., et al. (2015), International geomagnetic reference field: the 12th generation, *Earth, Planets and Space*, *67*(1), doi:10.1186/s40623-015-0228-9.

Varney, R. H., M. C. Kelley, and E. Kudeki (2009), Observations of electric fields associated with internal gravity waves, *Journal of Geophysical Research: Space Physics*, *114*(A2), n/a–n/a, doi:10.1029/2008JA013733, a02304.

Woodman, R. F. (1985), Spectral moment estimation in MST radars, *Radio Science*, *20*(6), 1185–1195, doi:10.1029/RS020i006p01185.